16 State House Station
Augusta, Maine 04333

MaineDOT

Transportation Research Division

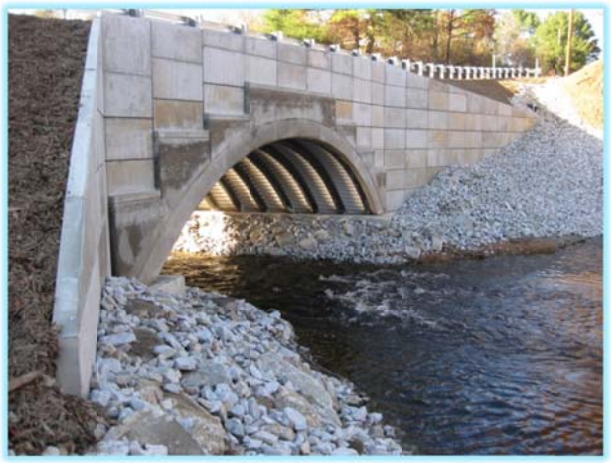

Technical Report 14-03

Bridge-in-a-Backpack™

Task 2: Reduction of costs through design modifications and optimization

Final Report – Task 2, September 2011

Technical Report Documentation Page

1. Report No. ME 14-03	2.	3. Recipient's Accession No.	
4. Title and Subtitle Bridge-in-a-Backpack™ Task 2: Reduction of costs through design modifications and optimization		5. Report Date September 2011 6.	
7. Author(s) Harold Walton Bill Davids Ph.D P.E. Josh Clapp P.E. Keenan Goslin P.E. Roberto Lopez-Anido Ph.D, P.E.		8. Performing Organization Report No. AEWC Report Number 12 – 08.814	
9. Performing Organization Name and Address University of Maine – Advanced Structures and Composites Center		10. Project/Task/Work Unit No. Project 17681.00 - Task 2 11. Contract © or Grant (G) No. Contract # 2010*3692	
12. Sponsoring Organization Name and Address Maine Department of Transportation		13. Type of Report and Period Covered 14. Sponsoring Agency Code	
15. Supplementary Notes			

16. Abstract (Limit 200 words)

The cost effective use of FRP composites in infrastructure requires the efficient use of the composite materials in the design. Previous work during the development phase and demonstration phase illustrated the need to refine the design methods for portions of these types of structures. Three parts were included in this task aimed at reducing costs through design modifications and optimization. They include improvements to the soil-structure interaction analysis methods, identification and/or design of a stronger decking material to span between the arches, and other advanced modeling tools. In the case of advanced modeling tools, it has been shown that a very important portion of the loading history of the arches includes the concrete filling of the tubes during construction. A majority of this report explains the evaluation and modeling of unfilled, hollow tubes to create a knowledge base and design methodology where the tubes could be safely analyzed for filling loads.

17. Document Analysis/Descriptors Arch bridges, concrete filled FRP tubes, Bridge-in-a-Backpack		18. Availability Statement	
19. Security Class (this report)	20. Security Class (this page)	21. No. of Pages 170	22. Price

Bridge-in-a-Backpack™
Task 2: Reduction of costs through design modifications and optimization

AEWC Project 814
PIN 017681.00

Prepared for:
Dale Peabody
Maine Department of Transportation
Office of Safety, Training, and Research
16 State House Station
Augusta, ME 04333
(207) 624-3305

AEWC Report Number
12 – 08.814

September 27th, 2011

Prepared by:

Harold Walton
Bill Davids Ph.D P.E.
Josh Clapp P.E.
Keenan GoslinP.E.
Roberto Lopez-Anido Ph.D P.E.

An ISO 17025 accredited testing laboratory
Accredited by International Accreditation Service

AEWC Advanced Structures & Composites Center
5793 AEWC Bldg
University of Maine
Orono, ME 04469-5793

CONFIDENTIAL

Telephone: 207-581-2123
FAX: 207-581-2074
contactaewc@umit.maine.edu
www.aewc.umaine.edu

Bridge-in-a-Backpack™
Task 2: Reduction of costs through design modifications and optimization

The cost effective use of FRP composites in infrastructure requires the efficient use of the composite materials in the design. Previous work during the development phase and demonstration phase illustrated the need to refine the design methods for portions of these types of structures. Three parts were included in this task aimed at reducing costs through design modifications and optimization. They include improvements to the soil-structure interaction analysis methods, identification and/or design of a stronger decking material to span between the arches, and other advanced modeling tools. In the case of advanced modeling tools, it has been shown that a very important portion of the loading history of the arches includes the concrete filling of the tubes during construction. A majority of this report explains the evaluation and modeling of unfilled, hollow tubes to create a knowledge base and design methodology where the tubes could be safely analyzed for filling loads.

Task 2.1 Simplified Modeling to Assess Soil-Structure Interaction Effects

All applications to date of hybrid FRP concrete arch tubular bridges have been buried structures where transverse decking was placed across the arches to distribute soil loads, dead loads, and live loads to the arches. FRP decking may be used alone or as formwork for reinforced concrete decking. Present structural analysis methods consist of finite element (FE) models that utilize 2D Euler-Bernoulli beam elements to model the arch. Nonlinear moment-curvature relationships can be included. The axial and bending stiffnesses of the concrete deck, if present, are neglected. Soil loads are applied by assuming a constant lateral earth pressure coefficient, K (taken as the at-rest coefficient, K_o), to relate horizontal and vertical soil pressures.

This document is intended to summarize the work that was performed by the University of Maine AEWC Advanced Structures and Composites Center (AEWC) in collaboration with Advanced Infrastructure Technologies (AIT) to develop new structural analysis software to analyze buried arch bridges that accounts for unbalanced backfilling and the potentially beneficial restraining effect of the compacted backfill on the arches. All routines were written in MATLAB (MathWorks 2009) so that the user has full control

over the analysis and may easily make changes to the analysis routines. The software incorporates four key capabilities:

1. The effect of staged construction was simulated by applying soil lifts sequentially on alternating sides of the arch.
2. A nonlinear soil constitutive relationship was incorporated by adding soil springs to the model corresponding to each layer of soil after it is placed.
3. Recognizing that the arches behave as stiff ribs supporting the more flexible deck, which may significantly affect soil-structure interaction, the decking was explicitly modeled using transverse elements perpendicular to the plane of the arch.
4. The effect of the axial and bending stiffness of the concrete deck, if present, in the longitudinal (span) direction was included in the model.

The net effect of these key features of the analysis methodology was investigated by modeling the backfilling of an example bridge which is proposed for construction in the near future at the time of this report. This allowed realistic parameters to be considered in a practical design scenario. Throughout this document references are made to this particular bridge project referred to as the Ellsworth Bridge. Details describing the example bridge and in general the work that was to be performed as part of the contract can be found in Clapp (2011).A collection of content specifically related to the programming aspect of the project can be found in Clapp (2011) as well.

Finite element model

Three-dimensional (3D) elements were utilized in order to capture the effect of decking flexibility in the transverse direction (spanning between arches). A schematic view of the finite element mesh is shown in Figure 1. Three element types were used: arch elements (also includes longitudinal decking stiffness if applicable), transverse decking elements, and soil spring elements. Nonlinear 3D Euler-Bernoulli beam elements were used to model the arch in the longitudinal direction as well as the decking in the transverse direction. If a concrete deck is present, the stiffness of the deck in the longitudinal direction is added to the stiffness of the arch to arrive at the total non-composite stiffness for these elements. For this study, a cracked section was considered for the concrete deck in both the longitudinal and transverse directions. Soil spring elements were based on a compression-only constitutive relationship that is discussed later. The arch boundary conditions were taken as fully fixed at the ends, although other boundary conditions can be specified. Loads were applied to nodes defining the transverse decking elements and were then transferred to the arch.

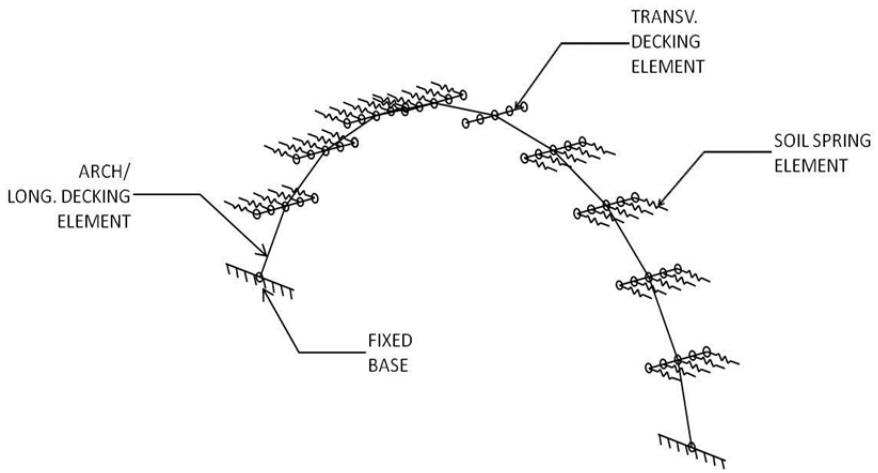

Figure 1 – Schematic 3D View of FE Mesh (Coarse Mesh Shown for Clarity)

Arch and Longitudinal Decking Elements

General nonlinear 3D Euler-Bernoulli beam elements were used to model the arch, although only in-plane deflections/member forces occurred since the arch was not subjected to out-of-plane loads in this study. The in-plane tangent bending stiffness, EI, and bending moment for the arch are a function of curvature and axial load level. These values were interpolated from relationships provided by AIT. If a concrete deck is present, it is also necessary to account for the in-plane longitudinal bending and axial stiffness of this layer. In this study, two different values of EI corresponding to cracked sections were used depending on whether positive or negative bending was occurring. This was necessary since the location of reinforcement was non-symmetric through the depth of the deck. It is also possible for the user to specify a generic moment-curvature relationship for the decking in the longitudinal direction. The area used to calculate axial stiffness, EA, of the decking was taken as the full uncracked cross-sectional area of the concrete. Throughout analyses the total axial load was split into arch and decking components proportionally to their stiffnesses and only the arch component was used when interpolating for its bending stiffness and moment.

Transverse Decking Elements

General and specialized nonlinear 3D Euler-Bernoulli beam elements were used to model the decking in the transverse direction. These elements were only intended to capture the effect of transverse bending, which leads to variable soil pressures across the length of the decking elements. Longitudinal bending and axial stiffness of the decking was included with the arch elements. A single row of decking elements, which can contain any even number of elements, extends from –s/2 to s/2, where s is the center-to-center

spacing of the arches. The local coordinate system [x′,y′,z′] of the decking elements is defined in Figure 2. The global coordinate system [X,Y,Z] is also shown for reference. Note that the x′ axis is parallel to the Z axis. For each element, the z′ axis was taken as being parallel to a line connecting the two adjacent arch nodes, as indicated by line A-B in Figure 2. The y′ axis was taken as perpendicular to the x′ and z′ axes. The actual bending stiffness of the deck was used for bending about the z′ axis. A large bending stiffness was applied for bending about the y′ axis to effectively prevent displacements in the x′-z′ plane. To model the symmetric bending of the decking, rotations about the z′ axis at each end of the decking must be prevented. Specialized elements were used to achieve this rotational restraint at coordinates Z = –s/2 and Z = s/2. This boundary condition was taken into account in the element formulation to arrive at a consistent element stiffness matrix, and it was not necessary to apply additional constraints in the model. General 3D Euler-Bernoulli beam elements were used for all other decking elements.

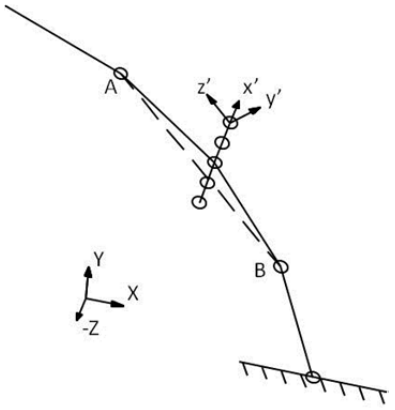

Figure 2 – Definition of Local Coordinate System for Transverse Decking Elements

Soil Spring Elements

Soil spring elements were oriented horizontally and only carried compressive axial loads. The axial load level F_{spring} depends on the tributary horizontal area A_h, the vertical pressure σ_v due to overburden and other loads, and the lateral earth pressure coefficient K as shown in Equation 1 below. Here, A_h was taken as the product of half of the elevation difference between the two adjacent nodes along the length of the arch and the z-spacing of decking nodes (or z-spacing/2 for nodes at the planes of symmetry).

$$F_{spring} = A_h \times \sigma_v \times K$$ Equation 1

Stiffness was estimated by using a forward difference approximation where a small deflection was applied. The tributary area for a particular element remained constant throughout the analysis, whereas σ_v and K changed as a function of additional loading and deflections, respectively. The lateral earth pressure coefficient K was defined based on Figure 3 below (see 'UMaine Model'), where deflections away from the soil were taken as positive. A curve reproduced from National Cooperative Highway Research Program (NCHRP 1991) is also shown for comparison. Note that the UMaine Model is just a simplified quadrilinear version of the NCHRP (1991) curve defined by the three pressure coefficients, except that K_o was taken as 0.45. This value represents a compromise between the NCHRP (1991) value of 0.4 and the value recommended by Maine DOT for culvert design of 0.47. Precedent for this approach can be found in literature on integral abutment bridges (Faraji et al. 2001; Ting and Faraji 1998) and in design procedures for earth retaining structures (USACoE 1994). Note that the UMaine model yields much softer behavior for the soil springs than the NCHRP curve, which was believed to be conservative. We note here that the MATLAB code developed as part of this work is quite general, and should permit alternative soil spring load-deformation relationships to be implemented fairly easily.

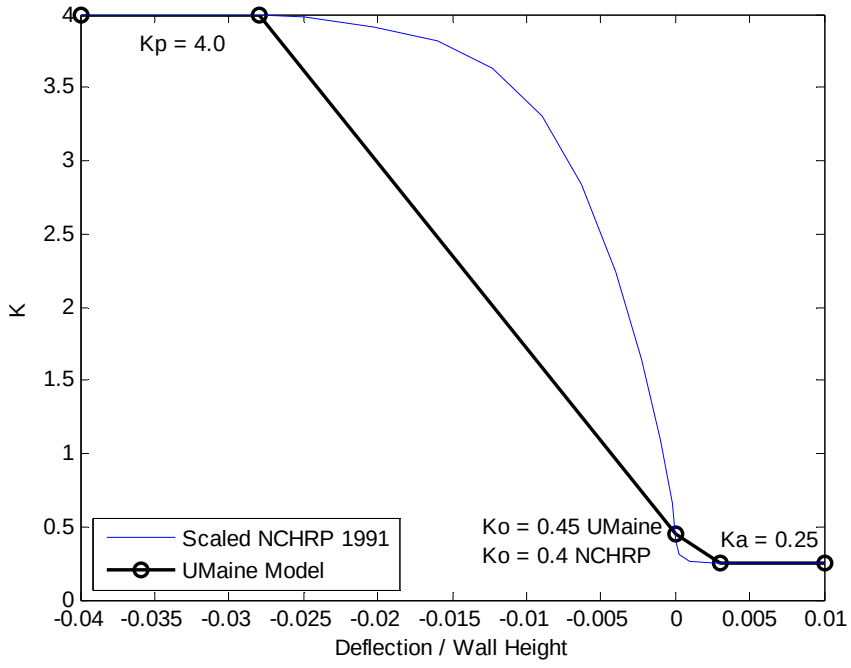

Figure 3 – Lateral Earth Pressure Coefficient as a Function of Relative Movement after NCHRP (1991) for Medium-Dense Backfill

The wall height for the example case was taken as the height of the arch, or 14 ft., which implies that deflections of approximately 0.5 in. away from and 4.7 in. into the soil are necessary to achieve the active and passive states, respectively. These deflections were defined relative to the horizontal displacement of the arch at the location of the spring after the applicable soil lift was applied (i.e. after a lift was placed that first caused a particular soil spring to be buried, the initial relative deflection for this soil spring was zero).

Consideration of staged construction

In the field, the backfilling process is performed after the arches are placed and decking is installed. Generally, based on recent bridge construction projects, the backfill is placed in lifts that do not exceed 12 in. in height and lifts are placed sequentially on alternating sides of the arch. Each lift is compacted before the next lift is placed. It was assumed for the analyses described in this document that a lift is in the at-rest state once it has been placed and compacted. After this point the state depends on deflections. Lifts were applied in 12 in. increments on alternating sides of the arch since this was believed to be the maximum differential between lifts on opposing sides of the arch during construction i.e. the scenario that causes the largest amount of side-sway. (The program allows lift heights of other than 12 in. to be specified.) The algorithm for the staged construction procedure, which takes place after the self-weight of arch and decking components are applied, was as follows:

1. Apply a new lift of soil.
    a. Horizontal loads corresponding to the at-rest lateral earth pressure coefficient K_o are applied within the region of this lift in addition to vertical loads applied in all applicable regions.
    b. Element shape functions are used to calculate statically equivalent nodal loads for vertical and horizontal soil pressures that vary linearly over the length of an element.
    c. The tributary distance in the z-direction is taken as the z-spacing of decking elements (or z-spacing/2 for nodes at the planes of symmetry).
2. Adjust the vertical pressure for any lifts that are below the new lift.
3. Re-calculate the stiffness of each soil spring based on the additional vertical pressure as well as the change in relative deflection.
4. Utilize a nonlinear Newton-based solver to determine the position of equilibrium, while continually updating the stiffness of nonlinear elements in the model including the soil springs.

5. After a solution has been obtained, activate any springs that were buried by the lift that was just applied.
6. Set the zero relative displacement position of the newly activated springs to be at the X-coordinate of the current deflected position. This 'zero' position will be retained for all future load steps.
7. Repeat 1-6 until all lifts are applied.
8. Apply additional loads such as dead load of the wearing surface and vehicle live loads.

Consideration of live loads

After backfilling was completed, the next step was to apply the wearing surface and then live loads were applied. Both a uniform lane load and a vehicular live load were considered per AASHTO. In this software, this process was broken into three steps: 1) dead load of the wearing surface DW, 2) AASHTO lane load, and 3) AASHTO vehicular loading. All analyses resume from the point at which the previous step was completed. For example, the DW analysis starts from the point at which the last backfilling step was applied. This was necessary since the principle of superposition does not apply for nonlinear analyses. The results of step (3) minus the results of step (1) represented the total effect of live loading. The lane load was applied separately from the live load only because it is a constant load and therefore it is not necessary to re-apply it for various truck positions in an envelope-type analysis. This may result in reduced computational time.

The loads and vertical stresses associated with the dead load of the wearing surface and the uniform lane load were simply based on tributary area. On the other hand, the loads for the vehicular live load were calculated using the integral solution to the Boussinesq vertical stress equation. The vertical stress used to calculate soil spring forces due to vehicular live loads was taken as the calculated force divided by the tributary area.

Specific parameters used for analyses

All analyses conducted as part of this study were based on expected values for the proposed Ellsworth Bridge Project. A majority of these parameters were directly provided by AIT and are summarized in Table 1. Parameters not directly provided were calculated/ estimated based on drawings and other information provided by AIT. Supporting calculations are provided in Appendix A.

Table 1 – Specific Parameter Values for Analyses

Description	Variable	Units	Decking	
			Concrete	FRP
Diameter of CFRP tube	diam	in	11.8	
Rise of arch centerline	rise	ft	14	
Span of arch centerline	span	ft	34.33	
Depth of backfill above arch crown	depth_crown	ft	Variable, 3-12.5	
Depth of wearing surface	DW_depth	in	3	
Equivalent deck thickness for self-weight calculation	deck_thick	in	7.8	0.31
Arch spacing	spacing	in	60	
Strength of concrete in the arch	Fpc	psi	5000	
Soil density	rho	pcf	125	
Wearing surface density	rho_asphalt	pcf	140	
Design truck axle	Axle_space		Short	
Number of lanes loaded	num_lanes		2	
All load factors			1	
Number of arch elements	numels		60	
Number of deck elements (per section)	num_deck		8	
Effective height for which to apply soil springs	H_effective	ft	14	
Elastic modulus of deck	E_deck	ksi	3759	4200
Area of concrete deck, long.	A_deck	in^2/in	5	NA
Positive bending moment of inertia, long.	I_pos	in^4/in	0.592	NA
Negative bending moment of inertia, long.	I_neg	in^4/in	0.066	NA
Area of concrete deck, trans.	A_deck	in^2/in	7.68	0.303
Positive & negative bending moment of inertia, trans.	I_deck	in^4/in	3.2	0.93
Effective radial distance from arch centerline to soil	t_deck	in	14.4	7.9
Lateral pressure coefficient, active	Ka		0.25	
Lateral pressure coefficient, at-rest	Ko		0.45	
Lateral pressure coefficient, passive	Kp		4	

Deflection/H_effective, active	delta_Ka		0.003
Deflection/H_effective, passive	delta_Kp		0.028

The geometry of the circular arc-segment was provided by AIT. Another arch geometry, referred to as the "Bebo" or "ConSpan" arch was also provided by AIT. The geometry of this arch is based on an elliptical shape. It is steeper near the supports and flatter near midspan as compared to a circular arc-segment arch. The total span and rise were held constant. An intermediate multi-radius geometry was also considered. This was a symmetric 3-radius arch with interior (around midspan) curve defined by a radius of about 19.6 ft and included angle of about 77.4 degrees. The exterior (near supports) curves of this geometry were defined by a radius of about 13.3 ft and included angle of about 48.4 degrees. All three geometries are shown in Figure 4.

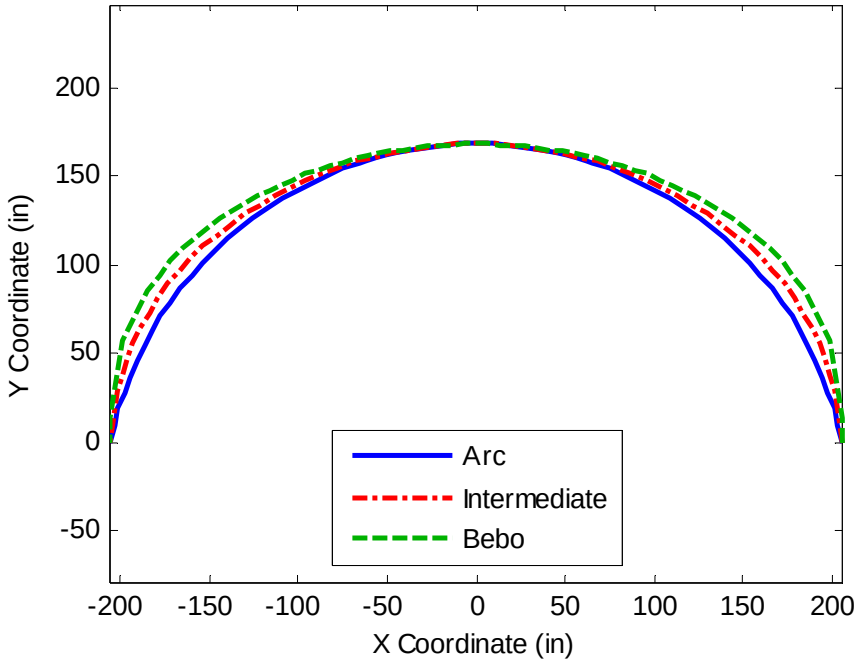

Figure 4 – Geometric Configurations for Analyses

Results: effect of staged backfilling

Staged backfilling affects analysis results in several ways: 1) alternating soil lifts result in side-sway and non-symmetric response about midspan; 2) staged backfilling allows

lateral earth pressure coefficients other than the at-rest coefficient to be rationally considered, which generally reduces critical response values; and 3) staged backfilling allows the structural response to be tracked throughout the construction period, which is important if the greatest response occurs prior to the final backfilling step.

The effect of staged backfilling was examined by running the matrix of analyses shown in Table 2. Three different arch bending stiffness relationships were considered, one of which utilized the nonlinear moment-curvature relationship provided for the arch tubes of this study. The others were linear-elastic relationships intended to provide approximate bounds on the response that would be expected. Both FRP decking and concrete decking were considered. The concrete decking is placed on top of another type of FRP decking in actual bridge applications, but this type of FRP is much softer than the FRP decking that would be used instead of concrete, and its stiffness was neglected in analyses. Three different levels of backfilling were considered: 3, 6, and 12.5 ft. The 3 ft and 6 ft depths are similar to actual values that have been used for recently constructed bridges. The 12.5 ft depth is the specified depth for the proposed Ellsworth Bridge. All results shown here are for service (unfactored) loads.

Results of analyses are presented in Figure 5 through Figure 9 below for both types of decking and also for both arch moment and total foundation thrust. Envelope arch moments are presented, meaning that the values represent the maximum/minimum values for any point along the length of the arch at a particular load step (average backfill elevation).

Table 2 Matrix of Analyses to Examine the Effect of Staged Backfilling

Arch Bending Stiffness	**Decking**	**Backfill Depth Above Centerline of Arch Crown (ft)**
Nonlinear	Concrete	3
Linear, Uncracked Section	FRP-only	6
Linear, Cracked Section	--	12.5

Envelope Arch Moments

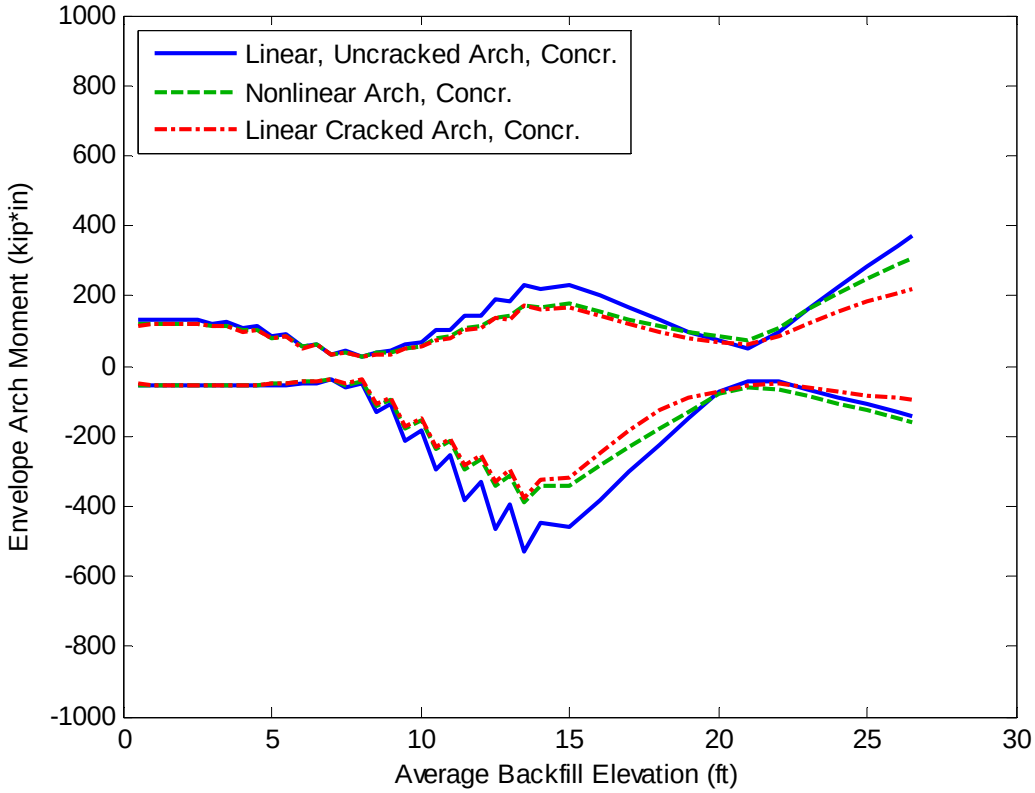

Figure 5 – Backfilling Envelope Arch Moment for Various Arch Bending Stiffness Relationships, Concrete Deck

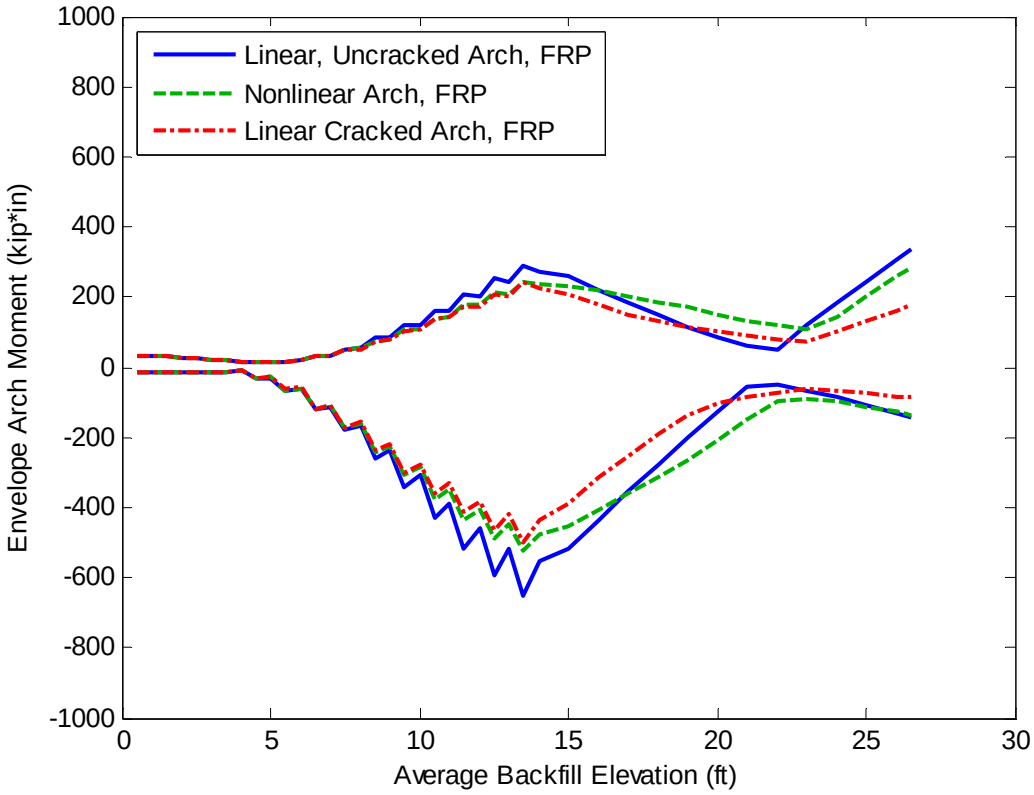

Figure 6 – Backfilling Envelope Arch Moment for Various Arch Bending Stiffness Relationships, FRP Deck

As shown in Figure 5 and Figure 6, the response of the nonlinear arch generally falls between those of the two corresponding linear models for arch bending moment. Generally the arch moments reach a peak at some point during construction near the point at which the backfill elevation approaches the height of the arch (14 ft). After which the magnitude of the moments generally decreases until the backfill elevation is around 21-22 ft, and then increases again. Thus, the critical construction moment may occur prior to the last load step, depending on the final backfill elevation.

The increased moment at elevations near 14 ft. stems from the fact that the alternating soil lifts cause side-sway and increased moments. The side-sway is depicted graphically in Figure 7 for the model with nonlinear arch bending stiffness relationship and a concrete deck. The original position of the arch is outlined in black. The deformed shape is indicated by the thick blue line (deflections are scaled by a factor of 10). It is apparent

from this illustration that the deflections (and resulting moments) are much greater as the backfill level is near the top of the arch. However, at the final grade elevation, the deflections are relatively small and many of the soil springs (not shown) have increased in stiffness (i.e. $K > K_o$). This stiffness of the soil is expected to reduce live load moments in the arch.

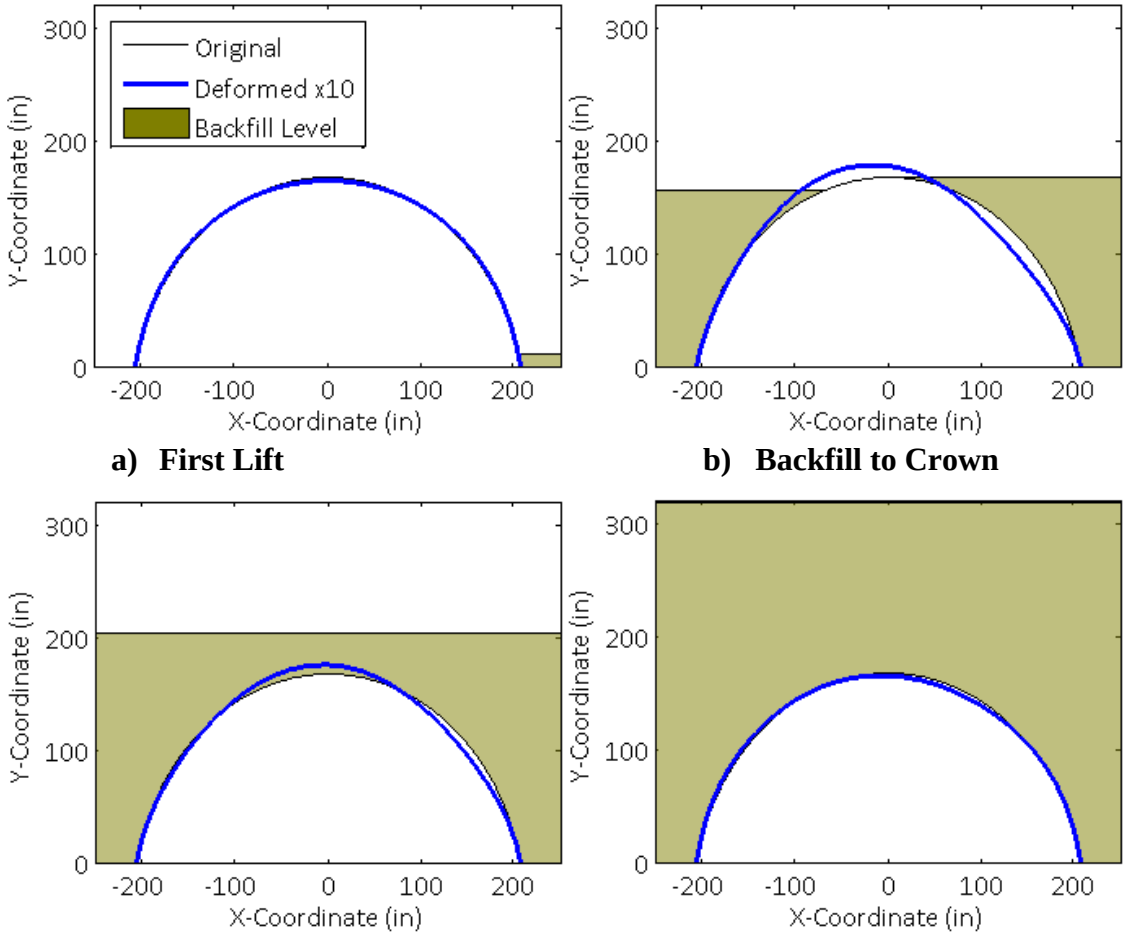

a) First Lift **b) Backfill to Crown**

c) 3 ft. Above Crown (Typical) **d) 12.5 ft. Above Crown**

Figure 7 – Deflected Shape of the Arch at Various Backfill Levels, Nonlinear Arch Bending Stiffness, Concrete Deck

Outward Foundation Thrust

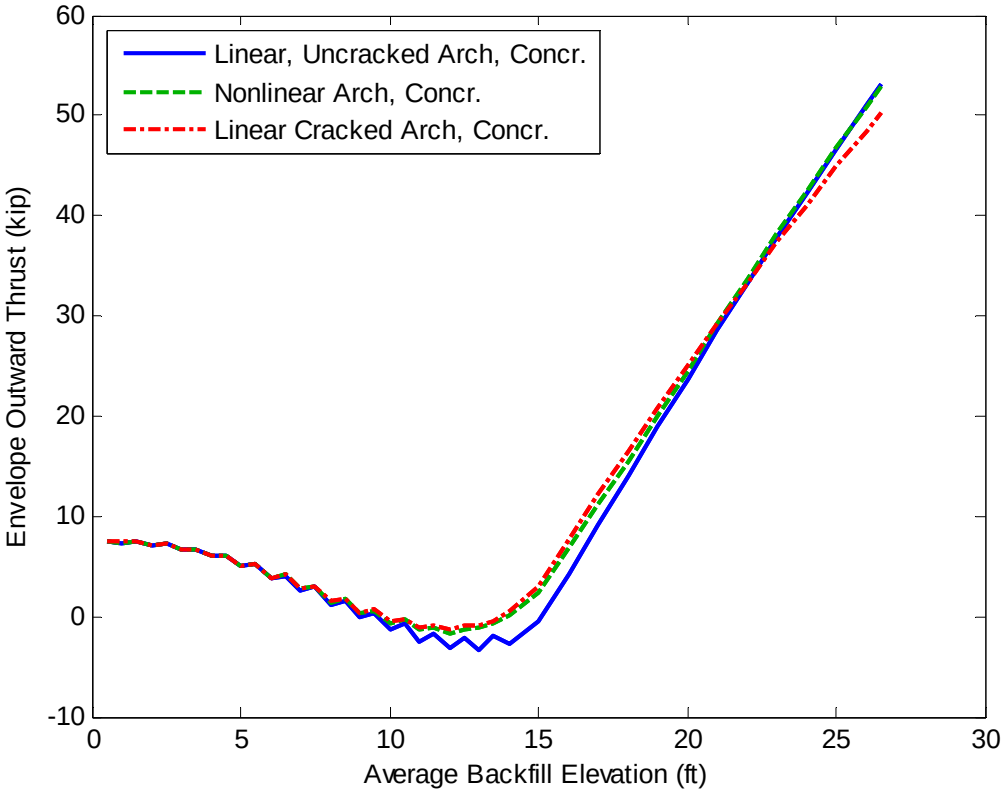

Figure 8 – Backfilling Envelope Outward Thrust for Various Arch Bending Stiffness Relationships, Concrete Deck

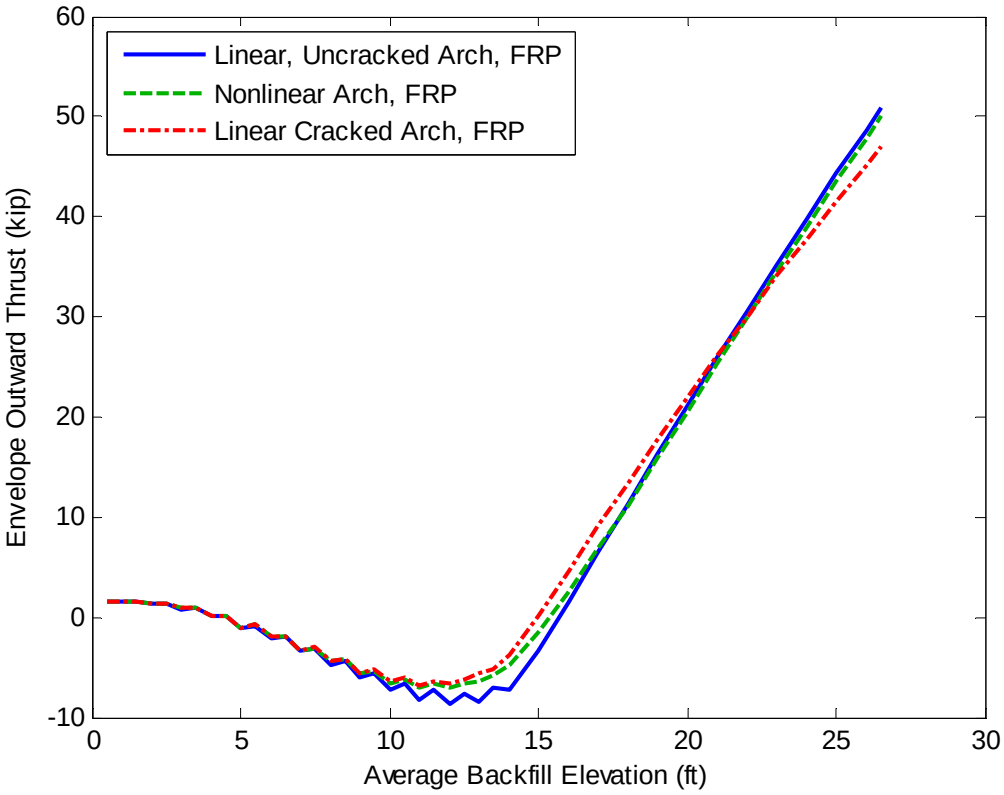

Figure 9 – Backfilling Envelope Outward Thrust for Various Arch Bending Stiffness Relationships, FRP Deck

As shown in Figure 8 and Figure 9, the response of the nonlinear arch again generally falls between the responses of the two corresponding linear models for arch outward thrust. Note that thrust values for the concrete-decked arches are initially much larger than those for FRP-decked arches due to the increased self-weight of the concrete. However, as the backfill elevation exceeds the approximate height of the arch, the thrust forces are dominated by the backfilling loads and both types of decking show similar results. It is important to note that the thrust force reported is not the total horizontal reaction, but rather the horizontal reaction at the base of the arch. The total reaction is the sum of the base reaction plus all of the horizontal spring forces.

Envelope Arch Axial Load

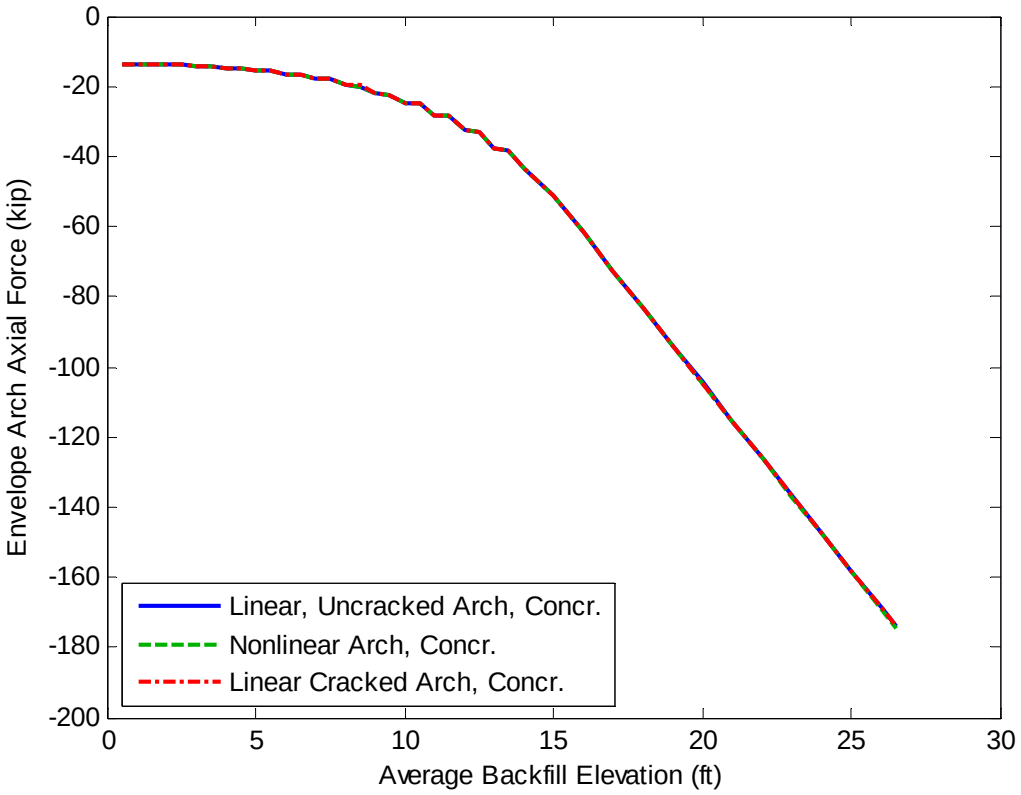

Figure 10– Backfilling Envelope Arch Axial Load for Various Arch Bending Stiffness Relationships, Concrete Deck

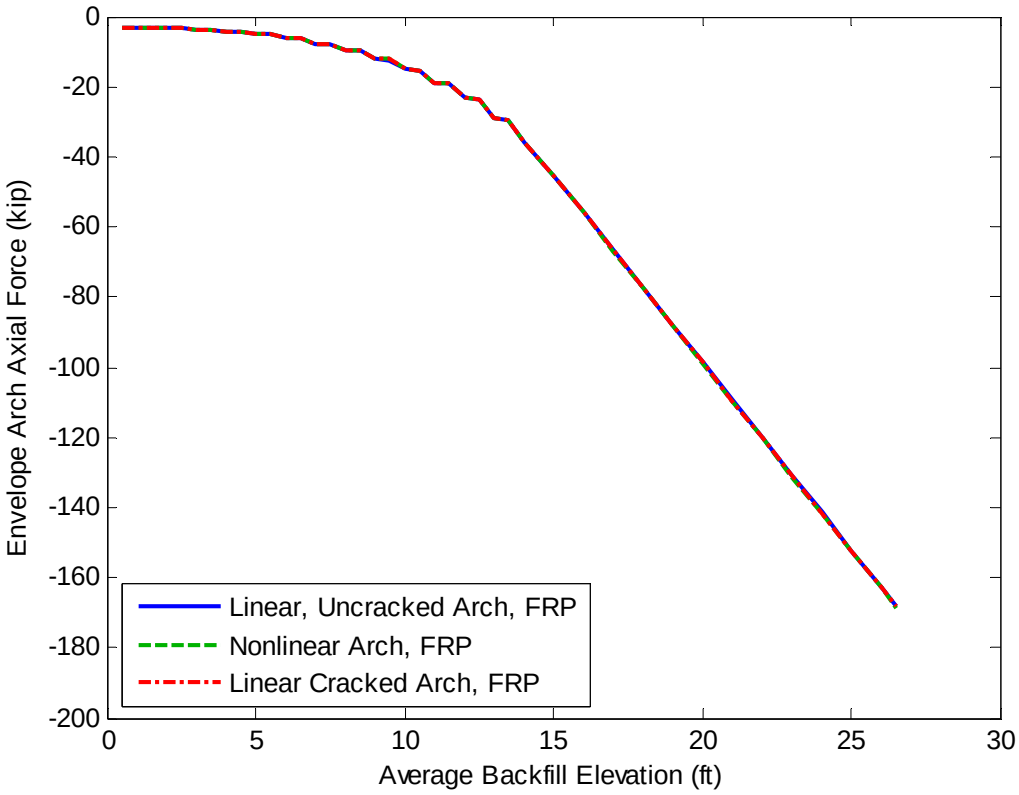

Figure 11 – Backfilling Envelope Arch Axial Load for Various Arch Bending Stiffness Relationships, FRP Deck

As shown in Figure 10 and Figure 11, the axial response of the arch is practically unaffected by the type of relationship used to describe the arch bending stiffness. The magnitude of the axial load in the concrete-decked arches is slightly more than for the FRP-decked arches due to the increased self-weight.

Results: effect of arch geometry

The geometry of the arches has a major effect on the way that the structure responds to a given set of loads. All bridges constructed to-date have utilized circular arc-segment arches. However, this configuration may not be ideal for all applications. Other geometric configurations are possible and have been considered for future projects. For example, one possible configuration is an arch that is relatively steeper near the supports and flatter near midspan as compared to a circular segment arc shape. This shape tends to result in

decreased foundation thrust and increased arch member bending moments. Based on economic factors, the shape of the arch could be optimized to achieve a desired effect. In this study, the effect of arch geometry was investigated by analyzing the three geometric shapes described previously. The matrix of analyses conducted is shown below in Table 3.

Table 3 Matrix of Analyses to Examine the Effect of Arch Geometry

Arch Geometry	**Decking**
Circular Segment Arc	Concrete
ConSpan Bebo Arch	FRP-only
Multi-radius (Intermediate)	--

Envelope Arch Moments

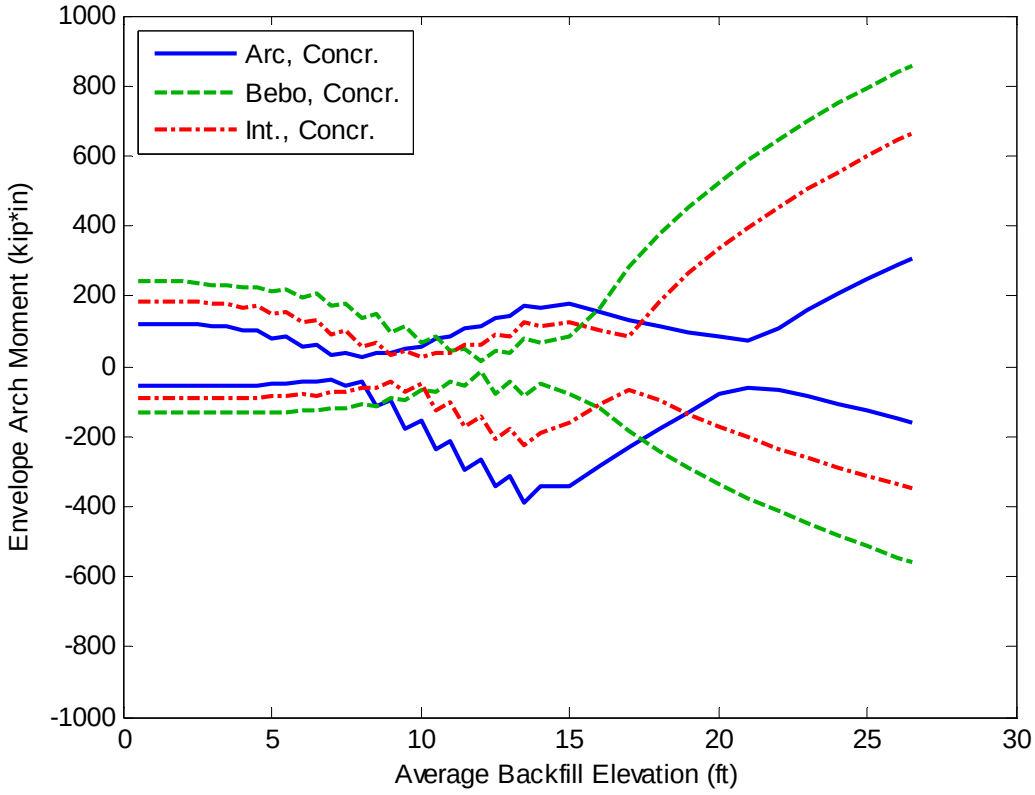

Figure 12 – Backfilling Envelope Arch Moments for Various Geometric Configurations, Concrete Deck, 12.5 ft of Total Fill Above the Crown

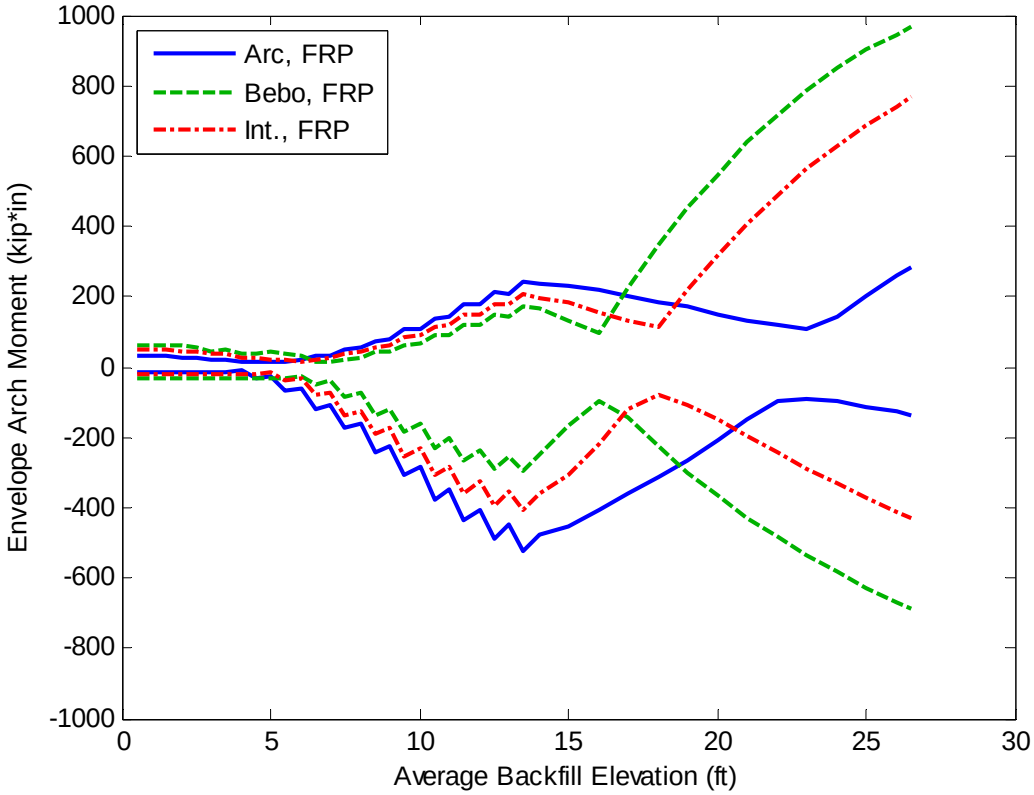

Figure 13 – Backfilling Envelope Arch Moments for Various Geometric Configurations, FRP Deck, 12.5 ft of Total Fill Above the Crown

It is apparent from Figure 12 and Figure 13 that the moment in the arch increases significantly at high backfill elevations going from the arc shape to the intermediate shape and again going from the intermediate shape to the Bebo shape. The reverse is true for the moment in the arch when the backfill elevation is near the height of the arch. This may indicate that shapes such as the Bebo arch are more appropriate for relatively small crown burial depths.

Outward Foundation Thrust

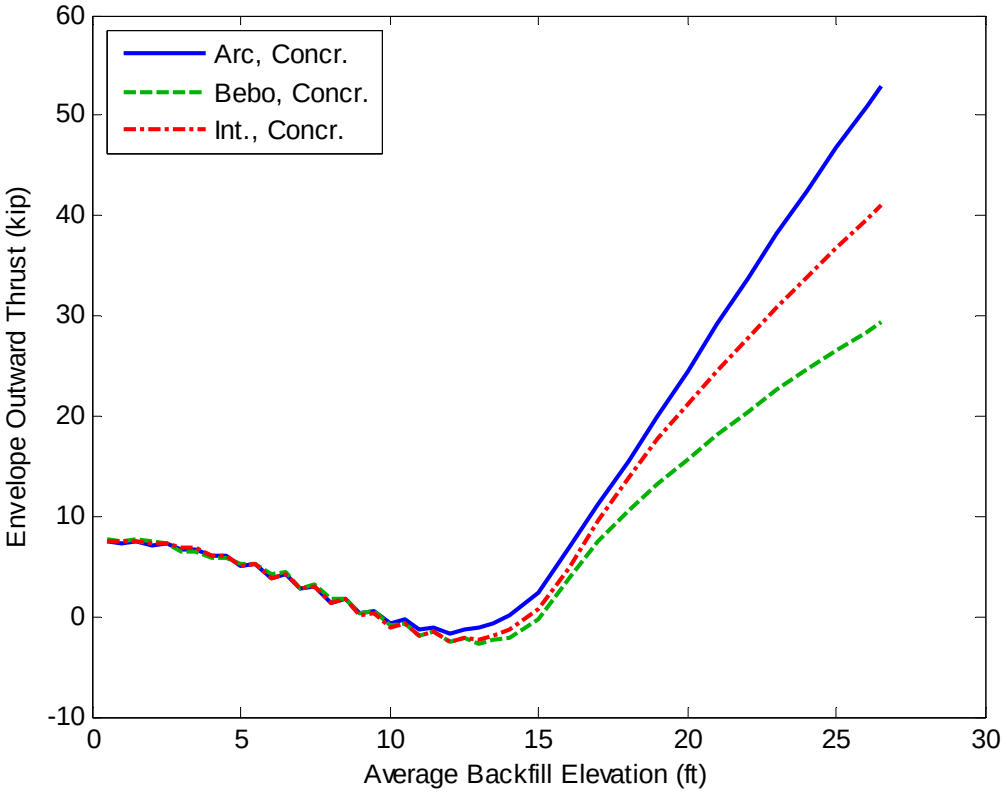

Figure 14 – Backfilling Envelope Outward Thrust for Various Geometric Configurations, Concrete Deck, 12.5 ft of Total Fill Above the Crown

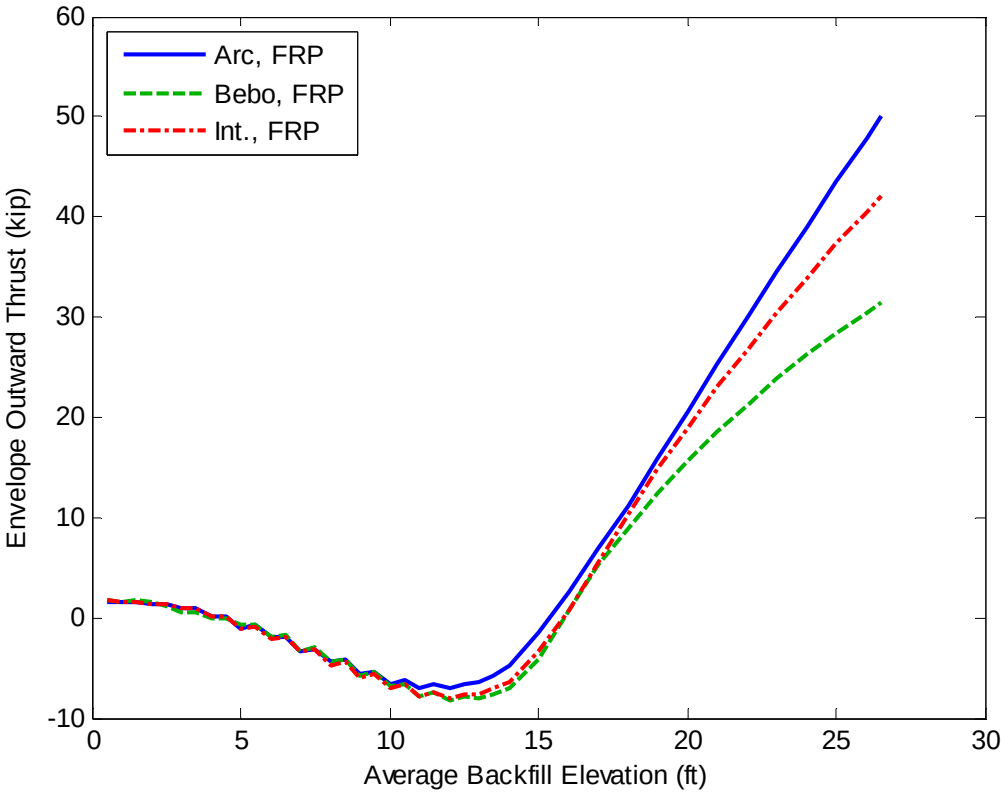

Figure 15 – Backfilling Envelope Outward Thrust for Various Geometric Configurations, FRP Deck, 12.5 ft of Total Fill Above the Crown

It is apparent from Figure 14 and Figure 15 that the outward thrust is generally greater for arc-shaped arches as compared to the Bebo arch for practically all levels of arch crown burial. Once again the response of the intermediate arch is in between the two others. This indicates that shapes that are relatively steeper near the supports and flatter near midspan are more effective at reducing foundation thrust loads.

AEWC Advanced Structures & Composites Center
5793 AEWC Bldg
University of Maine
Orono, ME 04469-5793

Telephone: 207-581-2123
FAX: 207-581-2074
contactaewc@umit.maine.edu
www.aewc.umaine.edu

Envelope Arch Axial Load

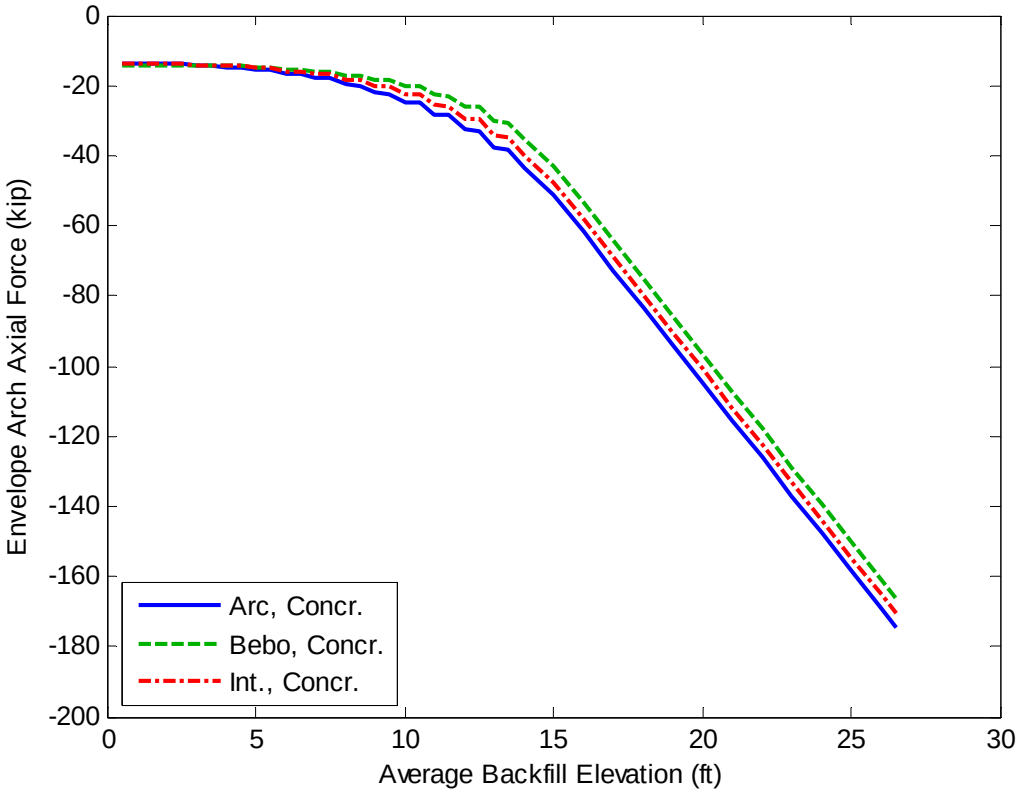

Figure 16 – Backfilling Envelope Arch Axial Load for Various Geometric Configurations, Concrete Deck, 12.5 ft of Total Fill above the Crown

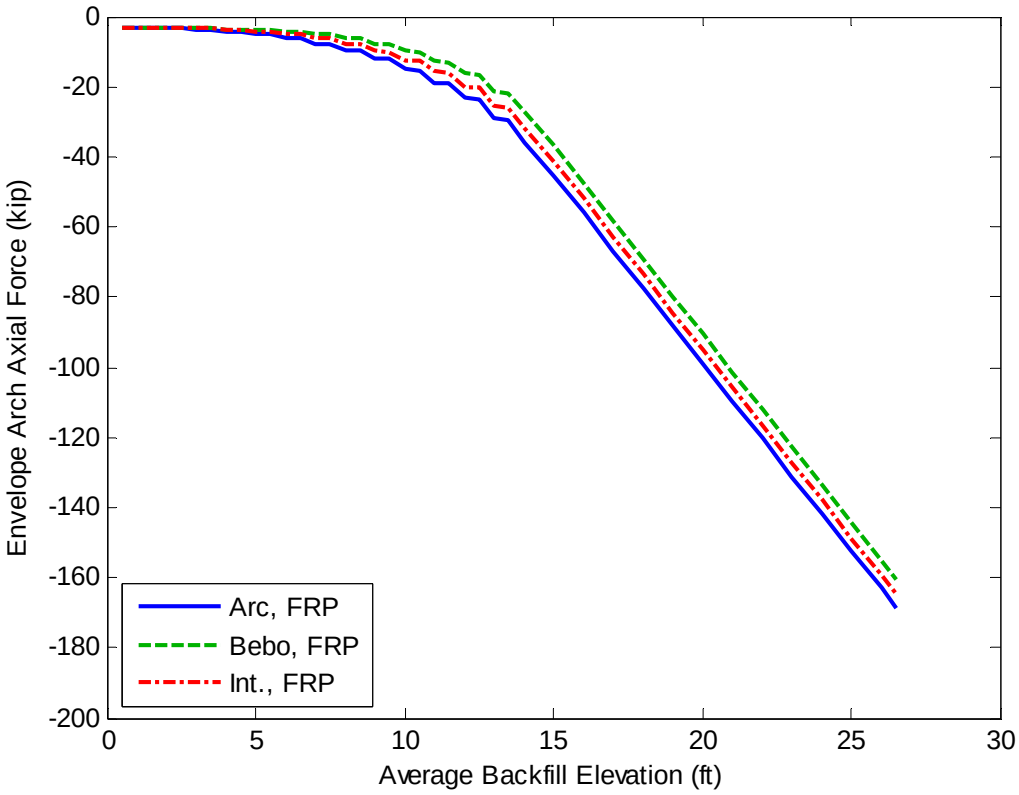

Figure 17 – Backfilling Envelope Arch Axial Load for Various Geometric Configurations, FRP Deck, 12.5 ft of Total Fill above the Crown

The maximum axial load level in the arch does not appear to be greatly affected by the shape of the arch based on Figure 16 and Figure 17, although the arc-shaped arch does carry slightly greater axial loads at all backfill levels.

Results: effect of live loading

The response due to live loading may control the design of the arch members, particularly for bridges with relatively low soil depth above the crown of the arch. The effect of soil-structure interaction on live loading was examined in this study by analyzing a variety of configurations as summarized in Table 4. Four different truck/position combinations provided by AIT were analyzed. The position refers to the front axle of the truck moving from left to right and the origin of the coordinate system is at midspan. Note that the positions referring to M+ in the right footing were actually applied with the truck

mirrored about midspan to maximize M+ in the left footing of the model. This was done because the positive moment is larger at the left footing due to staged backfilling. If staged backfilling were not considered, the foundation moments on each side of the arch due to construction would be equal. All analyses with live loading considered a final backfilling elevation of 15 ft (3 ft crown burial depth) unless otherwise noted. Service (unfactored) loads are used for all analyses.

Table 4 Matrix of Analyses to Examine the Effect of Arch Geometry

Truck and Position of Front Axle	**Maximizes**	**Arch Geometry**	**Decking**
Short Design Truck at 130 in (266 in Rev.)	M+ at right footing (M+ at left footing)	Circular Segment Arc	Concrete
Short Design Truck at 466 in	M- at right footing	ConSpan Bebo Arch	FRP-only
Tandem at -38 in (86 in Rev.)	M+ at right footing (M+ at left footing)	--	--
Tandem at 154 in	M- at right footing	--	--

Envelope Arch Moments

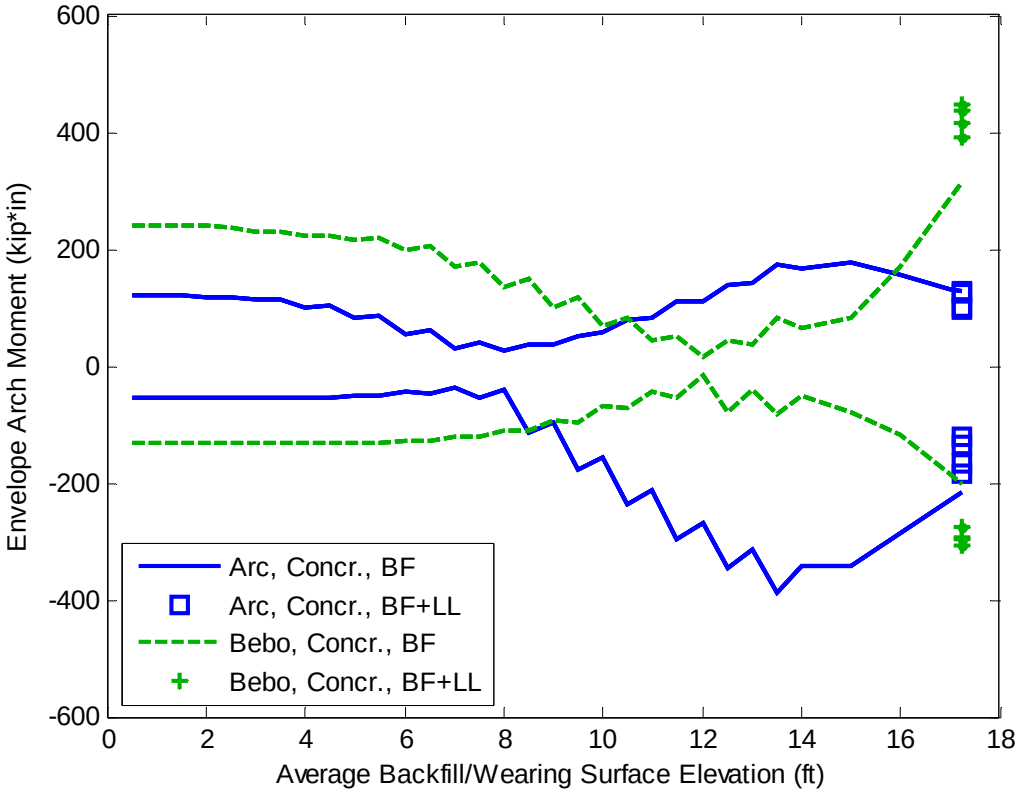

Figure 18 – Backfilling and LL Envelope Arch Moment for Arc and ConSpan (Bebo) Geometries (All 4 LL Analyses Shown for Each), Concrete Deck

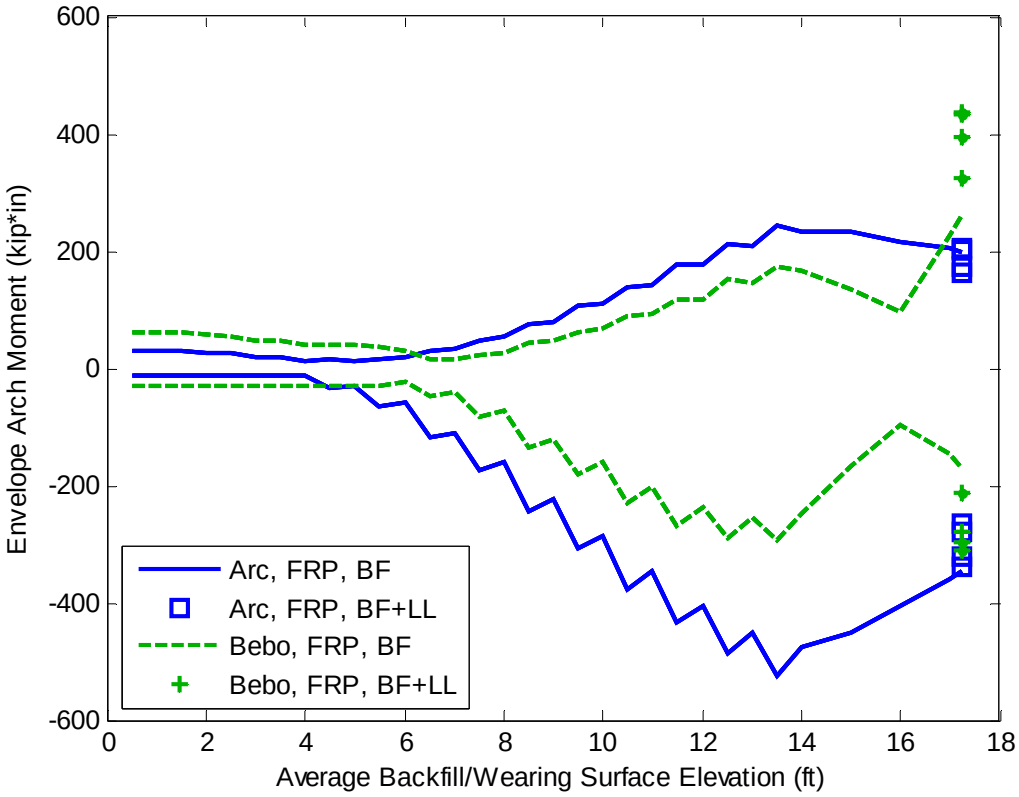

Figure 19 – Backfilling and LL Envelope Arch Moment for Arc and ConSpan (Bebo) Geometries (All 4 LL Analyses Shown for Each), FRP Deck

Interestingly, the magnitude of the arch moment due to live loading for the arc-shaped arches at all truck positions except one decreased as shown in Figure 18 and Figure 19. The one case that showed an increase in arch moment was only about 1%. This counter-intuitive result occurs because the crown burial depth is low (3 ft) and the arch is in such a position that it benefits from being "pushed back into place" by additional vertical loading (see Figure 7). On the other hand, the arch moment magnitudes increase for all possible scenarios with the Bebo arch. This indicates that the arc-shaped arch is more effective for resisting moment due to live loads at low crown burial depths.

Outward Foundation Thrust

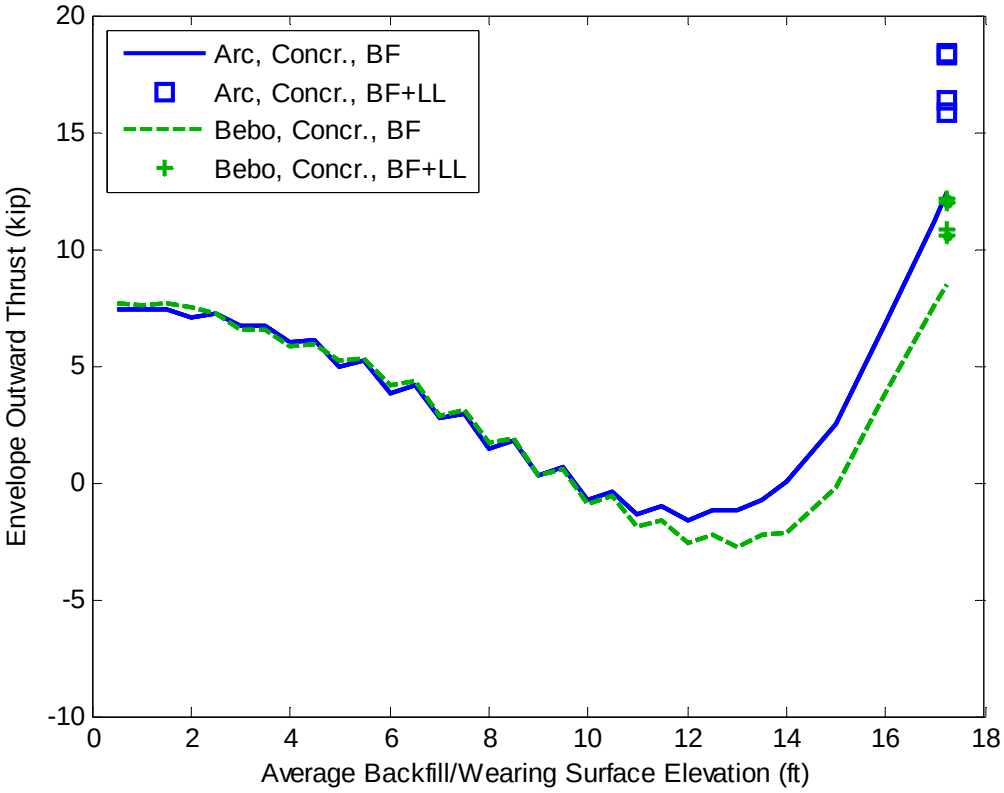

Figure 20 – Backfilling and LL Envelope Outward Thrust for Arc and ConSpan (Bebo) Geometries (All 4 LL Analyses Shown for Each), Concrete Deck

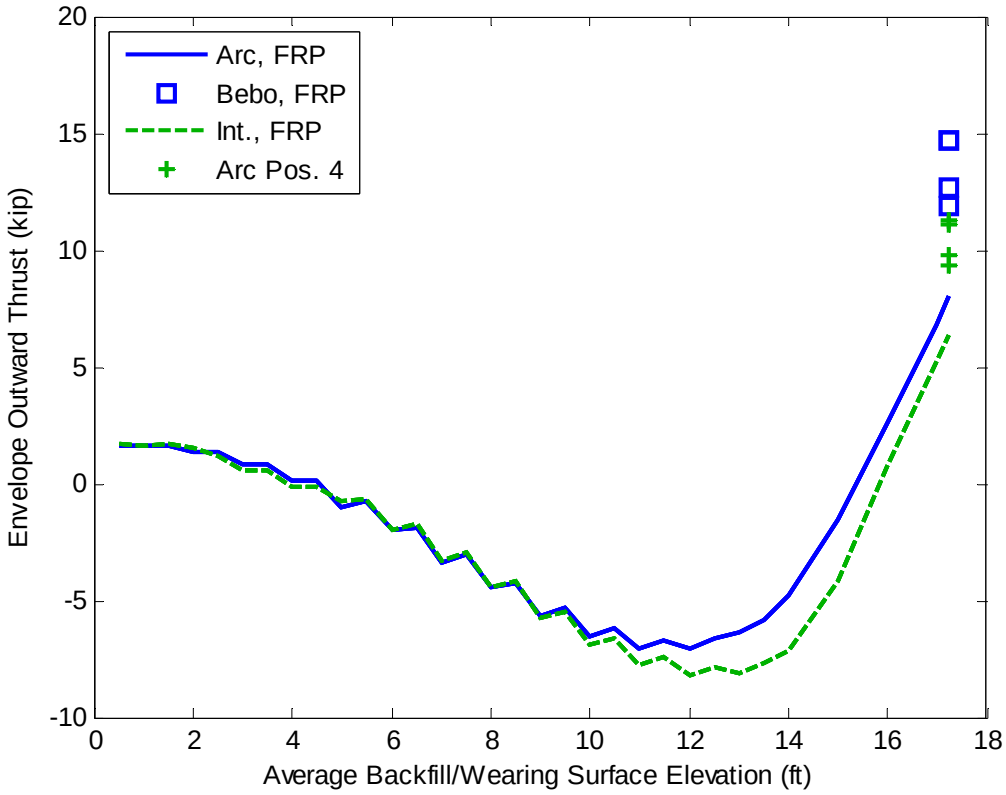

Figure 21 – Backfilling and LL Envelope Outward Thrust for Arc and ConSpan (Bebo) Geometries (All 4 LL Analyses Shown for Each), FRP Deck

It is apparent from Figure 20 and Figure 21 that the outward thrust is generally greater for arc-shaped arches as compared to the Bebo arch for practically all backfill and live load levels. This indicates that shapes that are relatively steeper near the supports and flatter near midspan are more effective at reducing foundation thrust loads due to backfilling and live loads.

Envelope Arch Axial Load

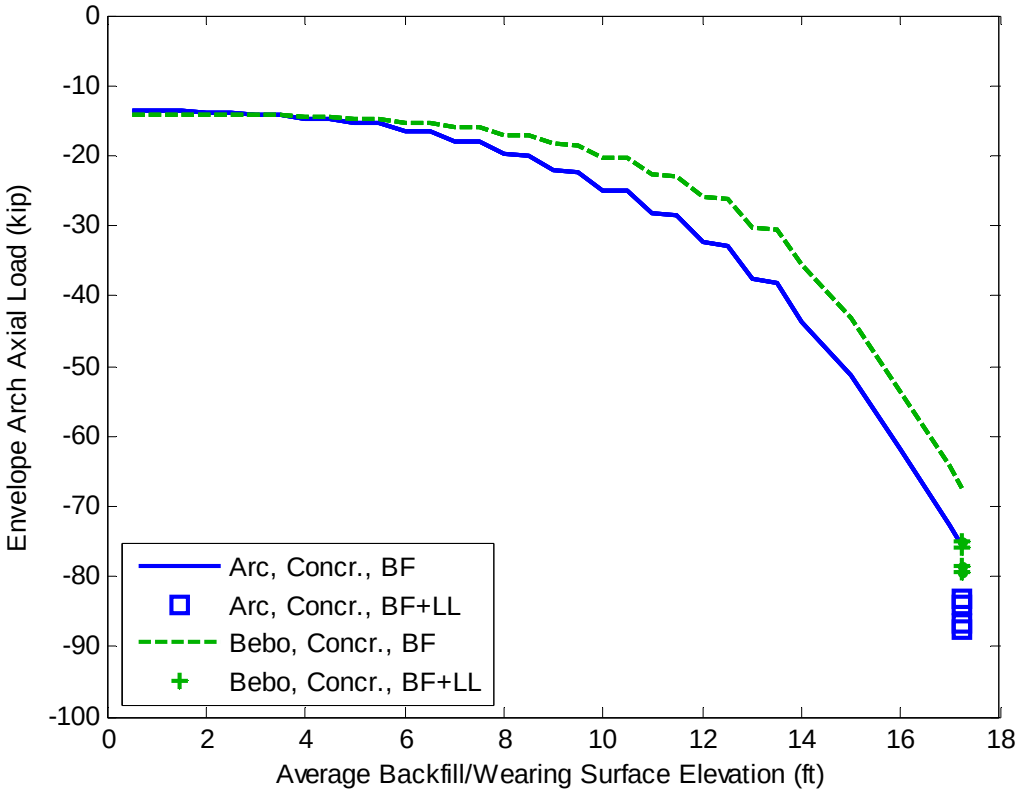

Figure 22 – Backfilling and LL Envelope Arch Axial Load for Arc and ConSpan (Bebo) Geometries (All 4 LL Analyses Shown for Each), Concrete Deck

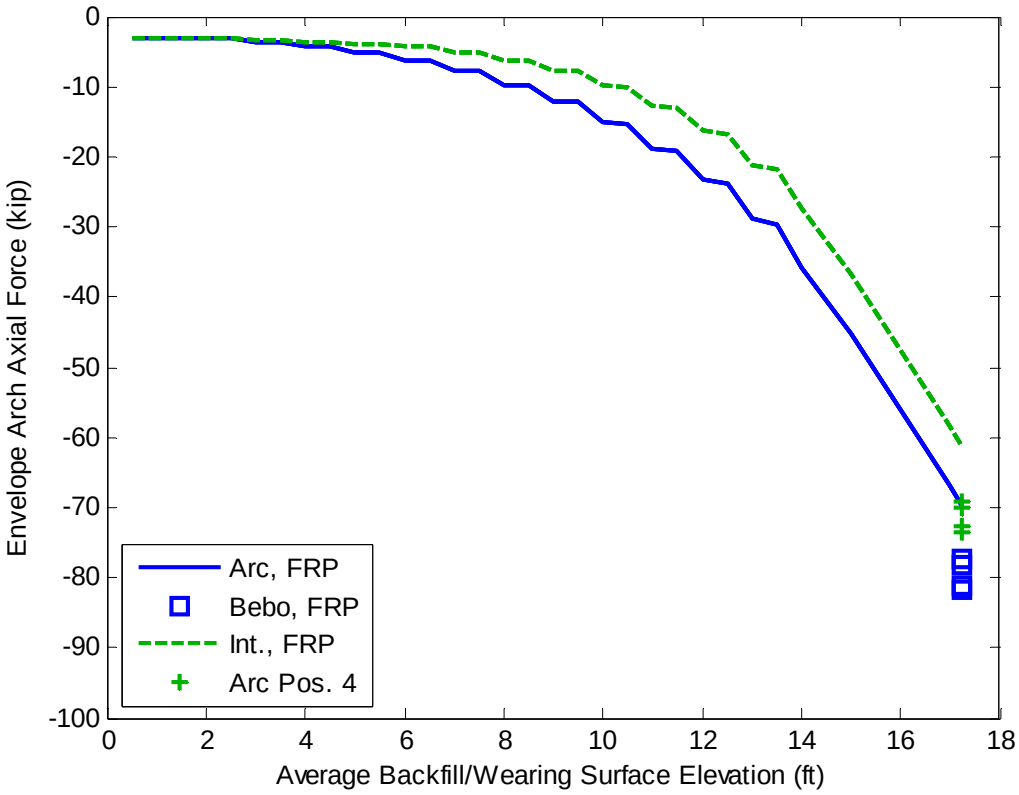

Figure 23 – Backfilling and LL Envelope Arch Axial Load for Arc and ConSpan (Bebo) Geometries (All 4 LL Analyses Shown for Each), FRP Deck

The change in axial load level in the arch due to live loading appears to be very similar for both arch shapes based on Figure 22 and Figure 23. Again the arc-shaped arch carries greater axial loads at all backfill levels.

Relative effect of soil springs

All analysis results presented to this point have utilized the procedure developed as part of this study with nonlinear soil springs. It is of interest to directly compare these results with those that would be generated with existing analysis code that does not consider nonlinear soil springs. A limited set of results is presented here to examine this.

Envelope Arch Moment

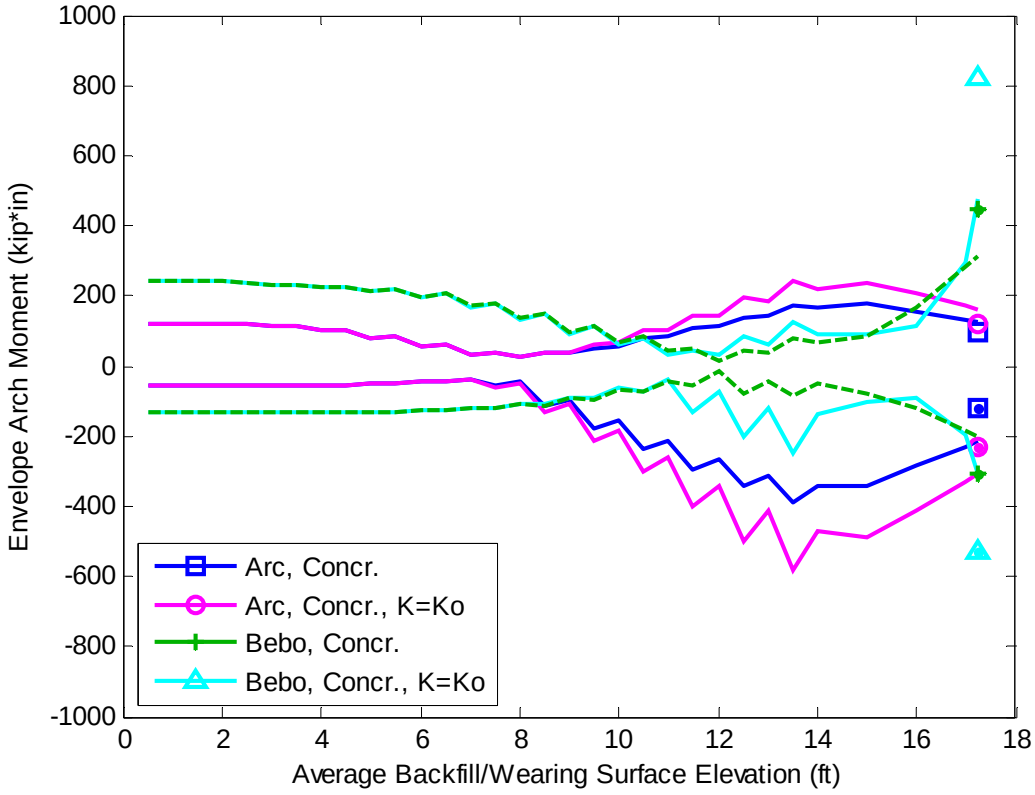

Figure 24 – Effect of Soil Springs on Backfilling and LL Moment, Concrete Deck, 3 ft of Backfill above the Crown

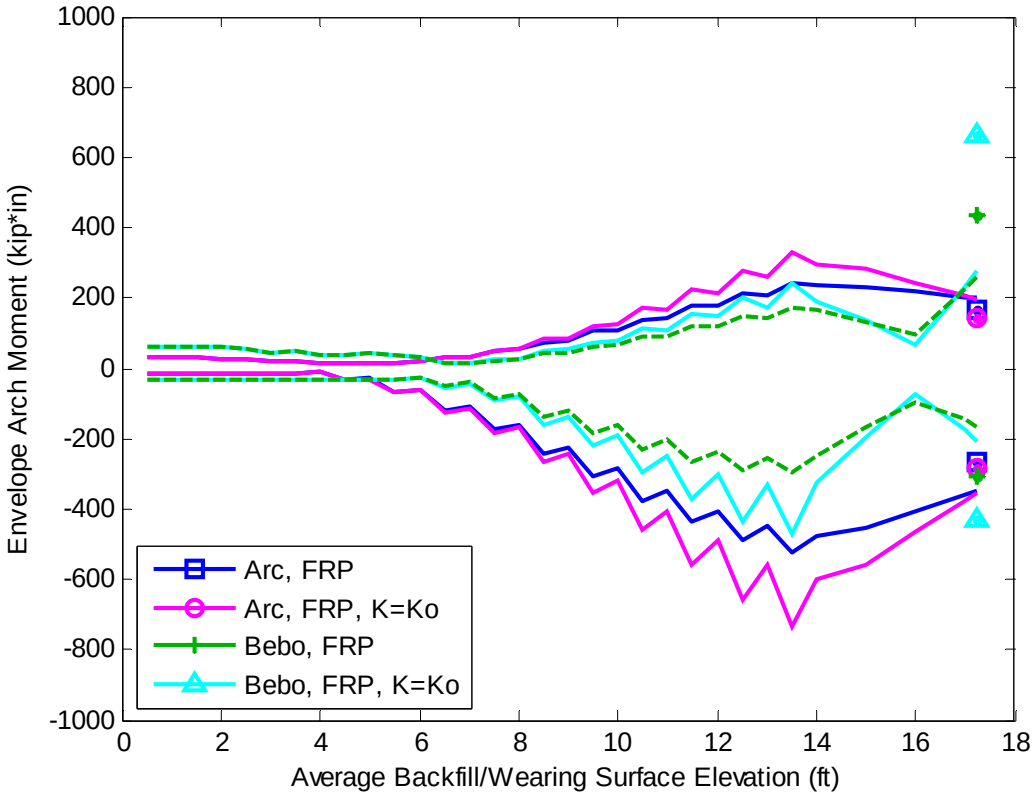

Figure 25 – Effect of Soil Springs on Backfilling and LL Moment, FRP Deck, 3 ft of Backfill above the Crown

It is apparent from Figure 24 and Figure 25 that the arch bending moment in both the arc-shaped arch and the Bebo arch are significantly reduced by considering the nonlinear soil spring relationship. The peak bending moment magnitudes and relative difference between the two types of arches are presented in Table 5. For all scenarios presented, the nonlinear soil spring relationship results in a reduction in arch bending moment of 26-46%.

Table 5 Peak Moment Magnitudes and Relative Differences Due to the Consideration of Nonlinear Soil Springs, 3 ft of Backfill above the Crown

		Arc			Bebo		
Deck	**Param**	**Nonlinear**	**K = Ko**	**Diff.**	**Nonlinear**	**K = Ko**	**Diff.**
Concr.	M+ (kip*in)	176	244	28%	447	823	46%
	M- (kip*in)	-386	-583	34%	-306	-532	42%

FRP	M+ (kip*in)	243	328	26%	436	666	35%
	M- (kip*in)	-523	-736	29%	-309	-470	34%

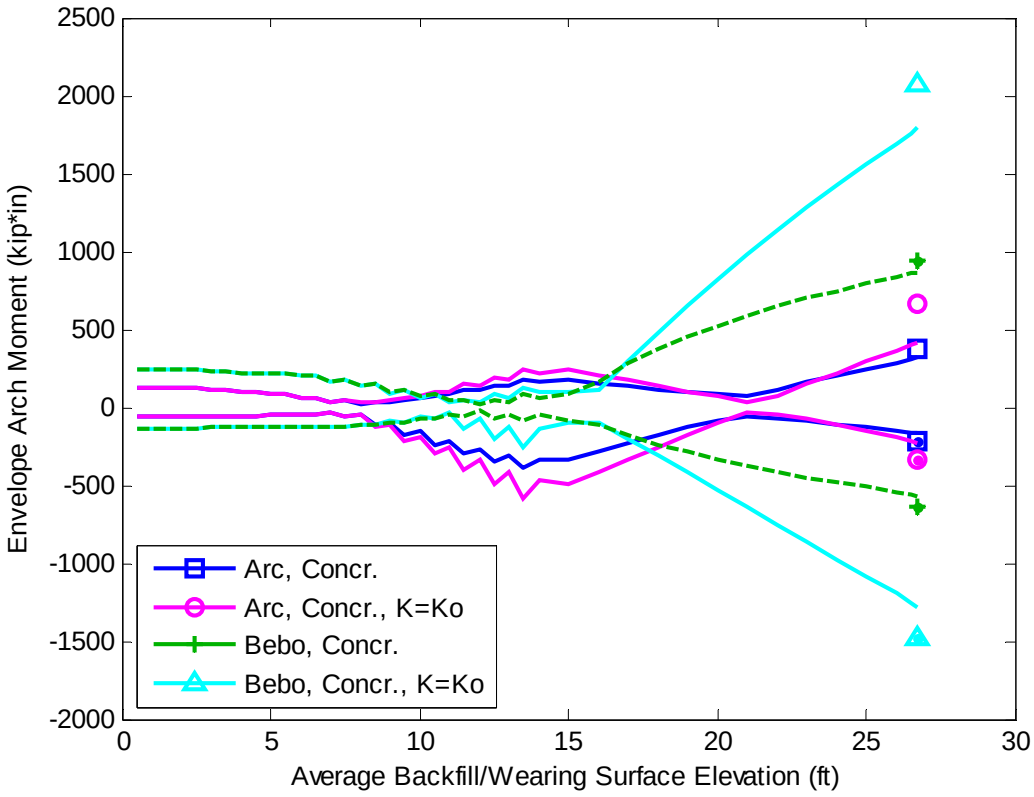

Figure 26 – Effect of Soil Springs on Backfilling and LL Moment, Concrete Deck, 12.5 ft of Backfill above the Crown

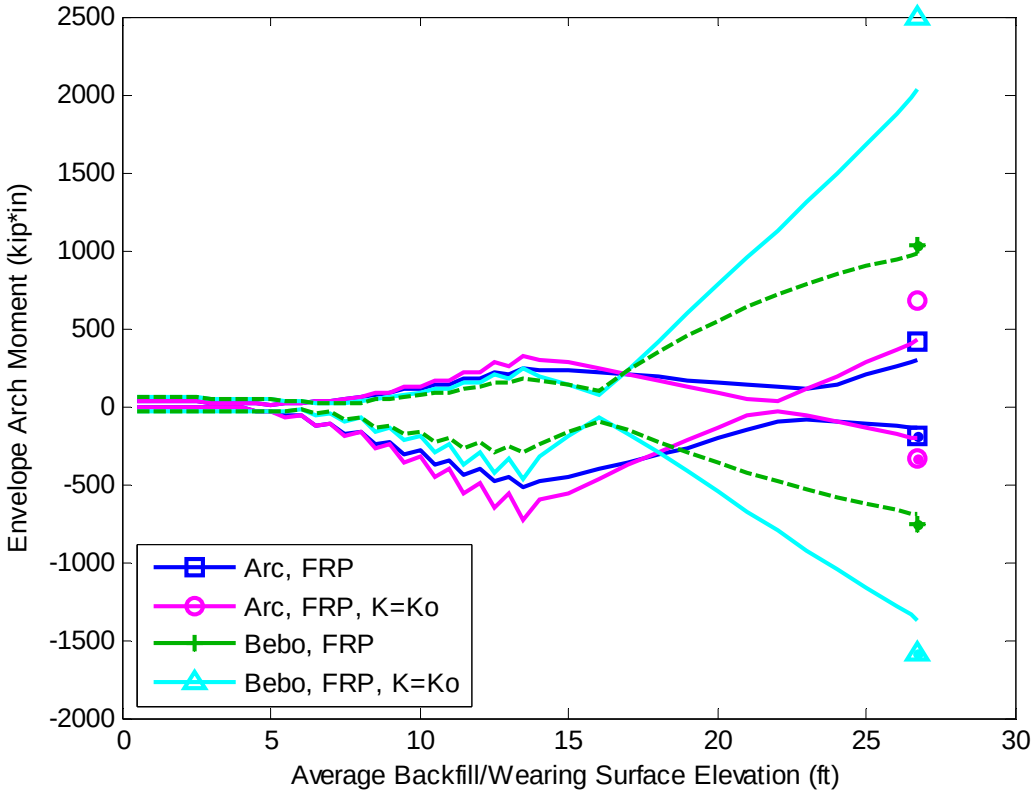

Figure 27 – Effect of Soil Springs on Backfilling and LL Moment, FRP Deck, 12.5 ft of Backfill above the Crown

It is apparent from Figure 26 and Figure 27 that the arch bending moment in both the arc-shaped arch and the Bebo arch are significantly reduced by considering the nonlinear soil spring relationship. The peak bending moment magnitudes and relative difference between the two types of arches are presented in Table 6. For all scenarios presented, the nonlinear soil spring relationship results in a reduction in arch bending moment of 37-59%.

Table 6 Peak Moment Magnitudes and Relative Differences Due to the Consideration of Nonlinear Soil Springs, 12.5 ft of Backfill above the Crown

		Arc			Bebo		
Deck	**Param**	**Nonlinear**	**K = Ko**	**Diff.**	**Nonlinear**	**K = Ko**	**Diff.**
Concr.	M+ (kip*in)	379	664	43%	935	273	55%
	M- (kip*in)	-212	-334	37%	-633	-1481	57%

FRP	M+ (kip*in)	417	674	38%	1032	2500	59%
	M- (kip*in)	-196	-340	42%	-762	--1581	52%

AEWC Advanced Structures & Composites Center
5793 AEWC Bldg
University of Maine
Orono, ME 04469-5793

Telephone: 207-581-2123
FAX: 207-581-2074
contactaewc@umit.maine.edu
www.aewc.umaine.edu

Envelope Outward Thrust

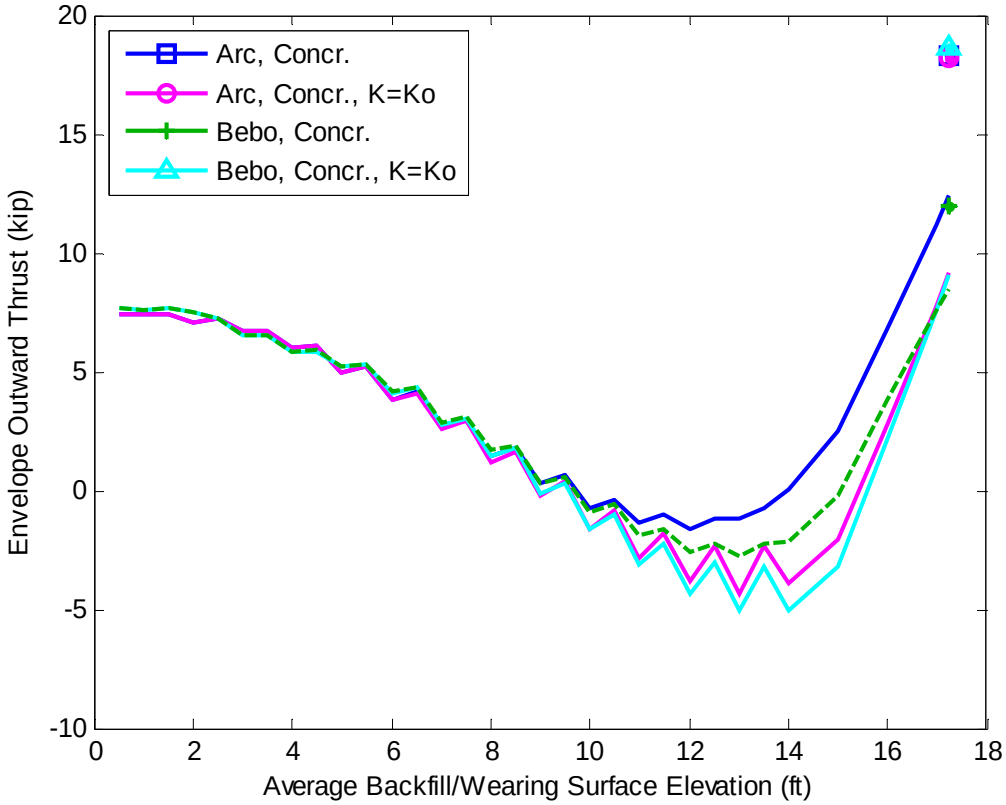

Figure 28 – Effect of Soil Springs on Backfilling and LL Thrust, Concrete Deck, 3 ft of Backfill above the Crown

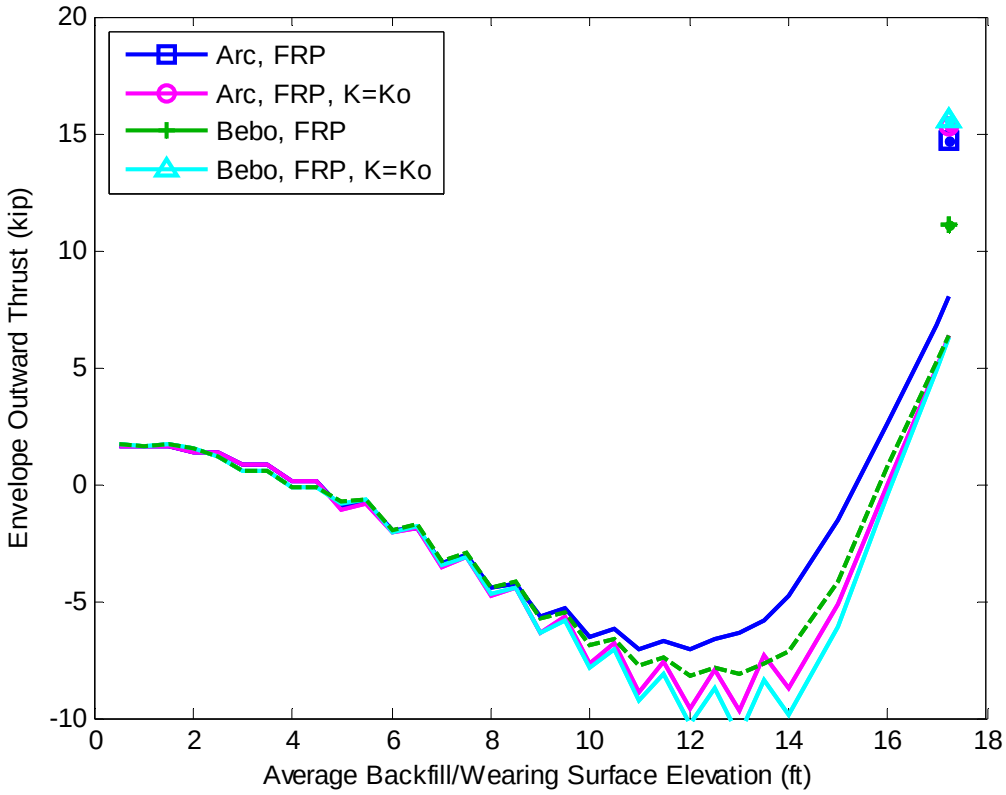

Figure 29 – Effect of Soil Springs on Backfilling and LL Thrust, FRP Deck, 3 ft of Backfill above the Crown

The outward thrust magnitude is reduced 29-36% when considering a nonlinear soil spring relationship for the Bebo arch, but it has practically no effect on the arc-shaped arch as shown in Table 7. The reason for the lack of significant benefit with respect to outward thrust with the arc-shaped arch is that many of the soil springs are actually still in the active state (i.e. K < Ko) at a backfill depth of the 3 ft. After the application of live loads, which causes K to increase, the response is similar to that for linear soil springs (K = Ko). As shown next, the soil-springs are more effective for larger crown burial depths.

Table 7 Peak Outward Thrust Magnitudes and Relative Differences Due to the Consideration of Nonlinear Soil Springs, 3 ft of Backfill above the Crown

		Arc			Bebo		
Deck	**Param**	**Nonlinear**	**K = Ko**	**Diff.**	**Nonlinear**	**K = Ko**	**Diff.**

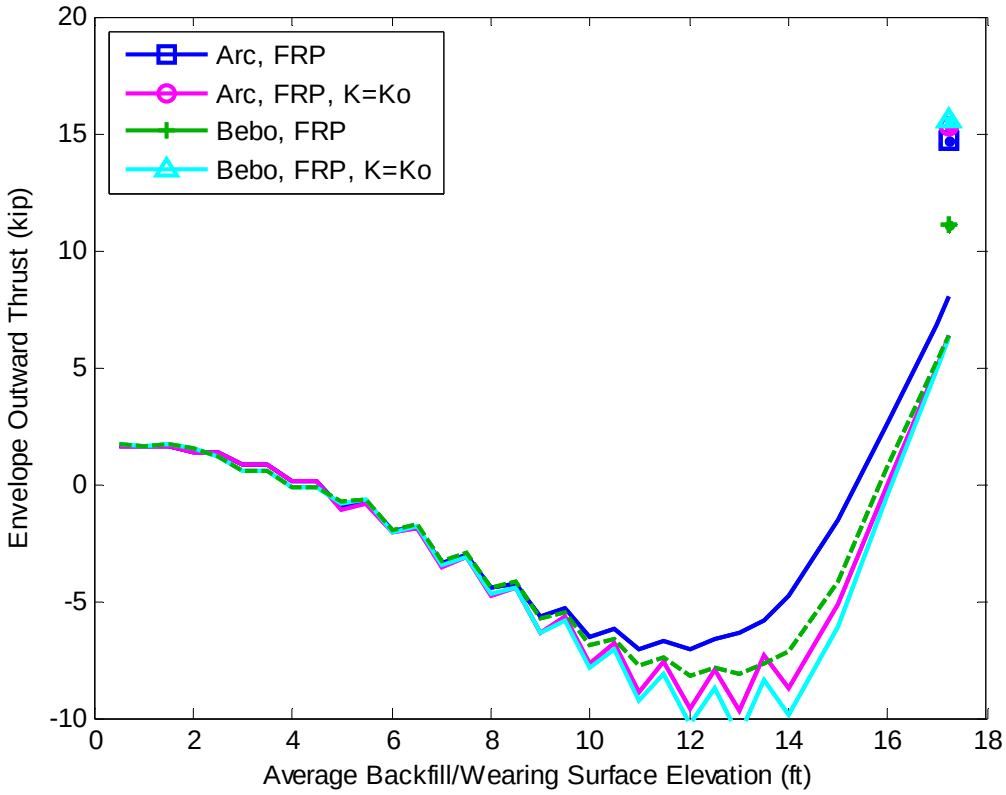

Figure 29 – Effect of Soil Springs on Backfilling and LL Thrust, FRP Deck, 3 ft of Backfill above the Crown

The outward thrust magnitude is reduced 29-36% when considering a nonlinear soil spring relationship for the Bebo arch, but it has practically no effect on the arc-shaped arch as shown in Table 7. The reason for the lack of significant benefit with respect to outward thrust with the arc-shaped arch is that many of the soil springs are actually still in the active state (i.e. K < Ko) at a backfill depth of the 3 ft. After the application of live loads, which causes K to increase, the response is similar to that for linear soil springs (K = Ko). As shown next, the soil-springs are more effective for larger crown burial depths.

Table 7 Peak Outward Thrust Magnitudes and Relative Differences Due to the Consideration of Nonlinear Soil Springs, 3 ft of Backfill above the Crown

		Arc			Bebo		
Deck	**Param**	**Nonlinear**	**K = Ko**	**Diff.**	**Nonlinear**	**K = Ko**	**Diff.**

Concr.	Outward Thrust	18.3	18.2	-1%	11.9	18.7	36%
FRP	Outward Thrust	14.7	15.3	4%	11.1	15.6	29%

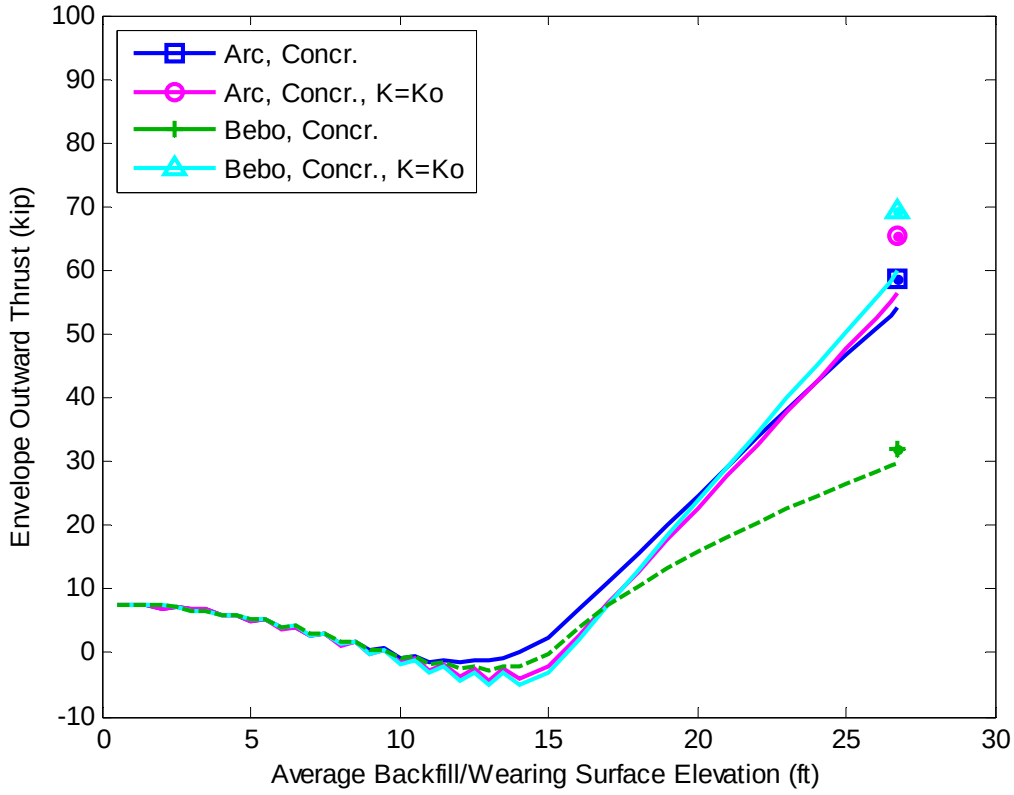

Figure 30 – Effect of Soil Springs on Backfilling and LL Thrust, Concrete Deck, 12.5 ft of Backfill above the Crown

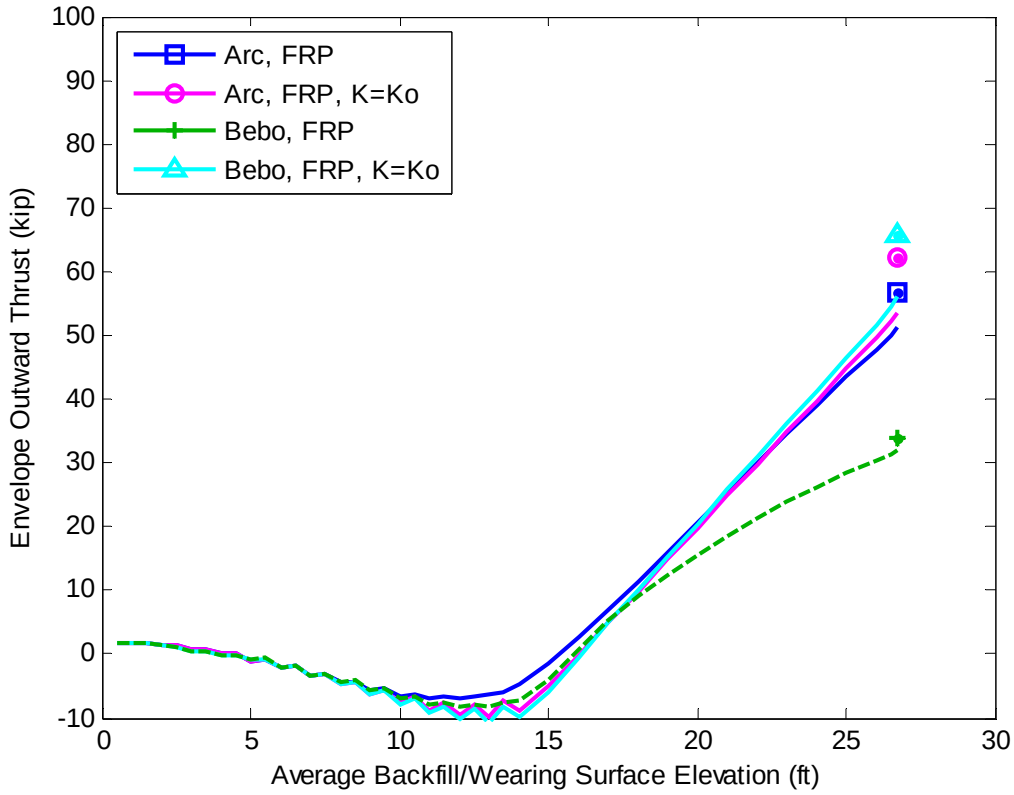

Figure 31 – Effect of Soil Springs on Backfilling and LL Thrust, FRP Deck, 12.5 ft of Backfill above the Crown

The outward thrust magnitude is reduced 48-54% when considering a nonlinear soil spring relationship for the Bebo arch, but only 8-10% for the arc-shaped arch as shown in Table 8 for a crown burial depth of 12.5 ft. This indicates that the use of nonlinear soil springs provides more benefit for the Bebo arch than the arc-shaped arch with respect to the improvement in foundation thrust. Additional improvement may be mobilized for both shapes when other types of foundations are considered (e.g. spread footings free to translate instead of the perfectly fixed foundations that are assumed in these analyses).

Table 8 Peak Outward Thrust Magnitudes and Relative Differences Due to the Consideration of Nonlinear Soil Springs, 12.5 ft of Backfill above the Crown

		Arc			Bebo		
Deck	**Param**	**Nonlinear**	**K = Ko**	**Diff.**	**Nonlinear**	**K = Ko**	**Diff.**
Concr.	Outward Thrust	58.8	65.4	10%	69.3	31.9	54%

FRP	Outward Thrust	56.9	62.3	8%	65.8	33.9	48%

Envelope Arch Axial Load

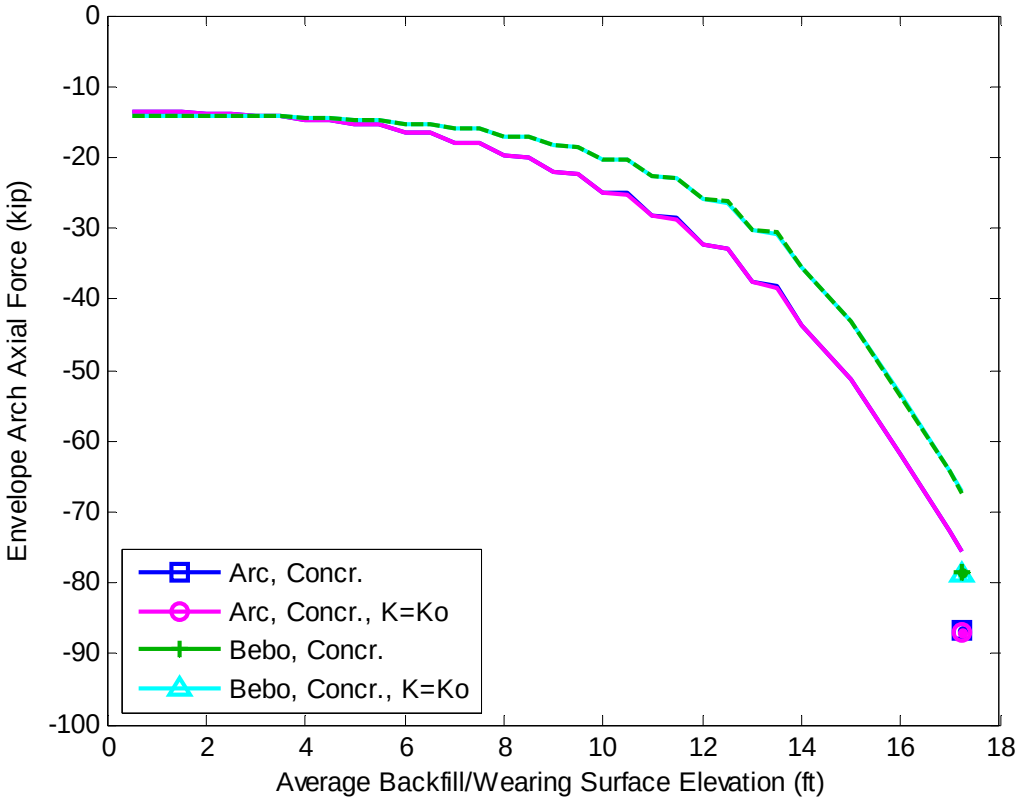

Figure 32 – Effect of Soil Springs on Backfilling and LL Arch Axial Loads, Concrete Deck, 3 ft of Backfill above the Crown

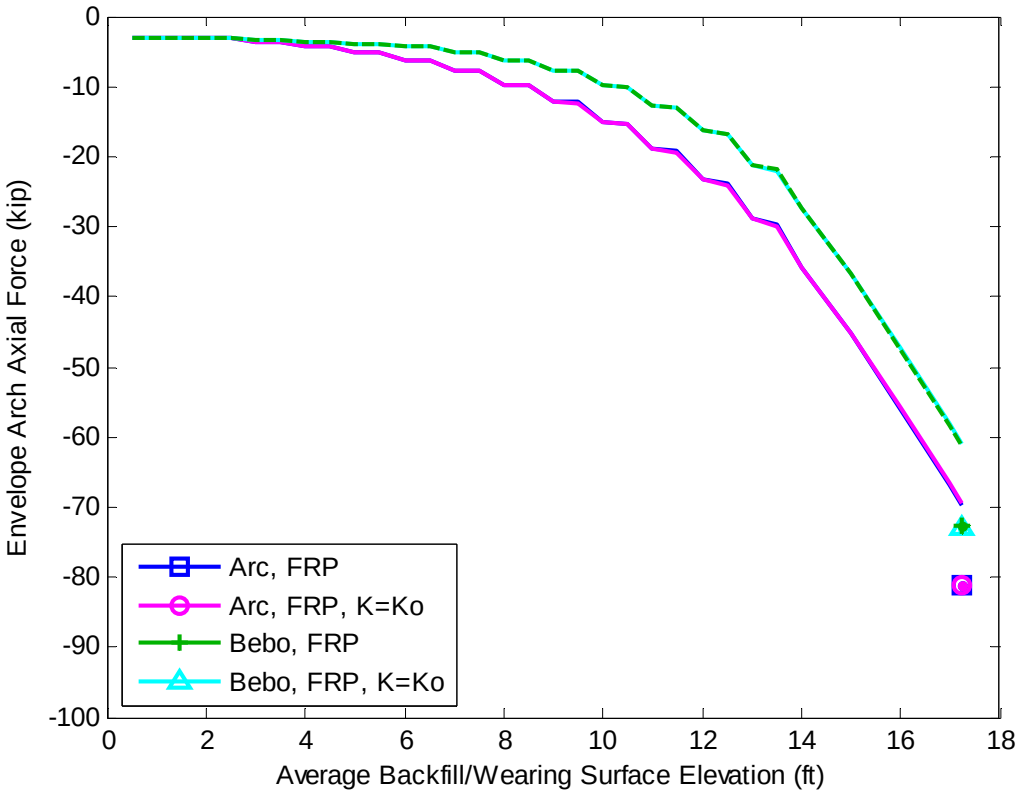

Figure 33 – Effect of Soil Springs on Backfilling and LL Arch Axial Loads, FRP Deck, 3 ft of Backfill above the Crown

The peak magnitude of arch axial force is practically unaffected by the soil spring relationship as shown in Figure 32, Figure 33, and Table 9. The difference in response is less than 1%.

Table 9 Peak Arch Axial Force Magnitudes and Relative Differences Due to the Consideration of Nonlinear Soil Springs, 3 ft of Backfill above the Crown

		Arc			Bebo		
Deck	**Param**	**Nonlinear**	**K = Ko**	**Diff.**	**Nonlinear**	**K = Ko**	**Diff.**
Concr.	Arch Axial Force (kip)	-78.6	-78.9	0.4%	-86.8	-87.1	0.3%
FRP	Arch Axial Force (kip)	-72.7	-72.9	0.3%	-81	-81.1	0.1%

AEWC Advanced Structures & Composites Center
5793 AEWC Bldg
University of Maine
Orono, ME 04469-5793

Telephone: 207-581-2123
FAX: 207-581-2074
contactaewc@umit.maine.edu
www.aewc.umaine.edu

Summary and conclusions

MATLAB-based structural analysis code has been developed to capture the effects of nonlinear soil springs, staged construction, decking stiffness, and longitudinal benefit from concrete decking. The effect of staged backfilling, arch geometry, and live loading was investigated by analyzing a variety of configurations that are representative of a proposed (or previously constructed) bridge project. Input parameters were based on values provided by AIT and were primarily based on the proposed Ellsworth Bridge project.

The following conclusions were drawn from results of analyses:

Staged Backfilling

1. Alternating soil lifts resulted in side-sway and non-symmetric response about midspan.
2. Staged backfilling allowed lateral earth pressure coefficients other than the at-rest coefficient to be rationally considered.
3. Staged backfilling allowed the structural response to be tracked throughout the construction period.
4. The bending moment response for the arch with the nonlinear bending stiffness relationship generally fell between those for the linear cracked arch and the linear uncracked arch.
5. The maximum moment during backfilling sometimes occurred at a point prior to the last construction load step depending on the total backfill level.
6. The type of arch bending stiffness considered did not have a large effect on the outward thrust.
7. The outward thrust was initially larger for the concrete-decked arches compared to the FRP-decked arches due to the increased self-weight.
8. The type of arch bending stiffness had practically no effect on the maximum axial load in the arch.

Arch Geometry

1. The shape of the arch had a large effect on the moment developed within the arch (total span and rise were held constant). Shapes that were steeper near supports and flatter near midspan (Bebo) resulted in much larger bending moments at large burial depths.

2. At shallow burial depths, the moments were largest in the arc-shaped arch and least for the Bebo arch, which may indicate that the optimal shape is dependent on crown burial depth.
3. The outward foundation thrust was greatest for the arc-shaped arch and least for the Bebo arch at all levels of backfilling.
4. The axial load in the arch was minimally affected by the arch shape, although the axial load in the Bebo arch was smaller for all levels of backfilling.

Live Loading

1. The magnitude of moment in the arc-shaped arch decreased as live loads were applied. This counter-intuitive result occurs when the crown burial depth is low (3 ft) and the arch is in such a position that it benefits from being "pushed back into place" by additional vertical loading (see Figure 7).
2. The magnitude of moment in the Bebo arch increased as live loads were applied, which may indicate that the arc-shaped arch is more effective for resisting moment due to live load at low crown burial depths.
3. The outward thrust due to live loading is greater for arc-shaped arches than the Bebo arch.
4. The change in axial load level due to live loading was similar for both arches. The total axial loads were larger in the arc-shaped arch compared to the Bebo arch.

Relative Effect of Soil Springs

1. The use of nonlinear soil springs resulted in 26-59% lower arch bending moments.
2. Outward thrust was reduced by 29-54% for the Bebo arch. Less significant differences of around 0-10% were noted for the arc-shaped arch. It is expected that the relative effect of the soil-springs with respect to outward thrust will be reduced further for arches with other types of foundations that allow lateral movements (e.g. spread footings or pile-supported foundations).
3. The soil springs had practically no effect on the axial load level in the arches.

In summary, the consideration of nonlinear soil springs, the 3D effect of transverse decking stiffness, staged backfilling, and various arch geometries was shown to have a significant effect on the critical response values that would be used to design bridge structures. Many of the critical response values were reduced significantly by considering

nonlinear soil springs. It was also shown that the arch geometry had a large effect on critical response values. The software developed as part of this project will provide a valuable tool to bridge designers in their efforts to optimize designs to achieve desired effects and ultimately improve the economic efficiency of these structures.

Task 2.2 Improved decking design

Efficient design of this bridge system needs to incorporate a greater spacing of the arches. The largest barrier to this has been the inability of the FRP decking product to span between the arches and carry the loads through the soil to the arches. At this time a new decking design was investigated to improve on the Enduro Composites Tuff Span decking as well as the cast-in-place (CIP) concrete deck used on all the bridges to date. This stronger decking material allows for a greater spacing of the carbon fiber reinforced arches. Increasing the spacing of the arches decreases cost and could potentially eliminate the concrete overlay presently used. Additionally, using structural CIP concrete is time consuming and expensive because of the rebar placement and cure time required. This work aimed at identifying commercial products that would allow arches to be spaced up to 6 feet on center with anticipated future geometries and at-rest soil pressures. This new decking product would also be much more durable and be expected to withstand significant damage without compromising the integrity of the structure.

Several panel products with the capacity to span between the arches were identified. Only one product found was to be able to conform to an arch shape. The products investigated include DuraSpan by Martin Marietta Composites, ZellComp FRP bridge decks, Superdeck by Creative Pultrusions, and SuperRail by Creative Pultruions. All of the products are rigid wide flat panels that are intended for typical girder systems except for SuperRail. DuraSpan is a commercially available bridge deck system in use as a direct replacement for concrete decks over steel girders. ZellComp FRP bridge decks are similar. Images of these two products can be seen in Figure 34 and Figure 35.

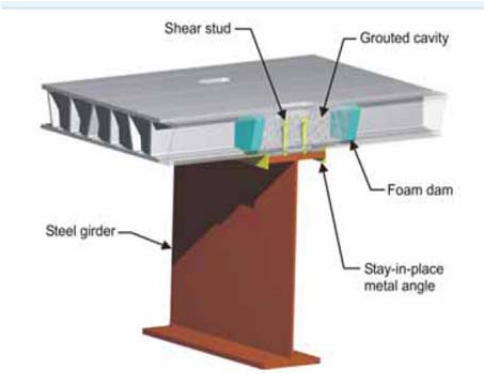

Figure 34 – DuraSpan Cross-section

Figure 35 – ZellComp During Construction

Other composite roofing deck products similar to the Enduro Composites, TuffSpan roof deck product were also investigated. There are several products available but do not have the strength to span between the arches with the soil pressures anticipated for these structures. These other products include corrugated composite roof panels such as Suntuf and Palruf. They are available commercially but are weak and intended for only minor spans and light loading.

Panels that could conform to an arch shape were analyzed as beam elements with a unit width. Simplified, conservative loads were used in the Neal Bridge analysis. This analysis found a maximum total service soil pressure of 1725 psf (Goslin 2009). This value was used for analysis of panels in initial screening calculations.

A product was identified that met the goals previously described. The SuperRail Composite Guardrail is manufactured and sold by Creative Pultrusions, Inc. and has been approved by FHWA as a guardrail system (Baxter 2003). Two components were included in the evaluating the feasibility of this decking system: 1) structural analysis of this system under the uniform soil and bearing loads and 2) determination of whether this panel will conform to the arch shape of the FRP tubular members.

Creative Pultrusions provided calculations that included predicted deflections and a 3D finite element analysis on their product in an arrangement similar to the Ellsworth bridge to be replaced in 2011 with the Bridge-in-a-Backpack™. The analysis was conducted to evaluate the product for its feasibility in use as part of the bridge system. Loads were provided by AIT. The analysis showed a soil pressure of roughly 49.3 psi at ultimate failure of the decking. The failure mode at this load was web buckling at the bearing of

each panel assuming there is no stiffener or panel overlap at this location, which is shown in Figure 36.

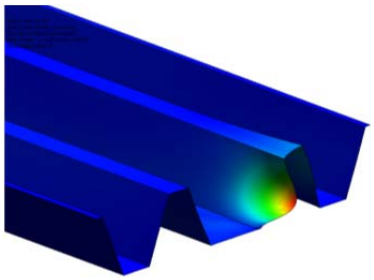

Figure 36 – Deformed shape of panel at failure from FE analysis (courtesy of Creative Pultrusions, Inc.)

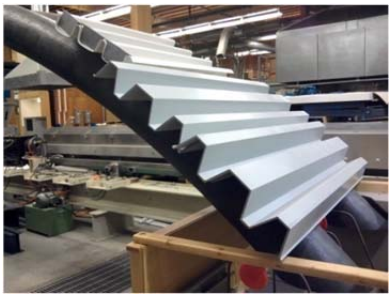

Figure 37 - Mock up of Composite Decking

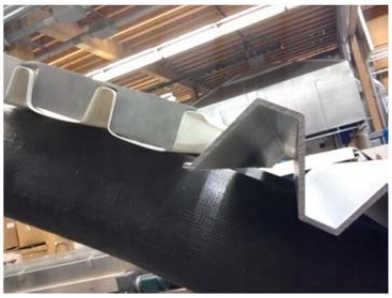

Figure 38 - Elevation of "New" & "Old" Decking

A section of the decking on a mock up in the lab can be seen in Figure 37 and Figure 38. A mockup of a bridge section was completed to evaluate whether the decking would conform to an arch shape, and could be installed successfully. This product conformed relatively well. It is very rigid in the weak axis of the panel but is narrow enough that for most radii of curvature the straight panel sections can be attached and conformed to the arch shape. Tuff Span and SuperRail properties are shown in Table 10 with a factor of safety of 2.5 for comparisons and analyzed for a typical buried arch section with a 24" cover at the crown. Deep sections were ignored where higher soil loads control.

Table 10 – Summary of Panel Products

Product	Moment Capacity (kip-in/ft)	Bearing Capacity (kip/ft)	Achievable Span (ft-in)	Conforms Easily to Arch Shape
Tuff Span (Bannon 2009)	12.4	2.1	3'-0"	Yes
SuperRail (Mostoller 2011)	114.4	34.0	6'-0" +	Yes
PalRuf/SunTuf	Negligible	Negligible	Negligible	Yes
DuraSpan	Not available	Not available	10'-0"	No
Superdeck (Creative Pultrusion 2011)	314	32	9'-0"	No
ZellComp (Richards 2011)	384	38	Not available	No

The strength and stiffness of this panel in the transverse direction of the bridge (longitudinal and strong axis of the panel) can be compared to the Tuff Span 8.0 Series 700 panel in the same direction. The stiffness of the CP-155 panel, EI, in the panel longitudinal direction is conservatively 82,160 kip-in^2 and the Tuff Span panel is published to be 5,850 kip-in^2(Enduro Composites 2009). The flexural compressive strength of the CP-155 in the direction of the deck span is reported to be 68 ksi (Mostoller 2011). The flexural strength of the Tuff Span 8.0 Series 700 panel is published as 55 ksi.

The Creative Pultrusions FRP decking product meets the need of stronger and thicker FRP product to span between the arches and conform to an arch shape. This eliminates the large expense of designing a custom FRP shape and tooling. This product will allow for the elimination of a concrete deck with the addition of a waterproofing solution at the seams of the panels. AEWC will continue to look for products that fit this need as new products are introduced to the market, but at this time CP-155 is the best product available for this use.

Task 2.3 Advanced modeling tools

Compression of Hollow FRP

The rigidified carbon fiber arch system relies on concrete for compression capacity and shape stability. The system was designed as a cast in place concrete application with the arch structure serving as formwork. While serving this function, the concrete adds no

capacity to the arch and the shell must carry construction loads – including wet concrete, workers, decking, and any equipment – until the concrete has cured. While the construction loads are much lower than the long term loads on the arch, the hollow strength and out of plane stiffness are much lower than that of the concrete-filled arch and local buckling of the shell wall during filling may be more critical than long term strength for some arch geometries.

According to Seide and Weingarten (1961), the short-column compression and bending capacities of a hollow shell are equivalent because both failures are controlled by local buckling of the compression face. Local and global buckling are irrecoverable deformations; local buckling is a change in cross sectional shape while global buckling is a change in member or structure orientation. Due to the high in-plane stiffness of an arch and the decking, which limits global out-of-plane deformations of the arches during concrete filling, global buckling is generally not a concern. However, due to the small thickness of the arch wall and the presence of a filling hole, local buckling failures are of concern for a full-scale hollow arch during concrete filling. Local buckling failures are not dependent on specimen length, provided the length is above crushing dominated failure and below Euler buckling failure, for pure axially loaded specimens. A short column in axial compression is considered to have – for the same material properties – the same compression face strength as a full sized arch. As short columns were easier to fabricate and test, short columns were tested in place of long arches or tubes for the majority of specimens.

Several models exist that give a predicted failure stress for local buckling of hollow sections in compression or bending (Timoshenko, 1935 Brazier, 1927 Donnell, 1934 and Kedward, 1978). All of these models are addressed by Kedward (1978). With the increased use of composites, buckling of composite cylinders has become a topic of interest for researchers. Hollow composites are not commonly used in highway infrastructure applications, but they are used in applications demanding a high strength to weight ratio, such as aerospace. An important subset currently being researched is anisotropic shells, shells with different fiber angles for different lamina. In these shells, buckling behavior is modified because the coupled flexure/torsion and potentially flexure/elongation and torsion/elongation can lead to early torsional buckling modes (Shen, 2008). If a cylinder made from a laminate schedule designed to maximize torsional buckling effect is compared in finite element modeling to a cylinder designed to minimize torsional buckling effect, the maximized model can have up to a 30% decrease capacity, despite having identical predicted capacity from classical buckling theory (Weaver, 2002).

Available analytical models exist for idealized homogeneous sections. The irregularity of the braid, native manufacturing defects (such as unintended curvature, diameter variation,

and non-circular cross section) and material anisotropy produce out of plane eccentricities that reduce the compressive buckling capacity of the thin wall composite tubes considered in this study. Therefore, laboratory tests have been performed on a variety of cross sectional geometries and potential arch materials to give baseline data on the local compressive buckling capacity that can be used to verify analytical and numerical models of wall buckling and assist in checking the capacity of an arch during concrete filling.

Specimen Fabrication and Material Properties

Fabricating Tubes

Laminate structure and the number of specimens tested for each type is listed in Table 11. Specimen identification begins with fiber composition; SC was a single carbon structural layer with a glass layer; BC was a single carbon structural layer, an outer bleeder abrasion resistance layer, and a glass layer; and DC was two layers of carbon with a glass layer. The second identifier was the nominal diameter of the specimen, 6.50in (165mm), 11.8in (300mm), or 14.8in (375mm); for example BC 300 refers to a 11.8in diameter bleeder carbon tube. For specimens with holes a third identifier was hole diameter, either 1.77in (45mm) or 3.00in (76mm); for example, BC 165-45 refers to a 6.50in diameter bleeder carbon tube with a 1.77in diameter hole. For a group of specimens tested with a known defect of inconsistent diameter, ID was added to the specimen label (SC 300-ID). Table 11 contains minimum buckling load, maximum buckling load, average buckling load, and COV of loads for each specimen type. Loads will be discussed in further detail in the failure strength section.

Table 11 Compressive Testing Matrix

	SC 165	DC 165	B.C 165	DC 165-45	DC 165-76	BC 165-45	BC 375	BC 375-76	SC 300	BC 300	SC 300-ID
Diameter (in)	6.50	6.50	6.50	6.50	6.50	6.50	14.8	14.8	11.8	11.8	11.8
Height (in)	15.0	15.0	15.0	15.0	15.0	15.0	29.9	29.9	18.1	18.1	18.1
Layers of Carbon	1	2	1	2	2	1	1	1	1	1	1
Carbon Layer Thickness (in)	.027	.027	.027	.027	.027	.027	.038	.038	.03	.03	.03
Carbon Braid Angle (deg)	22	22	22	22	22	22	18	18	22	22	22
Glass Thickness (in)	.035	.035	.035	.035	.035	.035	.039	.039	.046	.046	.046
Glass Braid Angle (deg)	81	81	81	81	81	81	76	76	81	81	81
Bleeder Thickness (in)	–	–	.03	–	–	.03	.035	.035	–	.03	–
Hole Diameter (in)	–	–	–	1.77	2.99	1.77	–	2.99	–	–	–
Hole to Diameter Ratio	–	–	–	0.273	0.461	0.273	–	0.203	–	–	–
Known Defect	No	No	No	Yes	Yes	Yes	No	Yes	No	No	Yes
Number of Specimen Tested	37	10	14	9	8	14	4	4	6	5	7
Number Included in Results	22	8	12	9	7	11	4	4	6	5	7
Average Ultimate Load (kip)	15.5	30.8	23.2	16.7	10.7	11.1	31.9	19.4	19.9	29.0	13.8
COV (%)	18.5	5.07	13.4	5.69	7.45	7.76	17.0	30.4	18.4	17.4	5.80
Lowest Ultimate Load (kip)	10.8	27.7	18.4	15.3	9.51	9.71	28.1	10.7	14.8	24.7	12.9
Highest Ultimate Load (kip)	21.4	33.0	27.0	17.9	11.8	12.1	39.8	23.2	25.2	35.3	15.0

All tubes used for testing were fabricated at AEWC. Arches used for bridges and fill testing as part of this research were fabricated by Kenway Corporation in Augusta, Maine. Arches are manufactured through the vacuum assisted resin transfer molding (VARTM) process, where vacuum suction forces the resin onto the fibers. This technique produces composites with a relatively high fiber volume fraction, little excess resin, and during VARTM there is little exposed resin reducing expelled gasses in the work area. Derakane vinyl ester 8084 resin was used in all specimens.

Arches are multilayer hybrid braided composites; each arch comprises two or more total layers and typically has a layer of braided glass fiber and at least one layer of braided carbon fiber. Braided fabrics keep all fibers aligned at the same angle (positive and negative) and allow layers to be pulled atop one another as a sock. The inner layer of a tube or arch is braided e-glass with fibers arranged close to the transverse or hoop direction (75 to 81 degrees relative to the longitudinal arch axis depending on diameter).

Outer layers of the tube, longitudinal strength layers, are comprised of fibers arranged closer to the longitudinal direction (15 to 30 degrees measured from the longitudinal arch axis for the tested specimens). Tubes have been constructed with one or two layers for this research, although additional layers have been used before, and outer layers for test specimens have been either carbon or glass fiber. All arches manufactured for bridges or built as direct replicas of bridge fiber architecture have been built with carbon fiber only for the longitudinal structural layers.

In some circumstances an additional 'bleeder' layer was added to the tubes. This layer is a thin (~0.028in) polyester random-orientation blanket material commonly used in composite manufacture to slow resin flow while keeping air passages open near vacuum ports. Originally added as an abrasion resistant layer, the bleeder material also helps local buckling capacity because it adds to the thickness of the cylinder. The bleeder has much lower stiffness than the longitudinal direction of the fibers, so it only minimally changes the longitudinal stiffness (elastic modulus times thickness) but it substantially changes the radial stiffness, or resistance to cross sectional shape change, as that term depends on thickness cubed; local buckling is a failure of the cross sectional integrity.

Material Assumptions

Throughout this thesis certain material properties, E_x-longitudinal elastic modulus, E_θ-radial elastic modulus, v_{xy}-Poisson's ratio, G_{xy}-shear modulus, were predicted for comparison with experimental results or to use in models when no experimental properties existed for that laminate. Classical Lamination Theory (CLT) with micromechanics was used to calculate all of these properties (for further information on

Classical Lamination Theory and micromechanics see Daniel and Ishai (2006)). Micromechanics provides a method of combining the properties of the vinyl ester resin with the fiber (carbon, glass, polyester bleeder) to get combined orthotropic properties, input properties are in Table 12. For transverse modulus and shear modulus the Halpin-Tsai approximations were used (Daniel and Ishai, 2006). Fiber volume fraction, V_f, is calculated from material properties explained later in this section.

Table 12 Micromechanics Constituents

Properties	**Matrix**	**E-Glass Fiber**	**Carbon Fiber**	**Bleeder Fabric**
V_f	-	0.56	0.56	0.33
***E* (Ksi)**	421	10400	34800	1450
***G* (Ksi)**	160	4350	4061	580
v	0.35	0.23	0.20	0.30

Classical Lamination Theory assumes a laminate comprises a stack of unidirectional plies. A braided layer is different from a unidirectional layer and the interaction of fiber and matrix are more complex in a braid. Several authors, including (Zeng et. al. 2004 Chen et. al. 1999 and Lei et. al. 1992), have addressed material properties of a braided composite with sophisticated finite element models. While these values can predict both strength and elastic properties, the purpose of material modeling in this thesis is to acquire missing elastic properties only, not predict composite capacity, because compression buckling failure results from a different mechanism than fiber failure.

When using CLT, braided fabrics do not achieve as high longitudinal elastic modulus as uniaxial plies (Carey, 2003), resulting in over prediction of stiffness. An approximation developed by Cox and Dadkhah (1995) based on a sinusoidal wave shape beam gives a longitudinal stiffness reduction factor. In Equation 2
, t_f is the fiber thickness, λ is the wavelength (measured at .709in for the carbon), E_1 is the fiber elastic modulus in the fiber direction, G_{12} is the in-plane shear modulus, v_{12} is the Poisson's ratio.

$$E_1(wavy) = E_1\left(1+2\left(\frac{t_f\pi}{\lambda}\right)^2\left(\frac{E_1}{G_{12}}-2(1-\nu_{12})\right)\right)^{-1} \qquad \text{Equation 2}$$

Later research (Edgren and Asp 2005) suggests that this model does not perfectly approximate the material stiffness. However, this model showed good agreement with results of coupon-level stiffness tests conducted at the University of Maine on carbon

fiber only (Bannon 2009) and on hybrid glass and carbon composites (Demkowicz 2011), predicting modulus to within 10%.

An important parameter in CLT is the fiber volume fraction, V_f, the percentage of a given volume of laminate that is fibers (for a vacuum infusion process it is assumed that the remaining volume is resin). Prior research on the arches has assumed a 50% fiber volume fraction (Bannon, 2009). There are techniques to directly measure fiber volume fraction such as acid digestion, and while it would be valuable to experimentally obtain this value, it is beyond the scope of present research. Also, this thesis deals entirely with arch or tube sections, not representative plate sections (comprised of the same laminates as an arch, but left as a flat plate), and in arch sections there is a large amount of surplus resin from flow media and infusion lines that contributes weight to a specimen but does not contribute to the layer thickness. The extra resin contributes little to the longitudinal or radial modulus, but it adds resin mass and changes the measured fiber volume fraction. As detailed later in this chapter, specimen thickness was measured carefully to avoid any resin ridges or other resin-rich portions of the tube. This presented another technique to find V_f. For a group of 6.50in tubes the length L_l and weight W_l of both the carbon fiber and the glass fiber was measured during fabrication; with a post infusion thickness t and diameter $2r$ the total volume V_l of a carbon fiber or glass fiber layer was calculated in Equation 3

.

$$V_l = 2r\pi L_l t_l \qquad \text{Equation 3}$$

With known densities ρ for both materials, it was possible to find the weight of a layer, if entirely fiber, and with that weight and the measured fiber weight calculate the fiber volume fraction in Equation 4

.

$$V_f = \frac{W_l}{V_l \rho} \qquad \text{Equation 4}$$

All of the input values for this analysis are in Table 13. This analysis shows that for mass of fiber to be conserved, for the measured thickness and diameter, fiber volume fraction for both the carbon and the glass should be 56%, which is 12% higher than the previous assumed value. Both layers independently indicated the same fiber volume fraction, lending confidence in its accuracy. Fiber volume fraction has been measured to be between 49% and 53% in plates made from woven E-glass reinforced sheets using the

same vinyl ester resin and the same vacuum infusion process (El-Chiti, 2005). The differences between the process used by El-Chiti and the arch fabrication process could account for the difference in fiber volume fraction. Another difference is thickness measurement technique; a caliper has a long jaw that spans the top of several fiber tow bundles. All measurements in tubes were taken with a fine ball micrometer to avoid resin ridges and flow media that create an artificial thickness. The ball micrometer was placed at thin points between fiber tows instead of measuring across the top, reducing the measured thickness and increasing V_f.

Table 13 Properties for Determining Fiber Volume Fraction

Material	**2*r* (in)**	**L_l (ft)**	**t_l (in)**	**W_l (lb)**	**ρ (lb/in^3)**	**V_f (%)**
Carbon	6.50	41.3	.027	10.0	.065	56.0
Glass	6.46	37.4	.035	16.5	.092	56.4

The areal weight of the fabric at the use angle is provided by the manufacturer; this value depends on the density and the thickness of the material. As seen in Table 14, the predicted weight was very close to the experimental for the carbon, but was different for the glass fiber braid. This value was used for calculating fiber volume fraction when individual material weights were not available (Demkowicz, 2011).

Table 14 Predicted and Measured Areal Weight

Areal Weight (PSF)	**Glass**	**Carbon**
Predicted	.391	.143
Measured	.261	.142

Another assumption used in all CLT models was that each braided layer counted as two opposing angle orthotropic plies that each occupies the full depth of the laminate and contributes 50% of the laminate properties. For a braided carbon fiber with 22-degree fiber angle and infused thickness of 0.027in, the total composite was treated as the arithmetic mean of a +22-degree 0.027in layer and a –22-degree 0.027in layer. Typically, a braided composite is treated as two opposing angle plies that each occupy half of a layer; for calculating the extensional compliance matrix both this method and the previous method produce the same result, but when a combined bending and extensional matrix is included the latter method introduces a false torsion-extension term. For calculating the longitudinal and radial moduli, the bending compliance matrix and the combined compliance matrix were ignored (Demkowitz, 2011).

Preparing Specimens

Large tubes were cut into short sections for axial compression testing using a horizontal band saw to produce planar perpendicular faces. Due to the slight curvature of the beams and the resin ridges on the surface, the cuts were planar but not necessarily parallel to each other or perpendicular to the longitudinal axis of the tube. The 6.50in diameter tubes were cut to 15.0in length while 11.8in and 14.76in tubes were cut to 18.1in and 29.9in lengths, respectively. Figure 39 shows all three different size specimens tested.

Figure 39 - Comparison of Different Size Specimens

Specimen height was measured at four evenly spaced points along the tube circumference. To determine that the points were evenly spaced the centerline circumference was measured using a cloth tape. The thickness of each specimen was measured at eight locations, four on each end of the tube. Thickness was measured using a 0.126in diameter ball micrometer. The thickness measurement was taken at the thinnest section within a diamond of the flow media as an attempt to capture the fiber thickness, staying away from resin ridges and the resin thickened areas near the flow media.

Table 15 contains the average thickness of each full 6.50in tube based on the eight measurements per specimen. Table 16 contains the same information pertaining to 14.4in diameter specimens. The coefficient of variability (COV) of specimen averages indicates the variability between the average thicknesses of each individual specimen. The COV of all measurements indicates the variability of all measurements taken on a single long tube.

Table 15 Thickness of 6.50in Diameter Tubes

Tube	Number of Measurements	Thickness (in)	COV (%) of Specimen Averages	COV (%) of All Measurements
SC 165, 1	128	.063	3.6	7.5
SC 165, 2	96	.062	3.5	11
SC 165, 3	40	.063	2.0	7.8
SC 165, 4	32	.059	1.2	6.2
BC 165	80	.092	4.1	6.6
DC 165	80	.089	1.3	4.9

Table 16 Thickness of 14.4in Diameter Tubes

Tube	Number of Measurements	Thickness (in)	COV (%) of Specimen Averages	COV (%) of all Measurements
BC 365	32	.122	4.3	7.2
BC 365-76	32	.122	5.6	7.5

The COV of specimen averages is lower for all tubes than the COV of all measurements indicating that the average thickness for all specimens was more consistent than the measurements taken within a single specimen. Longitudinal position in the tube and distance from infusion port has less effect on the thickness than cross section variability. Local thickness variability can be caused by thinner fibers or thinner resin coat and is a potential source of stress concentrations.

Instrumentation

Several setups for the instrumentation were used before deciding on the final version used for the remainder of the specimens. For 11.8in specimens, two +/-0.512in LVDTs (linear voltage differential transducers) were mounted to wooden holders attached to opposing faces of the cylinder with cyanoacrylate. Using two measurement devices produced unreliable data because it was difficult to see how the displacement varied around the entire perimeter of the specimen. For 6.50in and 14.76in diameters, four 1.0in potentiometers measured deflection. Figure 40 through Figure 42 show typical instrumented specimens.

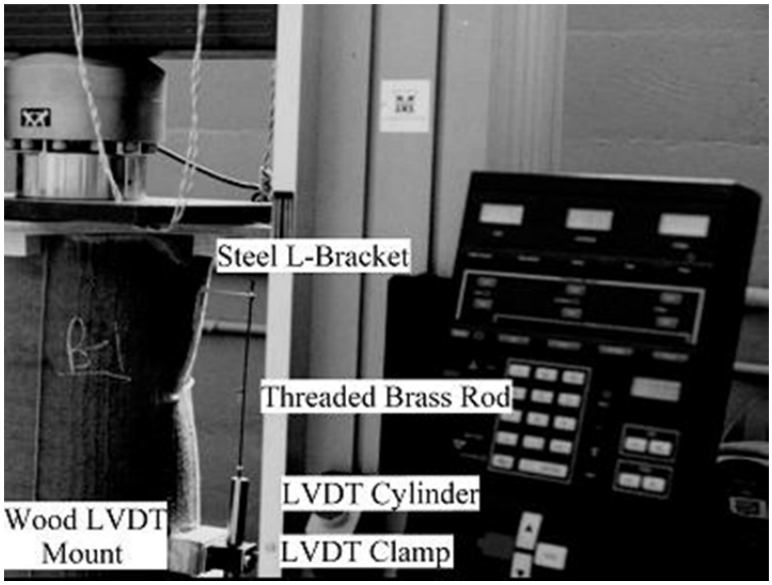

Figure 40 - Instrumentation of an 11.8in specimen

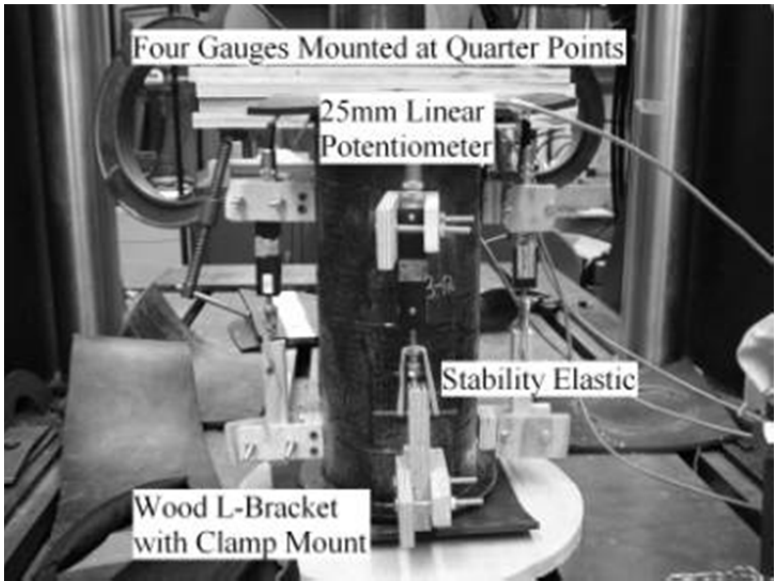

Figure 41 - Instrumentation of a 6.50in Specimen

Figure 42 - Instrumentation on 14.76in Specimen

To attach the potentiometers, L-brackets were constructed from wood with a height of 3.54in and a bottom leg of 0.984in plus the 0.295in to 0.492in thickness of the top leg. These two sections were connected with screws such that the long leg overhung the short leg by approximately 0.098 – allowing two gluing points on a round tube. Two L-brackets were attached 10.8in apart (outside edge to outside edge) for 6.50in tubes and 24.0in apart for 14.76in diameter tubes at quarter points on the perimeter of the cylinder. The bottom bracket held a wooden bearing rod and the top bracket held a 1.0 potentiometer. Both were clamped in place by a wooden plate and two 1/4x20 bolts. The potentiometers used required approximately a 0.9lbs force to either extend or retract. To overcome the initial force the gauge was held in contact to the wooden bearing surface with a rubber elastic. The elastic gave an initial compressive force that reduced a preload period where the gauge did not move despite the specimen moving. The elastics had an additional benefit of giving out of plane rigidity to the gauge. The centerline of the gauges were mounted approximately 1.57in from the side of the tube, meaning that for direct compression the gauges read the appropriate strain but when the specimen experienced bending they moved more than the cross section and were influenced by pinching and opening angles. As a result, the gauge with the largest deflection typically has a bent inward response and the gauge with the least compression (in some cases tension) has a bent outward response.

The failure time for a specimen was targeted at 2 minutes to 20 minutes to be within the static testing range. Tests were conducted in deflection control. The rate of actuator descent was set depending on the specimens and the boundary conditions. Different boundary conditions are compared in Walton (2011). For stiffer boundaries (steel, FRP) the load rate needed to be lower than for deformable boundaries (plywood, neoprene). For the 11.8in specimens, loads were recorded by a 45kip load cell on a 45kip capacity screw-drive actuator that moved at 0.1in/minute. For 6.50in and 14.76in specimens, loads were recorded with a 110kip load cell mounted on a 110kip capacity hydraulic actuator. Load rate for the 14.76in specimens was 0.2in/minute. 6.50in specimens had a variety of load rates depending on the boundary conditions. In general, plywood specimens were loaded at 0.10in/minute while resin capped specimens were loaded at 0.025in/minute, but this value was changed depending on other layers used in the boundary for load distribution such as neoprene or plywood.

Results, Analysis, and Observations

The primary goal of testing was to get ultimate strength values to be used as a comparison to model predictions, bend test results, and inputs for future modeling. A secondary goal of testing was to find a preferred test configuration to be used on future testing to minimize the uneven loading observed through differential deflection measurements, failure mode, and failure load. Terms used to describe the observed failure are defined, the variation in boundary conditions is explained, the failure strength results is presented, the instrument deflection results are presented, the elastic modulus calculation is explained and the effect of certain defects on ultimate strength – holes and diameter fluctuation glass fibers – are discussed.

Terminology

The location of the failure and the speed of failure were chosen to characterize the failure mode of the FRP cylinders. Both are indications of the uniformity of boundary conditions (loading). The three locations of failure were:

Bearing failure: Specimen failed at the boundary-characterized by delamination of the glass and carbon layers at the edge of the specimen. The specimen did not buckle. See Figure 43.

Figure 43 - Tube After Bearing Failure

Bearing-buckling failure: Specimen failed either below the bottom gauge or above the top gauge. This failure may have incorporated a certain amount of bearing damage after initial failure, but shows clear evidence of buckling and initial failure is approximately 0.591in to 1.97in from the specimen edge. See Figure 44.

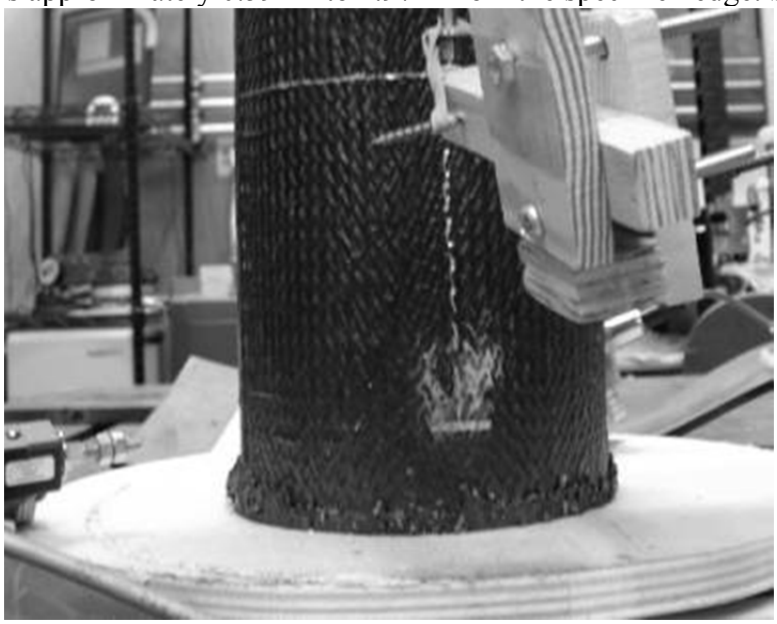

Figure 44 - Bearing-Buckling Failure

Buckling failure: Specimen failed far enough away from a boundary that no evidence of the failure existed at the boundary or at the plate level. See Figure 45.

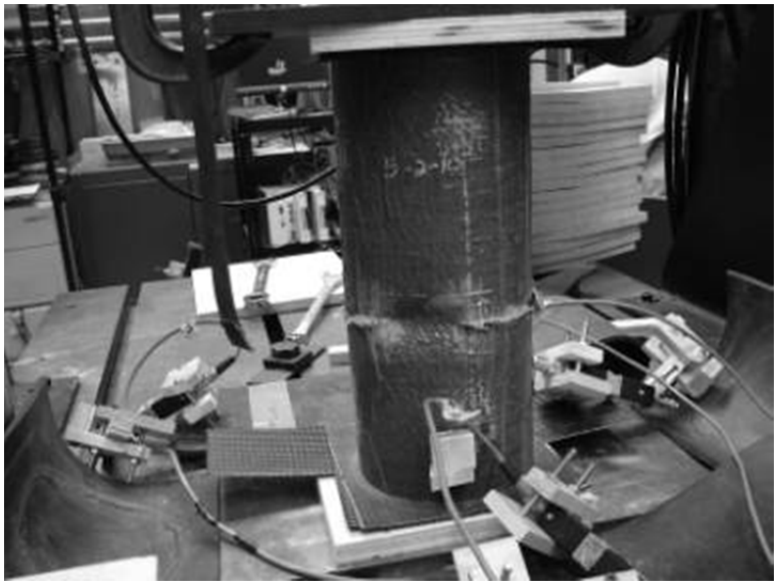

Figure 45 - Buckling Failure

The three failure rate definitions are:

Progressive slow: Specimen buckled in a single location, continued to carry additional load, and more than five seconds passed before the specimen buckled further. This failure rate showed uneven loading where other areas of the specimen were able to hold the capacity of the failed section for a prolonged time. In many cases the ultimate load was reached after the first buckle. See Figure 46 for a typical load-deflection plot.

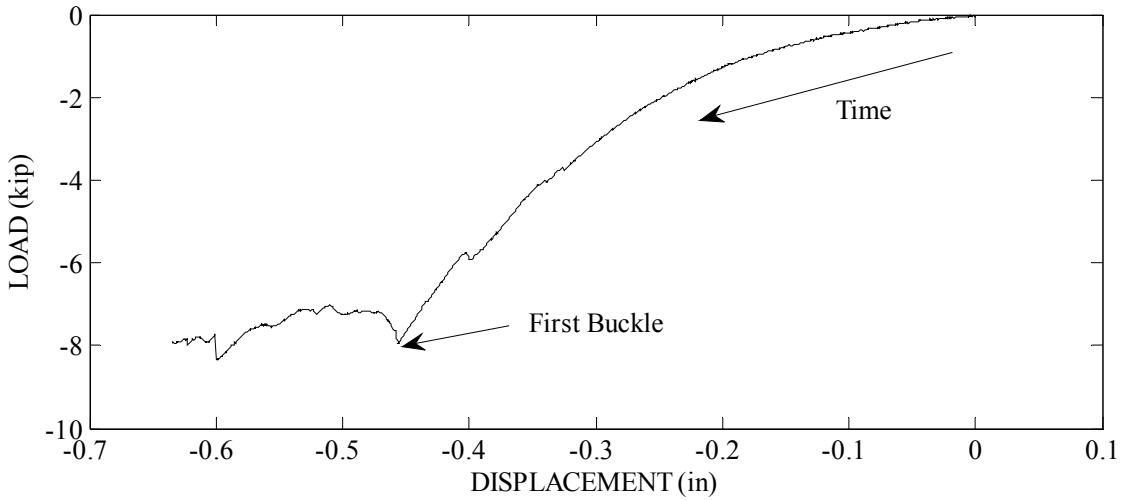

Figure 46 - Load-Displacement for Progressive-Slow Specimen SC 165, 1-13

Progressive rapid: Specimen buckled in a single location and within the next five seconds buckled around perimeter greatly reducing carrying capacity. This failure rate generally coincided with relatively uniform loading as measured by the LVDTs. It was possible that in a load controlled or gravity controlled test, specimens that failed at a progressive rapid rate would fail suddenly because they rarely were able to hold a higher load than initial buckling load. See Figure 47 for a typical load-deflection plot.

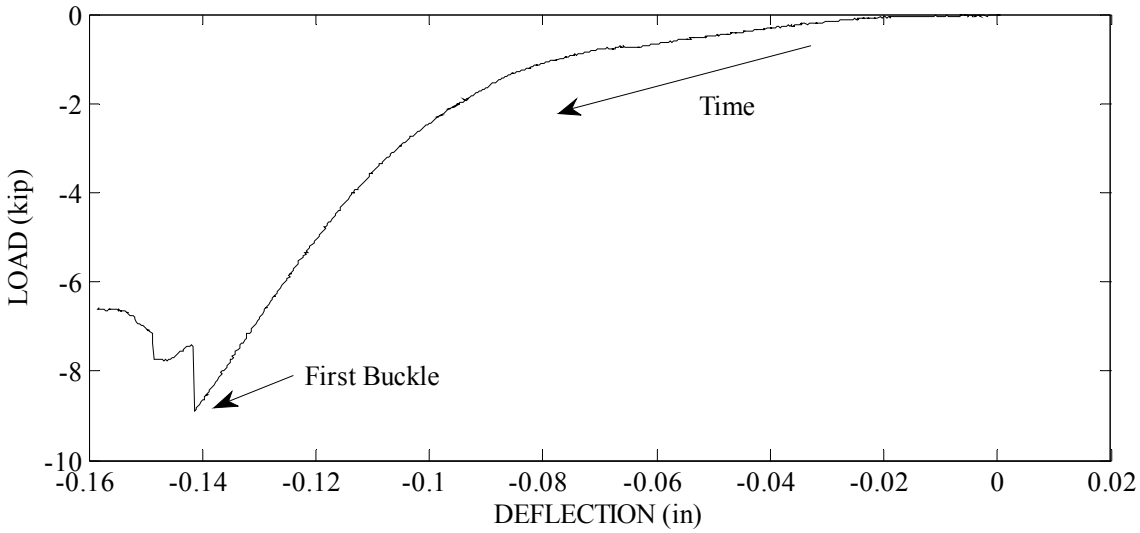

Figure 47 - Load-Displacement for Progressive-Rapid Specimen SC 165, 1-2

Sudden: Specimen lost carrying capacity and buckled in multiple locations within an indistinguishable time. This failure rate showed very close to uniform loading. See Figure 48 for a typical load-deflection plot.

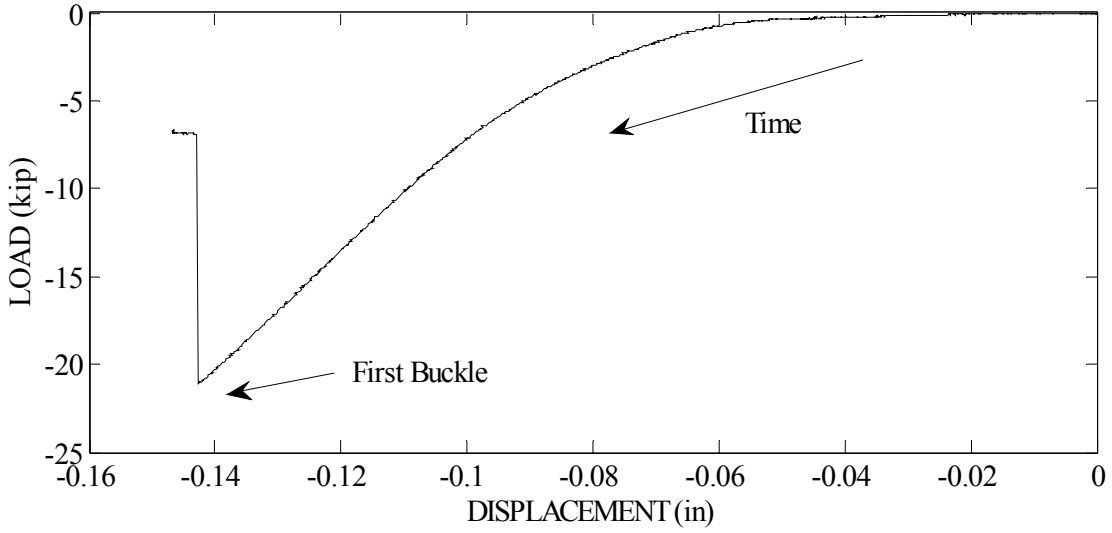

Figure 48 - Load-Displacement for Sudden Buckling Specimen SC 165, 1-6

Boundaries

Boundary conditions were modified and improved during the test series to produce the most reliable and repeatable test. Tests were evaluated on ease of implementation, percentage of sudden failures (a measure of even loading), and uniformity of strain. Two end restraint conditions were tested: fixed-fixed (with two perpendicular plates) or fixed-pin with a top plate that was fixed and a bottom plate mounted on a swiveling ball that was free to rotate as seen in Figure 49. Testing indicated that the specimens with the ball failed early as a result of having a large bending component. The bending component was due to out of plane loading caused by locally softer response in different sides of the specimen or bending and movement of the specimen in the direction normal to the shell.

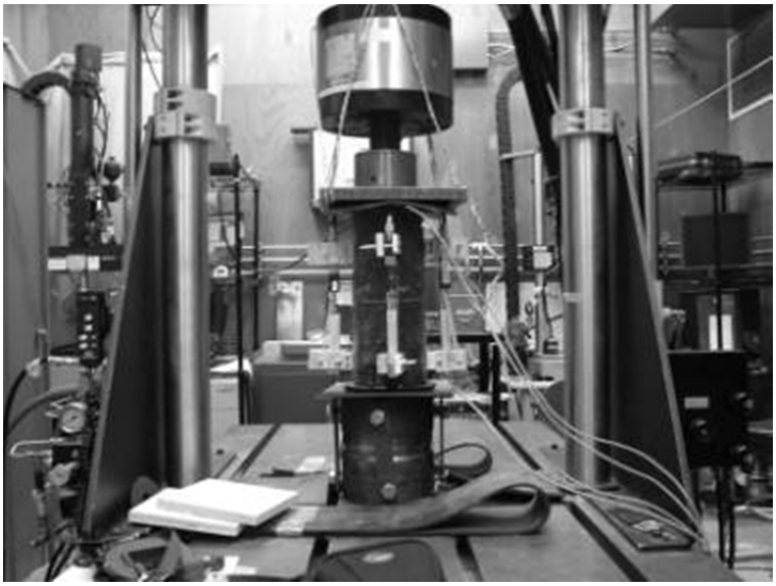

Figure 49 - Specimen Tested with Pivoting Bottom Surface

Four bearing surfaces were used: steel, resin, plywood, and FRP; as well as three materials for under layers between the cross head or table and the specimen: steel, wood, and neoprene. The best boundary condition was obtained with plywood, which crushed before tube rupture and allowed loads to distribute. Performance improved when an infused carbon fiber sheet was placed between the specimen and the plywood delaying the crushing failure and activating a larger crush area. This prevented excessive crushing in high buckling capacity specimens. Details on the different boundary conditions used are in Walton (2011).

Failure Strength

In compression it was possible for a specimen to fail in a localized segment while other segments continued to hold the same or higher compressive load. Bending failures cannot reload; the change in section modulus from cross sectional buckling makes any bending failure irrecoverable. For compression, the failure strength was categorized as the load at which the first buckling or bearing failure occurred. Table 17 contains the average failure load and the coefficient of variation for each type of specimen tested as well as the average of all single layer specimens. Also listed is the number of specimens tested as well as the number of specimens included in the average. For the results of every specimen tested as well as the load deflection plot and instrument deflection plot see Walton (2011).

Specimens were rejected from Table 17 for three reasons: a ball support was used, the resin cap cracked prior to failure, or the specimen failed in bearing. Testing with a pivoting load or ball support caused highly variable stresses that were read by the gauges as in-plane bending. This was visible in a graph such as Figure 50 below that shows a gauge reading tension in an axial compression test. The progressive slow failure rate for all specimens with this support type is further evidence that the specimens were not experiencing a symmetric load. The ball introduced out of plane bending stresses from a non-axial load that were small but significant due to the relative weakness of the specimen in that loading direction. Use of this fixture also resulted in a significant reduction in failure load.

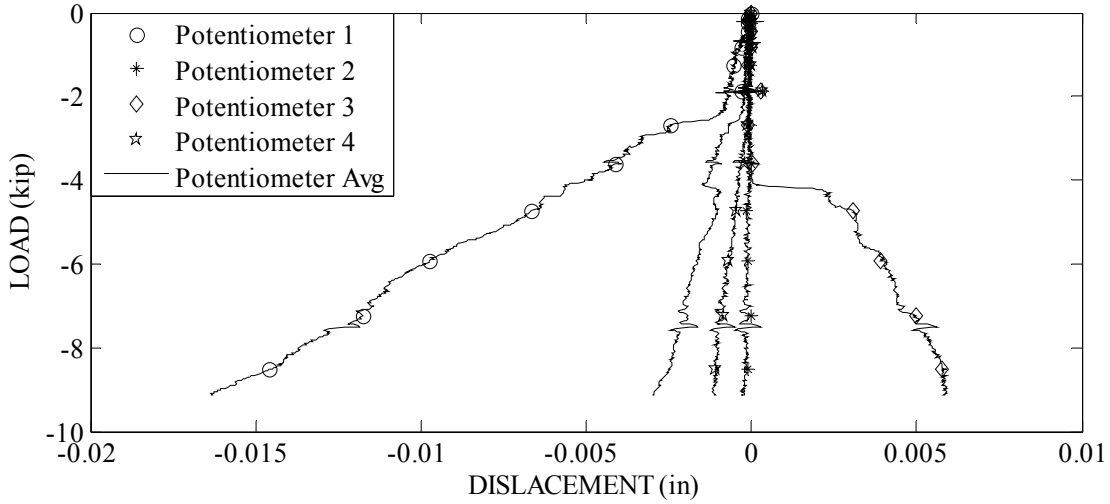

Figure 50 - Specimen SC 165, 1-8 Instrument Displacement Versus Load

Any specimen tested with a resin cap where the cap cracked prior to failure was likely to have sustained end damage on the interface with the resin. This made some specimens fail in bearing instead of buckling. Also, those specimens that did not fail in bearing were likely to fail at a lower load from having an uneven end condition from partially broken resin. Uneven loading of broken resin caps introduced many progressive-slow failures that were a symptom of highly irregular loading.

Specimens were also removed if they failed in bearing, a failure mode with different characteristics that was dependent on local discontinuities and hardness. Bearing failure was a delamination or crushing of the specimen edge and specimens tested with direct contact to steel plates failed in this mode because the material did not accommodate the tube. Other boundaries yielded at the specimen edge. Once the specimen started to crush it would delaminate to reduce load rather than buckle. Issues such as lack of smoothness

of the specimen edge caused local stress concentrations on the edge of the cylinder that resulted in bearing failure. Bearing failure could be a sudden failure and in some circumstances occurred at a load similar to the buckling load, however it was not the failure mode that was tested for and it therefore was not included in the calculation of the average and COV of the local buckling strength.

The ultimate load did include specimens that failed in either buckling or combined bearing/buckling as they were both local buckling failures and there was not a significant difference in the relative strength of the two failure modes.

Table 17 Failure Strength of 6.50in specimens

6.50in Specimens	Load (Kip)	COV	Number Tested	Number Included
SC 165, Tube 1	16.1	13.2	16	7
SC 165, Tube 2	13.5	19.0	12	8
SC 165, Tube 3	18.7	10.8	5	4
SC 165, Tube 4	14.7	14.1	4	3
SC 165, All Tubes	15.5	18.5	37	22
BC 165	23.2	13.4	14	12
DC 165	30.8	5.07	10	8

The specimens built with double carbon fiber have slightly higher than double the strength of single carbon layer specimens. This was not because the carbon was the only component contributing strength. An added polyester bleeder layer provided a ~50% increase in strength over single carbon by including a layer that had much less stiffness than either the carbon or the off axis e-glass. The results for the bleeder specimens show that increasing wall thickness without making much change to the relative modulus (elastic modulus independent of thickness) increased strength. The bleeder layer and the outer carbon layer both provide an increase in shape stability that increased the buckling load and they bridged gaps or imperfections in the inner layer of carbon, giving better coverage than a single layer of carbon. The second carbon layer provides an additional increase in strength by providing an increase in modulus as seen in later sections. The double carbon specimens had a low COV and a consistent failure mode; seven of eight failed in bearing-buckling.

Global buckling for a column is Euler buckling (Gere, 2004). For a column with pin-pin end conditions, the critical buckling load P_{cr}, Equation 5

, requires the longitudinal elastic modulus E_x, the moment of inertia I and the length of the column L.

$$P_{cr} = \frac{\pi^2 E_x I}{L^2}$$ Equation 5

For the single-carbon, short-column compression tests, the resulting critical buckling load was 1170kip; two orders of magnitude above the actual buckling load. Because of the large difference in actual buckling and global buckling, it is unlikely that failure occurred in the combined local-global region indicating that the specimen failed in pure local buckling, as intended.

Instrument Deflection

For 11.8in diameter specimens two LVDTs were used to measure deflection. From these two gauges it was impossible to determine the shape of the load distribution but it was thought to be planar due to the two planar faces of the cylinder. To address this uncertainty, testing on the other two diameter specimens was performed with four deflection gauges to observe stress distribution through variation in deflection. If stresses were planar, the most deflected gauge would be opposed by the least deflected gauge and the average deflection of opposing gauges 1 and 3 would be close to the average of 2 and 4. Of the 64 specimens tested only 23 had the highest deflection gauge opposing the lowest deflection gauge at 90% of peak load. Only 18 of the 43 specimens with good load-deflection data had opposing slopes within 25% of each other. Based on this it can be concluded that the majority of specimens did not load with a planar load or did not respond with even axial stiffness around the entire perimeter.

Calculating Elastic Modulus

The FRP shell was assumed linear elastic, meaning that the strain and the stress were related by a constant elastic modulus. FRP is typically assumed to be a linear elastic material because the fibers are linear elastic. The polymer matrix is not linear elastic, but the fibers have a much higher contribution of stiffness to the laminate. The fiber response is more characteristic of the total response. Elastic modulus is presented in terms of stress times length (ksi-in) or relative modulus, ignoring the thickness of the specimens. This is because thickness was highly variable within the same specimen. As mentioned, in the Instrument Deflection section, the measured deflection of the individual gauges was not linear because the loads were irregular and there was a bending response. The bending response tended to cause one gauge to pinch inward (compress) while its opposite gauge extended outward (tense) making the average of two gauges

include only the axial deflections, not the bending deflections. Averaging the four evenly spaced gauges gave the best attainable deflection.

Several of the first specimens tested were instrumented with a faulty gauge configuration and either the gauge broke away from the specimen prior to failure or lacked the rigidity to remain vertical, so only 43 of the 57 6.50in specimens tested were considered for calculating elastic modulus. The gauges exhibited a relatively high load to deformation compared to other instrumentation, (about 0.9lbs to get the gauge to move,) so a certain amount of deflection needed to occur before any gauges moved. Because the initial load was biased, based on the slight height irregularities of many specimens, the early loading period with a false stiff response lasted until 30% or less of ultimate load. Prior to failure, out of plane motions became large as specimens started to buckle; to avoid this effect no data beyond 90% of ultimate load was used for calculating elastic modulus. Elastic modulus was calculated as the slope of the average deflection-load plot from 30% to 90% of ultimate load multiplied by the gauge length (a constant for all specimens of the same type) and divided by the cross sectional perimeter. Figure 51 is a typical plot of load vs. instrument deflection, for specimen BC 165, 1-9, one of the 6.50in diameter bleeder-carbon tubes with a gauge length of 9.45in. Constant load bars were added at 30% and 90% of maximum load, the duration used for calculating elastic modulus. This plot shows the initially stiff response and illustrates the method of computing the elastic modulus.

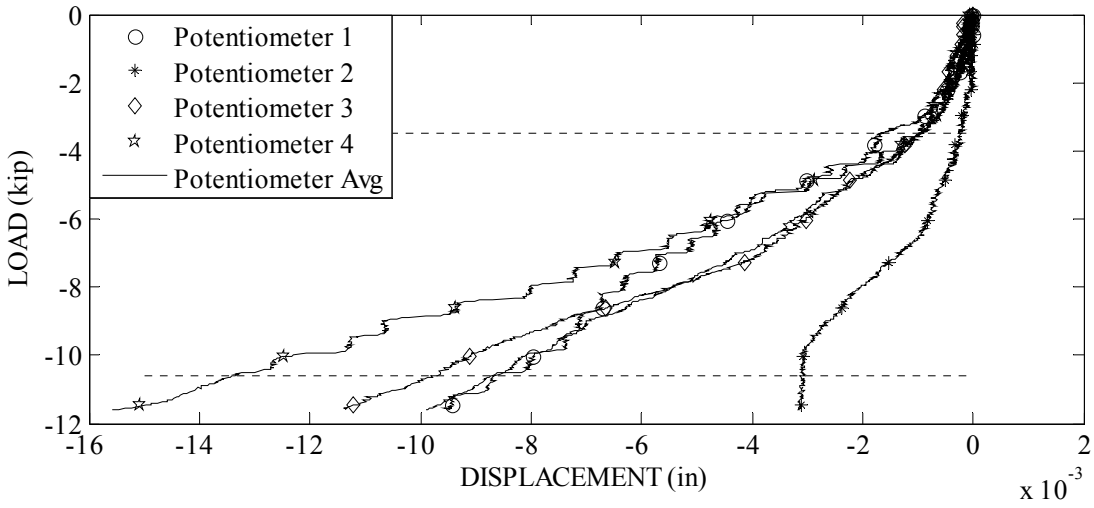

Figure 51 - Load Versus Instrument Deflection, Specimen BC 165, 1-9

R^2, a common measurement of linearity, was indicative of a linear response (.93 to .99), for the slope of the average deflection versus load plots. The number of specimens

accepted, averaged R^2, elastic modulus, coefficient of variation (COV) of elastic modulus, predicted modulus, and percent difference between predicted and experimental for the 6.50in tubes, are given in Table 18.

Table 18 Longitudinal Elastic Modulus Properties

Layer Type	**SC 165**	**BC 165**	**DC 165**
Number	25 of 37	8 of 10	10 of 10
E_x (Kip/in)	490	454	851
COV %	26.5	15.5	14.2
R^2	0.981	0.993	0.995
Predicted E_x	62.3	65.6	112
% Difference	27.4	17.5	24.9

The relative moduli presented in Table 18 show that the single layer carbon and the single layer carbon with bleeder specimens had close experimental moduli, and they also had close predicted moduli. The bleeder layer has a low relative stiffness compared to carbon fiber or glass fiber and a low fiber volume fraction, estimated at 33% instead of 56% for the other laminae, that gives very little influence to the relative modulus. The increased thickness was offset by decreased stiffness per thickness. The second carbon layer added a significant amount of stiffness to the laminate, about a 40% increase in the relative modulus. The COVs from all three specimen types were high, which suggests that there was a high degree of variability in the stiffness of the specimens or that the gauges did not properly read the deflection. Strain was measured with long gauges that assumed the specimen did not bend during loading. While global bending, the entire cross section shifting out of plane, could be removed from the data, local bending due to material imperfections would not be removed by averaging values. It was not surprising that the single layer specimens, despite a higher number of samples, had a higher COV because they were more prone to local errors as most of their stiffness came from the single carbon layer and any imperfection in that layer would have little support from other portions of the tube. This had a dramatic effect on the buckling strength, but it also loaded the tubes locally and made them more susceptible to producing errors in the gauges.

Predicted modulus was based on Classical Lamination Theory and micromechanics assumptions as detailed in material assumptions. As seen in Table 18, the predictions were not close to the experimental stiffness values. The difference is more likely a reflection on poor measurement technique than a faulty model. A similar version of this model has been compared with just carbon fiber, not a glass/carbon hybrid, and produced errors below 10%, (Bannon, 2009). During testing, the high internal resistance of the displacement gauge made it possible for the gauge to rotate outward instead of compressing, which would have under-measured strain resulting in a stiffness that was too high. In some cases, the measured stiffness was near or below the predicted stiffness,

but those values were offset by other measured stiffnesses that were more than double the predicted stiffness. The lowest COV of any material during this test was at over 14%, much higher than typical for a composite. This further suggests faulty test practice rather than actual material uncertainty.

Comparison to Models

Several models exist that were compared to the experimental data and used as predictions on the capacity prior to testing. The models poorly predicted the capacity of the laminate because they were formulated for isotropic or orthotropic materials – not anisotropic. Also, the material Poisson's ratio as predicted by micromechanics was 0.3 to 0.53 depending on fiber orientation, but the measured Poisson ratio from mechanical tension testing of a two layer carbon fiber composite, identical to the carbon fiber used in the 11.8in specimens, was 1.26 (Bannon, 2009) and a combined section modulus gives a Poisson ratio of 0.8 to 0.9. All of the models that contain Poisson's ratio broke down if it exceeded 0.5, and those that do not explicitly include Poisson's ratio directly still assume a typical material property of under 0.5. For the purpose of prediction, the micromechanics Poisson's ratio was used instead of the experimental value to give an equation that will produce a real result and does not violate the mechanical principles governing the equation.

Six models are compared with experimental results; all six models were addressed by Kedward (1978), and these models can be divided into two groups of three. The set of models based on compression is from research by Donnell (1934). The other set of models is based on bending research by Brazier (1927). The work by Donnell and Brazier is based on an isotropic material; both models have been modified for both an orthotropic material and an anisotropic layered composite.

Timoshenko (1961) developed this minimum stress value, Equation 6
, for Donnell's defect-based model; Kedward suggested multiplying by 0.606. E is elastic modulus in this isotropic material equation.

$$\sigma_T = \frac{Et}{r\sqrt{3(1-\nu^2)}} \qquad \text{Equation 6}$$

For an anisotropic multilayer composite the previous equation is modified to include the bending stiffness matrix for a composite. This gives increased strength to a material that is stiffer on the outside than the inside; unfortunately this equation was developed for a balanced laminate and tends to be problematic for an unbalanced laminate. In Equation 7 D_{11} is a bending compliance term and Φ, Equation 8

, is a shear stiffness reduction factor suggested by Kedward; it must be less than one or it is treated as one. Equation 7
is identical to Tatting's (1998) interpretation of the Donnell equation with the additional of a knockdown factor.

$$\sigma_L = \Phi \frac{\sqrt{E_\theta D_{11} t}}{rt} \qquad \text{Equation 7}$$

$$\Phi = \sqrt{\frac{2G_{x\theta}\left(1 - \nu_{x\theta}\nu_{\theta x}\right)}{\sqrt{E_x E_\theta}}} \le 1.0 \qquad \text{Equation 8}$$

Kedward's orthotropic equation for compression buckling capacity, Equation 9
, is very similar to the anisotropic laminate equation; it replaces the composite stiffness term with its orthotropic value. This equation also clarifies the connection between the orthotropic and anisotropic equations.

$$\sigma_L = \Phi \frac{\sqrt{E_x E_\theta} t}{r\sqrt{3(1-\nu^2)}} \qquad \text{Equation 9}$$

Brazier (1927) used energy methods for a deformable cross section to develop a buckling stress for an isotropic tube. Developed for bending, Equation 10
incorporates internal stress from radius loss.

$$\sigma_B = \frac{2\sqrt{2}}{9} \frac{Et}{\sqrt{(1-\nu^2)}r} \qquad \text{Equation 10}$$

Equation 11
is a modification of Brazier's stress for an anisotropic laminate developed by Kedward. Kedward also provided an orthotropic equivalent in Equation 12
by replacing the bending compliance term with its orthotropic equivalent.

$$\sigma_K = \frac{2\sqrt{2}}{9} \frac{\sqrt{D_{11} E_\theta} t}{tr} \qquad \text{Equation 11}$$

$$\sigma_K = \frac{2\sqrt{2}}{9} \frac{\sqrt{E_x E_\theta} t}{\sqrt{(1-\nu_{x\theta}\nu_{\theta x})}r} \qquad \text{Equation 12}$$

Using the predicted values for Poisson's ratio, *E*, as well as all of the measured average terms, the experimental local buckling stress was compared to the six local buckling failure predictions.

Table 19 Predicted Compressive Load and Experimental Load in kips

	Bending			**Compression**			
	Isotropic Equation 10	**Orthotropic** Equation 11	**Anisotropic** Equation 12	**Isotropic** Equation 6	**Orthotropic** Equation 7	**Anisotropic** Equation 9	**Experiment**
SC	46.3	36.0	38.0	51.5	52.8	51.0	14.7
BC	72.2	57.3	31.7	80.5	85.0	43.2	23.2
DC	128	76.9	71.7	142	119	104	30.8

No compression prediction comes close to the experimental buckling stress; most over predict capacity by at least 200%. The bending-based predictions do not do much better; with one exception they over predict average compression capacity by at least 100%. Specimens tested had an unbalanced anisotropic laminate – a coupled action reduction was not accounted for in these predictions. Coupled action means that when subjected to axial compression the laminate will want to bend in its principal material directions. Unlike a thin plate, a cylinder has increased rigidity against warping curvatures and it is unlikely the cylinder shape will alter much under the coupling effects, but these expected curvatures will still induce additional stress on the composite not accounted for in any of these models. The importance of coupling can be seen in the predictions for the single carbon and the bleeder carbon buckling stress. The bleeder carbon tube was stronger in experimental tests, it is the single carbon tube with an additional layer to stiffen against out of plane bending, but the model predicts a lower buckling load because the carbon is in the center of two soft materials and therefore cannot contribute much bending resistance, lowering the *D* term versus the single carbon prediction.

Effect of Known Material Errors on Strength

Materials with the known defects of excessive diameter change and drilled holes have been tested to determine the acceptability of these errors on actual bridges.

Diameter Inconsistency

Diameter inconsistency is a problem that to a certain extent every arch suffers from. During the manufacture process the diameter of the inflated e-glass braid was measured at use angle, and while it is typically close to the nominal values, there are always fluctuations at the several hundredths of an inch level. Change in diameter could have a severe impact on the strength performance of an arch. Inconsistent diameter implies a region where the material has a tapered shape and loads traveling though the wall thickness are partially directed away from the vertical axis of the arch. The stiffness of the arch through the wall thickness direction was several orders of magnitude lower than the longitudinal or radial stiffness. Even small loads directed through the thickness result in shape changes leading to buckling instability. Buckling was more of an irrecoverable shape change than fiber failure, and shape change was exacerbated by initial diameter irregularities.

Specimen Description

In all arches, the inner E-glass braid layer holds the diameter of the arch constant during resin infusion. The imperfections in this layer varied the diameter of the circular cross section or made the section less circular. The fabric reinforcement typically has slight changes in diameter, but they are acceptably small and gradual, less than 1% total change over the specimen (not readily visible). Diameter fluctuations are measured as change in the perimeter of the inflated E-glass braid layer measured with a pi tape or a cloth tape at 6.0in intervals. Measurements were made at the E-glass braid placement stage of fabrication to avoid resin ridges that are formed during infusion. The manufactured tube had no sudden bulge or hourglass deformities that developed in less than 6.0in; the measuring method did not entirely miss any diameter defects, although local maximum and minimum diameters of the varying diameter wave were not necessarily measured. An eccentricity term was created to quantify inconsistent perimeter, this term is the percent change in perimeter in a 6.0in interval Equation 13

.

$$\text{eccentricty} = \frac{\Delta D}{6.0in} \qquad \text{Equation 13}$$

A gradual taper over the full 24.0in height of a specimen would have a lower eccentricity than a specimen with no taper over 18.0in of the height and a steeper taper over the final 6.0in.

AEWC Advanced Structures & Composites Center
5793 AEWC Bldg
University of Maine
Orono, ME 04469-5793

Telephone: 207-581-2123
FAX: 207-581-2074
contactaewc@umit.maine.edu
www.aewc.umaine.edu

Table 20**Error! Reference source not found.** contains the measured diameter and the calculated eccentricity for all of the control and inconsistent diameter specimens (ID). An eccentricity of two-thirds of a percent (0.67%) was a threshold for diameter inconsistency, and a specimen from each group was very close to this threshold. Visual observation was very important in this process; all of the inconsistent diameter tubes were taken from a length of tube that looked wavy; specimen SC 300-6 was also taken from this section but measured with such low eccentricity it was included with the control specimens.

Table 20 Diameter Measurement for Inconsistent Diameter Specimens

Sample	Top D (in)	Mid 1 D (in)	Mid 2 D (in)	Bottom D (in)	Eccentricity %
SC 300-1	11.7	11.7	11.6	11.7	0.439
SC 300-2	11.7	11.7	11.7	11.7	0.169
SC 300-3	11.7	11.7	11.7	11.7	0.169
SC 300-4	11.7	11.6	11.6	11.6	0.509
SC 300-5	11.6	11.7	11.8	11.7	0.644
SC 300-6	11.6	11.6	11.6	11.6	0.272
SC 300-ID-1	11.6	11.6	11.6	11.8	1.22
SC 300-ID-2	11.8	11.8	11.6	11.6	1.81
SC 300-ID-3	11.6	11.6	11.6	11.7	0.883
SC 300-ID-4	11.7	11.8	11.5	11.8	2.08
SC 300-ID-5	11.8	11.8	11.7	11.6	0.969
SC 300-ID-6	11.6	11.6	11.7	11.8	0.678
SC 300-ID-7	11.8	11.8	11.8	12.0	1.70

A piece of e-glass that had been rejected from manufacturing due to visible diameter flux was used to manufacture 11.8in specimens. The capacity of the visibly bad specimens was compared with those from the same tube that had little diameter variation and some tubes with bleeder material. Sample sizes were small as all three groups of tubes were taken from the same long specimen.

Results

There was a large difference between the normal, inconsistent diameter, and bleeder-covered specimens, in Table 21.

Table 21 11.8in Specimen Ultimate Strength

Specimen	SC 300	SC 300-ID	BC 300
Ultimate Load (Kip)	19.9	13.8	29.0
COV	18.5	5.80	17.4
Sudden Buckles	3 of 6	0 of 7	2 of 5

The additional bleeder layer caused a considerably higher capacity, approximately 50%, while inconsistent diameter fabric showed 30% lower strength. Having multiple failure rates caused the high COVs of the normal and bleeder specimens. Normal and bleeder specimens each had some specimens fail with higher than average loads in a sudden

buckling mode. The other specimens, including all of the inconsistent diameter specimens, failed in progressive slow failure modes. Boundary conditions are a potential source of this difference as the same plywood end caps were used for every specimen and they became heavily grooved by the end of testing. However, the high COV and the difference between sudden and progressive buckling were also true for the 6.50in specimens that were tested with new boundaries on every specimen. Ineffective deflection measurements were taken from these specimens so any attempt at calculating elastic modulus was inaccurate and it was impossible to judge the evenness of the stress distribution around the entire perimeter from only two points.

Concrete Filling Holes

Arches are field filled with concrete and the concrete must have a means of entering the arch. Two methods, end filling and crown filling, have been employed and are discussed in Walton (2011). Crown filled arches require a 2.52in -2.95in hole to be drilled in the arch for the concrete pipe to gain access. This hole at the crown of the arch was in a high bending stress region – in an area that was in the compression face of the arch.

Holes have a detrimental effect on composite materials and researchers have tried to quantify the effect of holes in various composite materials. Saha (2004) tested pultruded e-glass fiber with polyester matrix plates with a series of holes ranging from 7% to 69% of the width. Results showed a reduction in capacity of 66%-70% from the smallest hole to the largest hole depending on specimen thickness, with thinner specimens achieving higher compressive stress capacities. Similar reductions have been found in carbon fiber composites (Rhodes and Mikulas, 1987).

Soutis and Fleck (1990) tested graphitic carbon fiber composites in compression with mixed fiber angles (+/-45 degree and 0 degree) and holes. Specimens were 1.97in wide with 0.197in diameter holes. The average failure stress of specimens with holes was 45% lower than specimens without holes. During compression failure, specimens failed initially at the 0 degree plies; high relative stiffness attracted much of the load. Similar results have been found by other researchers (Arslan, 2009). Failure in tests by Arslan were consistent: all specimens failed within 5% of the same load, failed near the hole, and failed at a lower load than all specimens without holes. The author concluded that the consistent failure mode and load were indicative of a failure controlled by the hole.

Holes in 14.4in Specimens

The effect of a hole on capacity was explored in two series of testing. First, eight total 14.4in diameter specimens were tested in axial compression. These specimens had four control specimens without holes and four specimens with 2.95in -4.15in holes drilled at the middle of their 29.9in height. Specimens were cut apart with a horizontal band saw

that was too small to cut the specimens in a single pass causing the specimens to have a large variation in height and a visibly uneven edge. Instrumentation was mounted as described for the 6.50in specimens only the gauge length was increased to 22.4in. Load rate for this test was 0.2in/minute. Figure 52 shows a comparison of tests performed on 14.76in diameter specimens with and without a hole to show the scale of the hole relative to the specimen.

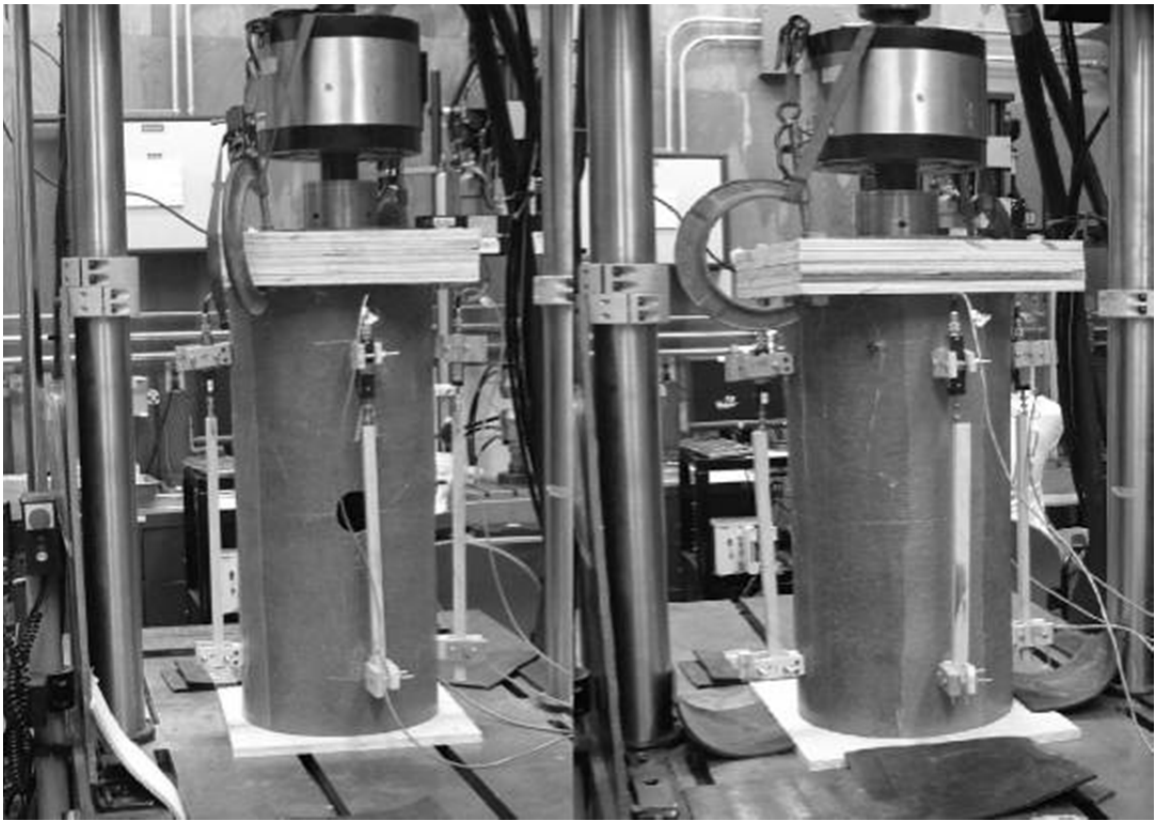

Figure 52 - Compression Test, 14.76in Diameter, With Hole and Without Hole

Specimens with holes had a lower load capacity than specimens without holes, but the difference between the specimens was clouded by the edge imperfections from the cutting process. In the case of some tests there was a load of 9kip on the specimen while there was still a visible gap between the specimen and the plate – half of the ultimate load was applied before the second side saw any load.
Table 22 contains a comparison between the loads of the two specimen types.

Table 22 Ultimate Load on 14.76in Tubes

Type	Control	Hole
Failure Load (Kip)	31.9	19.4
COV %	17	30.4

The holes created a loss in load capacity of 40% compared to specimens without holes. This value may be artificially low due to the irregular boundary conditions. The uneven end cuts would have a more detrimental effect for the control specimens because they did not have a controlling defect. Buckling failures were precipitated by defects, and all control specimens had a preexisting boundary defect while all specimens with holes had the hole as a primary defect. All four of the specimens with holes buckled at the hole, meaning that the hole was a larger defect than the unevenness at the end points. For some of the specimens with holes it was possible that the uneven boundaries improved the capacity because stress concentrations were directed away from the known weak spot until the tube was sufficiently loaded to damage the plywood end caps and begin loading the holed section, while an even load distribution would have already compromised the hole. Control specimens could only be hurt by stress concentrations at any location because their nominally equal strength around the circumference gave no preferential failure location.

Holes in 6.50in Specimens

Holes were also drilled in a series of 6.50in diameter, 15.0in length, double carbon and bleeder carbon specimens. Identical material and specimen dimensions to prior 6.50in diameter cylinders, these cylinders had holes drilled at mid height. All bleeder carbon specimens had a 1.75in diameter circular hole drilled at the mid height. Nine of the double carbon specimens had the same 1.75in hole and eight specimens had a larger 2.95in -3.15in hole. All holes were cut with a hole saw. The smaller hole was picked as the closest hole saw size equivalent (ratio of diameters) to a 3.0in hole in a 11.8in specimen, a typical case for filling. The larger hole size for double carbon specimens did not reflect a real world application; it served as a hole substantially larger than the 1.75in hole and a second data point for comparison with the finite-element models discussed in the section modeling buckling for a hollow cylinder. Strain was not measured during testing. Figure 53 shows the specimens with holes during tests.

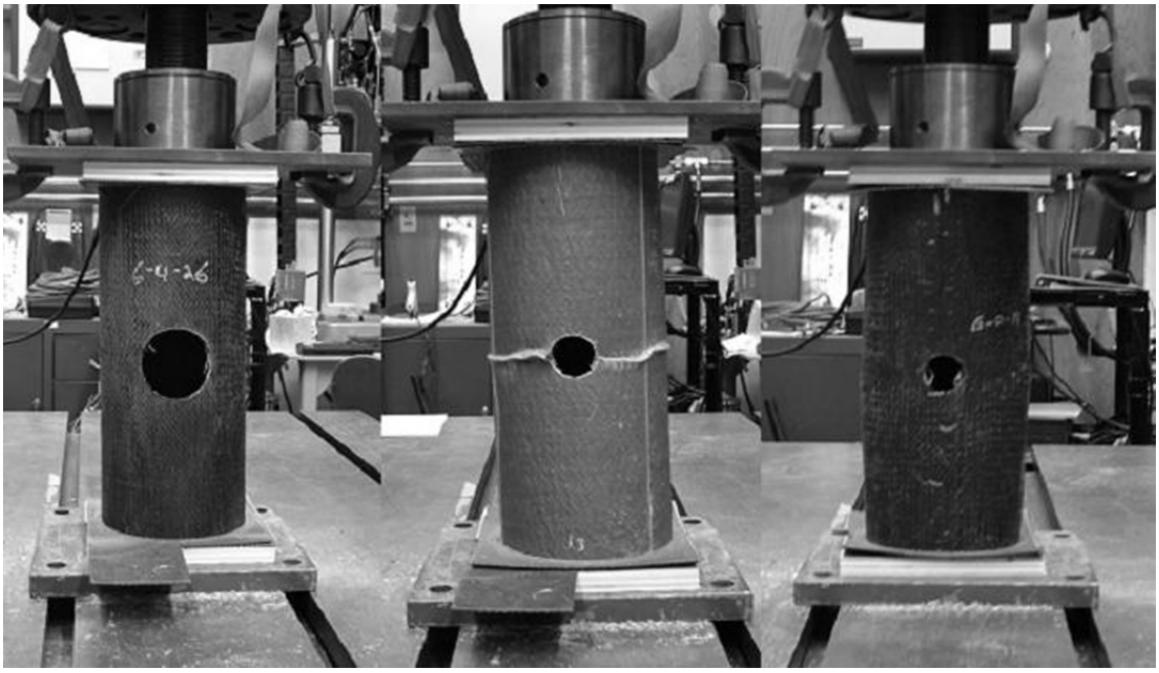

Figure 53 - DC 165-76, BC 165-45, and DC 165-45

Results for specimens with holes are in Table 23, for comparison, specimens without holes are in Table 17. Drilling holes significantly lowered the buckling capacity compared to cylinders without holes; a 1.75in hole reduced the capacity of bleeder carbon specimens by 51% and double carbon specimens by 46%. The strength drop for a specimen with a hole is large enough that special consideration should be taken for design of the apex of an arch. It is possible that it would be unconservative to design an arch based on the highest stress during filling, which generally occurs at the footing or the shoulder, and the strength of a cylinder without a hole.

FRP topped plywood end caps were used for all specimens with holes. This boundary type performed best out of all tested boundaries, but to generate an even load distribution in specimens with irregular edges, the plywood needed to crush around the cylinder prior to specimen buckling. Specimens that buckled before plywood crushing were not accepted as part of the mean or the COV because they had most likely loaded unevenly and failed around the hole at a local stress not indicative of the total load in the specimen. Plywood crushing was obvious from the sound it made during a test; the typical load for plywood crushing was 5.85kip-7.87kip; all specimens excluded failed below 7.87kip. The COV, after ignoring the low specimens, was low compared to prior results for specimens without holes and typical local buckling testing. Single carbon and bleeder carbon specimens without holes both had a buckling capacity COV over 15%. Donnell

(1934) tested common thin-walled metal cylinders made from brass, steel, and aluminum and found that buckling capacity COV was greater than 20% for isotropic, uniform metals, because even small deformities in the shell (on the order of the thickness) could result in substantially reduced buckling capacity, and these deformities could not be removed during manufacture. Low COVs are indicative of a failure dominated by a single uniform defect that is consistent for every specimen in the group, instead of being dominated by random imperfections. The effect of a sizeable hole is larger than the diameter inconsistencies in typical cylinders, and as such it dominates the failure response.

Table 23 Results of 6.50in Specimens with Holes

TYPE	Load (kip)	COV %	# Tested	# Accepted
Bleeder Carbon	11.1	7.8	14	11
Double Carbon (Small)	16.7	5.7	9	9
Double Carbon (Large)	10.7	7.5	8	7

Summary

Arches experience construction loads before concrete hardens, and at this time they rely only on the strength of the composite shell. The capacity for a section in axial compression is expected to be nearly equivalent to the capacity of the section in bending because both failures are precipitated by buckling of the compression face. Existing analytical models do a poor job of predicting this local compressive buckling of the composite tubes because of the extreme thinness of the tube, the large Poisson ratio from braid interaction, and the inability of the models to fully capture the complex fiber architecture of the tube. To establish the relative accuracy of these models and get baseline data for future modeling and immediate bridge safety, short specimens were tested in axial compression. These specimens had a variety of diameters and used one or two layers of carbon for the longitudinal reinforcing or bleeder as an abrasion layer over a layer of carbon. Two layers of carbon doubled the strength of the composite compared to one layer since it increased axial stiffness and thickness (which enhances radial stiffness), and bridged gaps in the first carbon layer. The bleeder layer gave a 50% increase in capacity without adding axial stiffness by increasing the thickness (thus enhancing radial stiffness) and bridging holes in the carbon. When filling an arch with concrete it has been necessary to cut holes in the composite. Preliminary testing indicates at least a 40% loss in axial capacity due to a 2.95in diameter hole in a 14.8in diameter carbon bleeder tube.

MODELING BUCKLING FOR A HOLLOW CYLINDER

Due to the poor compressive buckling capacity estimates of many of the analytical models discussed in the section compression of hollow FRP – and the inability of these models to predict the effect of drilling a hole in the composite and other geometric irregularities – a finite element model was constructed to help understand the results from the structural compressive testing. Abaqus Standard (Dassault Systemes, 2010) was used as the modeling platform. Models of the composite tubes were built based on the three 6.50in diameter, 15.0in long specimen lay-ups tested in axial compression as detailed in the last section. This section covers the element type selection, material characterization, and level of mesh refinement using linear elastic (eigenvalue) buckling analysis. Models were then constructed to study the effect of unbalanced loading and geometric imperfections on buckling capacity. Finite-element models of the composite cylinder were then constructed with a hole added at mid-height to simulate the concrete filling port, and the effect of the hole on compressive capacity is examined.

Selecting Analysis Parameters – Eigenvalue Buckling Analysis

The cylinder was modeled using shell elements. The cylindrical shell was restrained from out of plane motion and loaded by a constant shell edge load. Figure 54 shows load and boundary conditions for a cylinder. Edge displacements are restricted in x- and y-axes, edge rotations are restricted about the z-axis and load is applied normal to the circular ring surface of the cylinder (z-axis for an unperturbed cylinder).

Figure 54 - Load and Boundary Conditions for a Typical Cylinder Model

In an eigenvalue buckling analysis, the eigenvalue is the number that when multiplied by the applied load gives the buckling load. Instead of reporting the eigenvalue, the buckling load (in kips) is reported for easier comparison with the experimental results.

According to the Abaqus users manual (Dassault Systemes 2009), there are three elements (S4, S4R and the S9R5) that work well for shell buckling. The S9R5 element is a quadratic element with an intermediate node on each side and a central node that uses reduced integration through the depth. This element assumes thin shell behavior, which is consistent with the radius to shell thickness seen in the experimental tubes, but it cannot be selected from the Abaqus graphical user interface (GUI), making it cumbersome to use. The S4R element is a linear element (nodes only on the corners) with reduced integration. It requires a finer mesh than the quadratic element for the same level of accuracy, but reduced integration helps the run time. The S4R element is prone to hourglassing, sometimes producing fictitious buckling modes (Dassault Systemes, 2009). The S4 element results in models with longer run times for the same level of accuracy when compared with the other elements because it is linear and does not have reduced integration. However, the S4 element is an all-purpose shell element and is not prone to false buckling modes. Ultimately, the S4 element was selected for this study.

Selecting Material Properties

After choosing the S4 element type, the next step was to select a material model to best mimic the shell wall for the three types of 6.50in diameter tube lay-ups. In the Section Mesh Refinement, the best mesh density, which has 7650 equal size elements, is determined, and all analyses in this section rely on that mesh. For all models, the thickness was 0.035in for the e-glass layer, 0.027in for carbon, and 0.029in for the bleeder layer. These values reflect the measured thickness of the shell wall as seen in Chapter 2 on compression testing. All material models use predicted elastic properties, since insufficient experimental results exist for the exact fiber lay-up. See Material Assumptions for Classical Lamination Theory material assumptions.

Isotropic

The simplest material model, isotropic, assumes that the material has the same properties in every direction and requires only the elastic modulus and Poisson's ratio for inputs. Some buckling models (Brazier 1927 and Timoshenko 1935, 1961) assume uniform material properties. The tubes have different elastic moduli in the longitudinal and radial direction; the balanced modulus in Table 24 was taken as the square root of the multiple of the longitudinal and radial moduli, Equation 14. This approach is similar to the orthotropic buckling models in the comparison to models section that utilize the square

root of both principal moduli, compromising between the difference in longitudinal and radial elastic modulus.

Table 24 Material Properties for Isotropic and Engineering Constant Models

Title	**S C**	**B C**	**D C**
E_x **(Ksi)**	5740	4080	7180
E_θ **(Ksi)**	3650	2670	3050
$E_{balance}$ **(Ksi)**	4580	3290	4680
V_{12}	0.335	0.338	0.476
G_{xy} **(Ksi)**	1330	979	1610

$$E_{bal} = \sqrt{E_x E_\theta}$$ Equation 14

Poisson's ratio for the longitudinal, radial direction was used as the Poisson's ratio for the entire material. This model should not be a good prediction of the buckling strength and if the longitudinal elastic modulus were used for E_{bal}, the result would serve as an upper bound for the buckling capacity. This model predicts the same buckling pattern for all three models, Figure 55, which does not accurately reflect the double carbon specimens' tendency to buckle near the boundary. Table 25 gives the buckling capacity for each of the four models tested with each material type.

Table 25 Buckling Capacity of Material Models

Material Models	**Isotropic**	**Orthotropic**	**1-Layer**	**2-Layer**	**Experimental**
SC	243	236	162	153	68.7
DC	601	548	372	304	138
BC	417	390	210	197	101

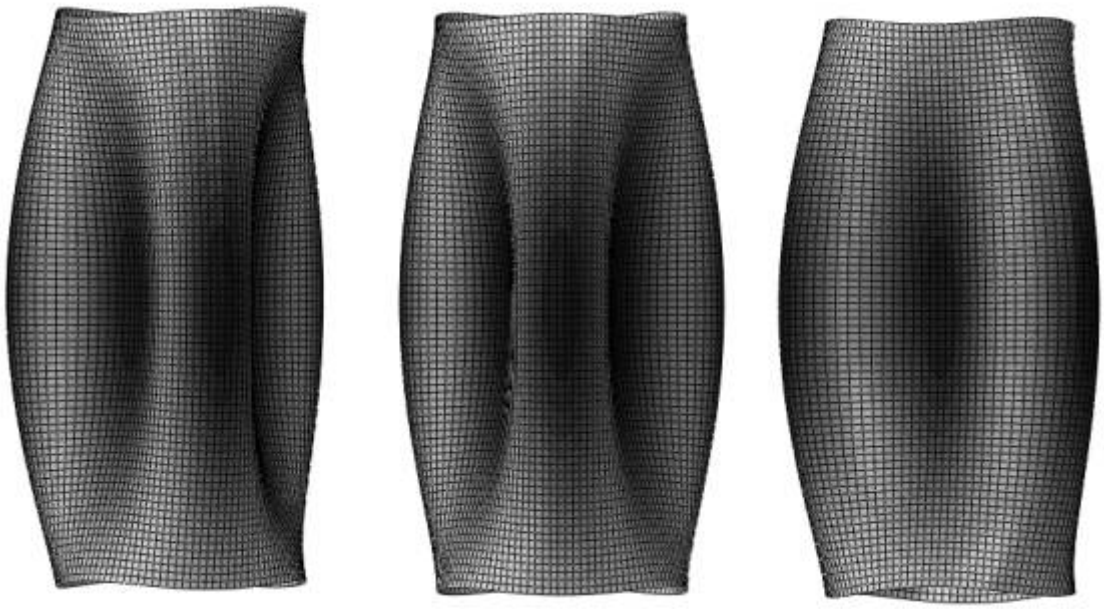

Figure 55 - Isotropic Model Single Carbon, Double Carbon, and Bleeder Carbon

Engineering Constant – Orthotropic

The engineering constant model allows moduli to be specified in orthotropic directions. Material properties are constant through the thickness, but the longitudinal moduli give a higher longitudinal stiffness and a lower transverse stiffness versus the isotropic model.

contains the independent properties for this material model, which were generated using Classical Lamination Theory. This model predicts different buckling shapes for each material model, and these shapes may reflect experimental results. As in Figure 56, double carbon specimens had a strong tendency to buckle near the support, and the model predicts buckling away from mid height. Also, the single carbon specimen shows a tendency to buckle at mid height. However, the response of the bleeder carbon and double carbon specimens was not identical as predicted by Figure 56. Double carbon specimens were more affected by edge buckling than bleeder carbon specimens and this was not reflected by the orthotropic model. The first two models assumed uniform properties through the cross section, and both models poorly predict load or buckled shape.

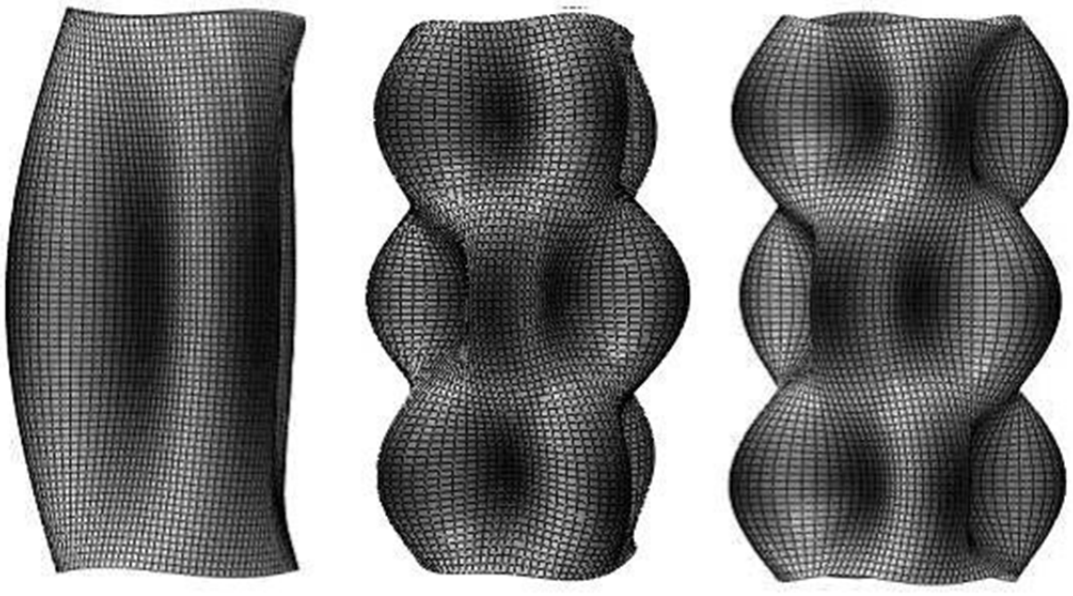

Figure 56 - Orthotropic Single Carbon, Double Carbon, Bleeder Carbon

Lamina with Two Layers per Braid

A braided layer is often treated as separate consecutive opposing layers (Bannon 2009). For this model, lamina material values were used with the micromechanics values for the 1, 2, and 3 material axes as in Table 26. In the Abaqus composite material editor, the materials were set to their appropriate angle (+/- 81 for the e-glass and +/- 22 for the carbon fiber). Abaqus calculated the final stiffness in the cylinder's longitudinal, radial and transverse directions during the solution phase. For this material model (and the one layer per braid material model described in the next section), the bleeder material is modeled as an isotropic layer with uniform properties in each direction. It is then added as an additional layer in the material model angled at 0 degrees. This model predicts a torsional mode for tube buckling as shown in Figure 57, which was not experimentally observed. Laminate composite modeling performed by Weaver (2002) shows a similar torsional buckle using a symmetric laminate based on coupled bend/torsion. Weaver's model showed a 30% reduction from a torsional buckling mode that could be avoided by using a different laminate schedule that minimizes flexure/torsion coupling. Both laminate schedules proposed by Weaver (2002) had the same classic buckling loads using analytic models. In this material model torsional buckling comes from the stacking of the carbon laminates, an outer layer 22 degrees and an inner layer of oriented at -22 degrees. The tube becomes stronger in the 22-degree direction because it is further from the neutral axis and adds higher bending resistance, allowing the tube to buckle in the opposite direction. In an actual braid the +22 and –22 layers interact and both affect the

full thickness of the carbon layer, so torsional buckling should not occur for a braided composite.

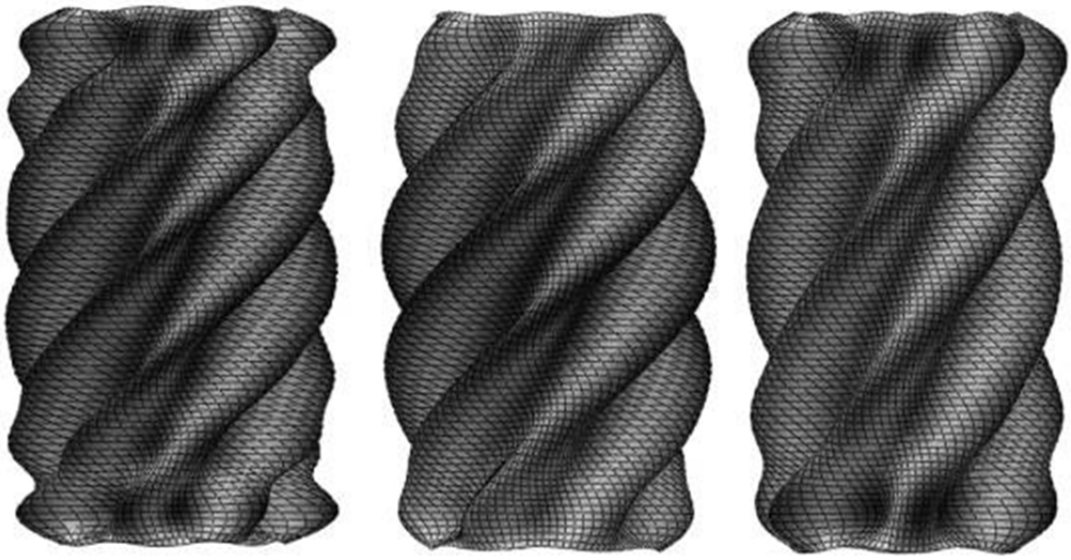

Figure 57 - 2-Layer/Braid Model Single Carbon, Double Carbon, Bleeder Carbon

Table 26 Properties for Lamina 2-Layers

Property	**Carbon**	**E-Glass**	**Bleeder**
E_1 **(Ksi)**	15500	5420	711
E_2 **(Ksi)**	1900	1670	711
v_{12}	0.266	0.283	0.334
G_{12} **(Ksi)**	434	437	225

Lamina with One Orthotropic Layer per Braid

In this approach each braided composite layer was treated as a single orthotropic layer in the Abaqus composite editor. A micromechanics worksheet was created to calculate the stiffness, shear stiffness, and Poisson's ratio of each layer treating it as a two-layer composite with opposite directional plies that occupy the same space (+/-22 degrees for the carbon, +/-81 degrees for the e-glass). These properties, in Table 27, were entered into a lamina material model in Abaqus for each material. The e-glass and carbon braid properties were stacked in the Abaqus composite editor and positioned at 0 degrees, because the angular direction was already accounted for by the reported material

properties. This model had a simple adjustment between single carbon, double carbon, and bleeder carbon tubes where only an additional layer needed to be added or subtracted using the Abaqus composite editor.

This model consistently produced the most reasonable buckling shapes based on comparisons with the experimental data. For the single carbon and carbon bleeder specimens the tube is predicted to buckle at mid span as shown in Figure 58, which is consistent with experimental results where a majority of specimens broke away from the support. Double carbon models buckle in five half-sine waves over the height of the model. This buckled shape has a maximum deformation close to the edge of the tube, and 90% of the experiments on double-carbon tubes exhibited end failures.

Table 27 Engineering Constant Properties 1-Layer

Property	**Carbon**	**E-Glass**
E_x **(Ksi)**	9530	1640
E_y **(Ksi)**	1650	5160
ν_{xy}	1.085	0.109
G_{xy} **(Ksi)**	2260	608

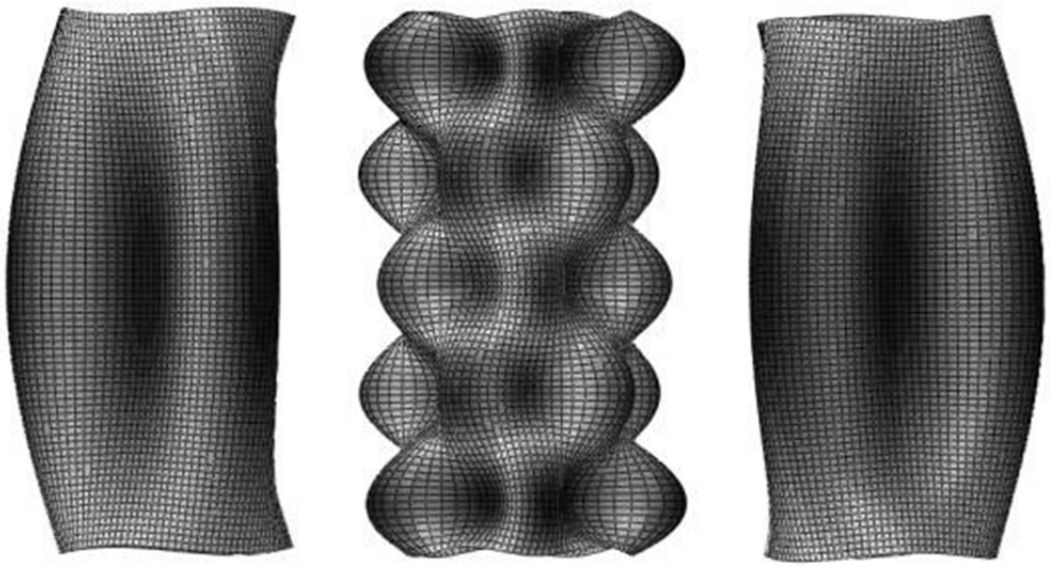

Figure 58 - 1-Layer/Braid Model Single Carbon, Double Carbon, Carbon Bleeder

Mesh Refinement

After deciding on the 1-layer per braid material model, a mesh refinement study was performed on all three material types to determine the mesh density required to produce an accurate buckled shape and buckling load. All meshes were uniform with equal-sized elements. The total number of elements ranged 300 for the coarsest mesh to over 47000 elements in the finest mesh. In all cases the element was selected to be a quadrilateral and ABAQUS defaults to make all elements as close to square as possible for a given geometry; for a cylinder all elements were square because there were no irregularities for ABAQUS to have trouble meshing. The number of elements has a substantial impact on computation time and solution accuracy. The best element size converges to a consistently accurate solution in an acceptable time, since the large matrix of analyses run in this modeling program prohibits a very high degree of mesh density. 7650 elements, corresponding to an element edge length of 0.197in, were used for all additional modeling. The 7650 element mesh averages 1 minute per buckling solution, the 18055 element mesh averages 8 minutes per buckling solution; the improvement in computation time is worth the sacrifice in computation accuracy, shown in Table 28. Percent change in Table 28 is the change relative to the finest mesh.

AEWC Advanced Structures & Composites Center
5793 AEWC Bldg
University of Maine
Orono, ME 04469-5793

Telephone: 207-581-2123
FAX: 207-581-2074
contactaewc@umit.maine.edu
www.aewc.umaine.edu

Table 28 Mesh Refinement Study

Number of Elements	Percent Change	Load (Kip)
Single Carbon		
300	18.1	42.9
1887	2.87	37.4
3942	1.38	36.9
7650	0.387	36.6
18055	0.213	36.4
30200	0.0672	36.4
47685	-	36.4
Bleeder Carbon		
300	18.8	56.4
1887	3.03	49.0
3942	1.47	48.3
7650	0.932	47.2
18055	0.460	47.7
30200	0.077	47.4
47685	-	47.4
Double Carbon		
300	24.2	103
1887	6.91	88.3
3942	3.69	85.7
7650	1.29	83.6
18055	0.672	83.2
30200	0.178	82.5
47685	-	82.7

Experimental Imperfections

The eigenvalues predicted by the different material models are considerably higher than the experimentally observed buckling loads. However, all models have thus far assumed a perfect cylinder loaded by a perfectly concentric load. No fabricated tube is a perfect cylinder, and manufacturing imperfections create diameter changes and curvatures over the length. Also, in many tests the load was eccentric, as seen from the potentiometer data reported in compression of hollow FRP. Therefore, applying a uniform load does not accurately reflect the load seen by many specimens. To see the effect of these two inconsistencies on the buckling capacity, modified models were constructed using the uniform mesh with 7650 elements selected in the mesh density study and using one orthotropic layer per fabric layer to model the composite shell wall. Other imperfections that will not be covered are local variations in thickness, stiffness, and waviness.

Effect of Unbalanced Loading

Two different unbalanced loads were applied to the tube: one where the load varies linearly from 0 to double the average load across the cylinder diameter, and a second case where the load varies linearly from 2/3 of the average load to 4/3 of the average load across the cylinder diameter. The first unbalanced load represented the case where one side of the cylinder is entirely unloaded while the second case was for a cylinder where there was some load everywhere – a more moderate loading case. Table 29 displays the predicted buckling capacity of cylinders subjected to unbalanced load. Capacity was slightly reduced by the moderate unbalanced load: the bleeder carbon model reduced by only 1.5% and the double carbon model by 9.1%. The higher unbalanced load produced a 28% to 33% reduction in capacity that brings the buckling load closer to the experimentally observed values. The experimental buckling load was still considerably lower than the model-predicted buckling load, however. Further, many specimens did not show evidence of eccentric load; plywood loading platens deformed based on load reducing eccentricity from uneven edges. Other defects must also contribute to the discrepancy between experimental and modeled buckling load.

Table 29 Capacity of Cylinders with Unbalanced Loads

TYPE	SC	BC	DC
Regular	162	210	372
Moderate Unbalance	150	207	337
Full Unbalance	109	152	249

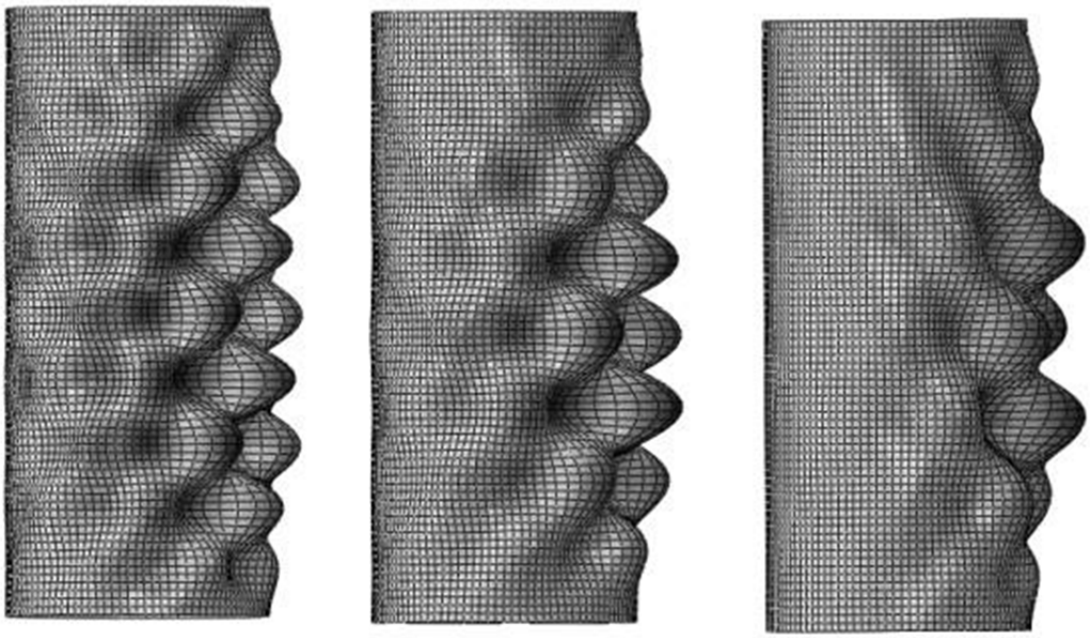

Figure 59 - Uneven Load Models Single Carbon, Double Carbon, Bleeder Carbon

Effect of Geometric Imperfections

Geometric irregularity is a consequence of manufacturing that was present in the tested specimens. The cylinder used for mesh refinement and material model determination was a perfect cylinder and was not indicative of experimental specimens. Here, geometric imperfections that affected the full geometry of the cylinder are considered, such as cross sectional diameter variation and longitudinal curvature. Local, node-level variations in thickness and stiffness were ignored, however they also potentially affected experimentally determined buckling capacities.

The initial perfect cylinder model was created in the Abaqus GUI. Abaqus generates an input file from its GUI and then loads this file in the 'job' module when running an analysis; Abaqus can also load an input file directly without a model. The input file contains the nodal connections, coordinates, and lay-up scheme for each part as well as the global material properties, boundaries, loads, and part interactions. To perturb the mesh into an irregular geometry, only the nodal locations needed to be modified – connections and material properties remain constant. A MATLAB routine was written to modify the nodal coordinates into a variety of shapes keeping all of the boundary and connectivity information constant (see Walton (2011) for this code). The MATLAB routine has five inputs: lay-up, hole size (see eigenvalue buckling analysis of tubes with

holes), perturbation type, scale, and extra – a way of altering the perturbation type for models with holes (see effect of geometric imperfections in tubes with holes).

Table 30 contains the buckling loads calculated from the Abaqus eigenvalues for the cylinders with a variety of defects. Defects are explained in subsequent sections. Defects range from the double-carbon 0.10in arc perturbation with a 14% increase in capacity to the single carbon, single curvature perturbation with a reduction in capacity of 61%. As discussed in the following sections, the size of the defects falls within the range of actual defects that were measured in the test specimens.

Table 30 Strength of Cylinders with Geometric Imperfections

Deformation Type	SC	DC	BC
Non-Deformed	163	372	210
Hourglass - 0.02in	148	369	192
Hourglass - 0.06in	122	322	161
Hourglass - 0.10in	101	281	135
Bulge - 0.02in	169	371	220
Bulge - 0.06in	166	366	215
Bulge - 0.10in	161	357	210
Single Curvature - 0.10in	148	351	192
Single Curvature – 0.30in	96.1	245	129
Single Curvature – 0.50in	63.4	171	86.9
Double Curvature - 0.10in	151	366	196
Double Curvature - 0.06in	120	311	161
Double Curvature - 0.50in	94.9	260	131
Ellipse - 0.10in	162	369	209
Ellipse - 0.06in	153	345	200
Ellipse - 0.50in	135	310	178
Arc - 0.10in	181	424	225
Arc - 0.06in	114	291	149
Arc – 0.50in	72.0	198	98.0

Inconsistent Diameter

The laboratory specimens exhibited a small but measurable amount of diameter inconsistency. Most specimens varied in perimeter from 20.2in to 20.6in (over the full ~11m length of the infused part). The local variation in the part (over the 15.0in specimen height) was usually small, but 0.03in changes in diameter were measured in nearly every specimen, and 0.08in or larger changes in diameter (over 0.24in changes in

perimeter) from top to mid height or mid height to bottom were measured in ~25% of specimens, and there is a rough correlation between diameter change and buckling capacity, discussed in diameter inconsistency. Diameter variation was caused by inconsistency in the glass diameter constraint layer, or over-tensioned carbon fiber restricting the diameter of the tube. Models were created to reflect these diameter inconsistencies in the specimen. This took on three different forms: hourglass shape (diameter contraction in the middle), bulge (diameter expansion in the middle), and ellipse (cross section has a minor radius and a major radius).

Hourglass

The hourglass shape was a uniform and symmetric reduction in diameter. Diameter loss was based on the height of the cylinder varying along a sine wave with period equal to the height of the cylinder and amplitude equal to variable *scale*. The peak of the sine wave occurs at the ends of the tube and the trough of the wave occurs at mid height making the mid height the smallest diameter. Any sharp discontinuities in diameter present in actual specimens are visible during manufacture, and such specimens are rejected, so the smoothed shape of the sine wave was assumed to be a reasonable representation of the diameter variation in an actual cylinder. The equation for the diameter change, Equation 15, depends only on nodal height *Z*.

$$radius\_change = \frac{-\sin\left(\left(Z - \frac{Z_{\max}}{4}\right)\left(\frac{2\pi}{Z_{\max}}\right)\right)}{2} * scale \qquad \text{Equation 15}$$

After calculating diameter change, the new diameter at each node was converted back into rectangular coordinates. Figure 60 contains a wire mesh plot of the deformed nodal locations before buckling analysis. Note that this shape has an extreme degree of hourglass – ten times the maximum used in analysis – and is a graphical representation, not actual input coordinates.

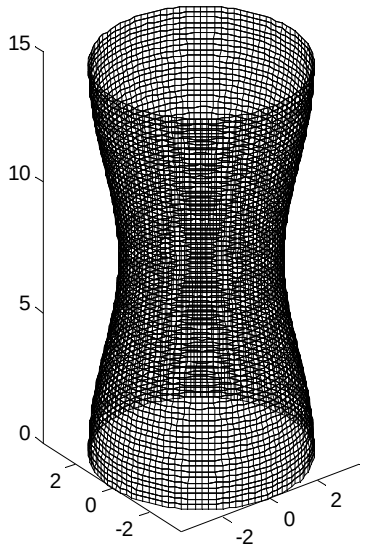

Figure 60 - Wire mesh of hourglass perturbation, 0.984in radial decrease at center

Buckling capacity was greatly affected by this perturbation, but the buckled shape remained the same for many cases. Table 30 contains the buckling capacity for cylinders without holes and with geometric irregularities. With a 3.08% loss in diameter, the model experienced a 24% to 38% loss in capacity depending on lay-up. The single carbon and carbon bleeder models have no appreciable shape change with any of the three hourglass shapes tested or the initial perfect cylinders. The double carbon model with the lowest degree of hourglass tested (0.02in) retained the buckled shape of the perfect double carbon cylinder, as in the left of Figure 61. The middle and highest values of hourglass deformation modified the buckled shape into the center-buckled shape shown in the right of Figure 61. Measured levels of diameter variation over the length of most specimens fell between the perfect cylinder and the lowest hourglass shape (or bulge shape) and from the perfect shape to the 0.02in contraction there was no change in buckled shape. The different buckled shape of the more irregular double carbon cylinders indicates that moderate hourglass may have contributed to the one of ten double carbon specimens that broke at its center. However, the specimen that broke at its center had a higher buckling load than any other double carbon specimen making it unlikely to be caused by an imperfection.

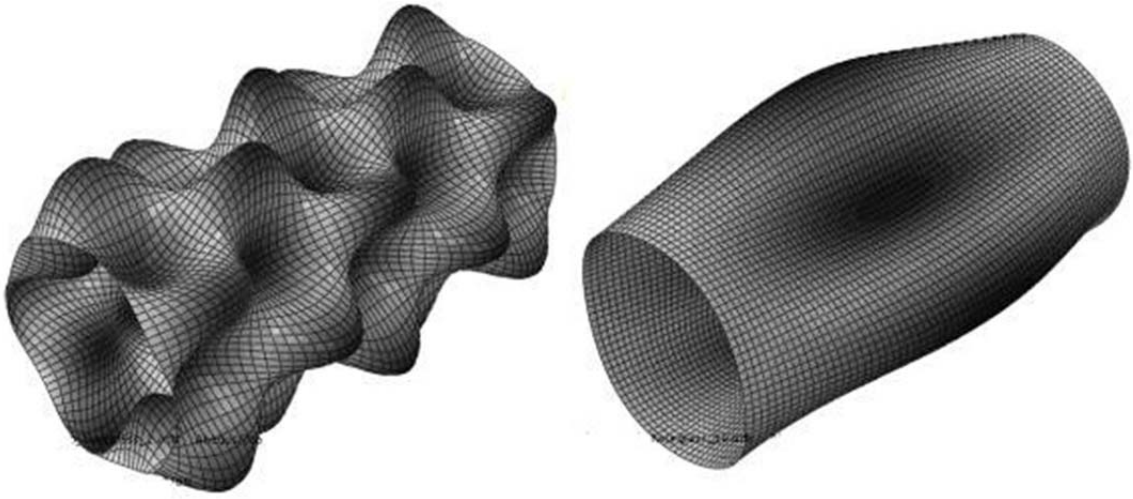

Figure 61 - Comparison of Double Carbon 0.02in and 0.10in Hourglass

Bulge

The bulge shape was the inverse of the hourglass shape – the middle increased diameter and the edges decreased diameter. Modeled with the diameter varying in proportion to height, a full sine wave, with amplitude *scale*, was used with the peak in the center and the troughs at the ends. The bulge shape originated from the same manufacturing inconsistencies as the hourglass and the differentiation between these shapes was based on where the individual specimens were cut from the master tube. The bulge magnitude was computed as the negative of Equation 15.

To translate from rectangular coordinates to cylindrical coordinates a rotation, θ, is calculated at all points (initially radius is constant for the cylinder). The radius is modified by Equation 15, and nodal locations are converted back to rectangular coordinates. Using a 10x exaggeration over the largest bulge used in modeling, Figure 62 shows the nodal positions of a bulged cylinder.

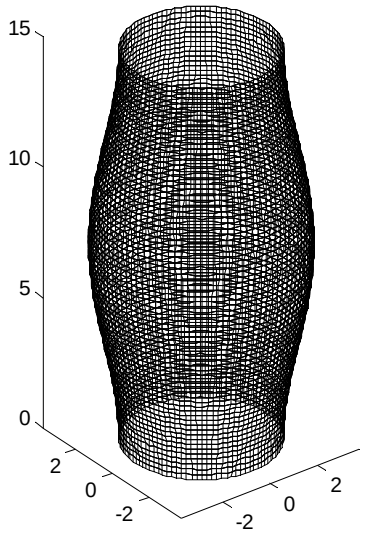

Figure 62 - Wire Mesh of a Bulged Cross Section, 0.984in Radius Increase at Center

Bulging the center of the cylinder did not substantially change the buckling capacity, but it did alter the buckled shape for most models. In Table 30, the largest loss in capacity (4.35%) was the 0.50in bulge in a double carbon model – much smaller than the 22% loss in capacity for the equivalent hourglass shape. In many circumstances, the bulge increased capacity and having a small bulge in the single carbon and bleeder carbon models increased the buckling capacity by as much as 5.1%. Accompanying the change in capacity was a change in buckled shape. No models with a bulge buckled at the mid height of the cylinder – the dominant buckling mode transferred the maximum deformation from the middle to the edge. Even a small bulge (0.02in – too small to be detected by sight) resulting in edge buckling as shown in Figure 63, indicating that buckling mode is very sensitive to a bulge. This is consistent with the large number of bleeder carbon and single carbon specimens that buckled near the edge in bearing-buckling failure. As with no bulge, for double carbon specimens any bulge maintains bearing-buckling failure; experimentally, 7 of 8 specimens failed in bearing-buckling.

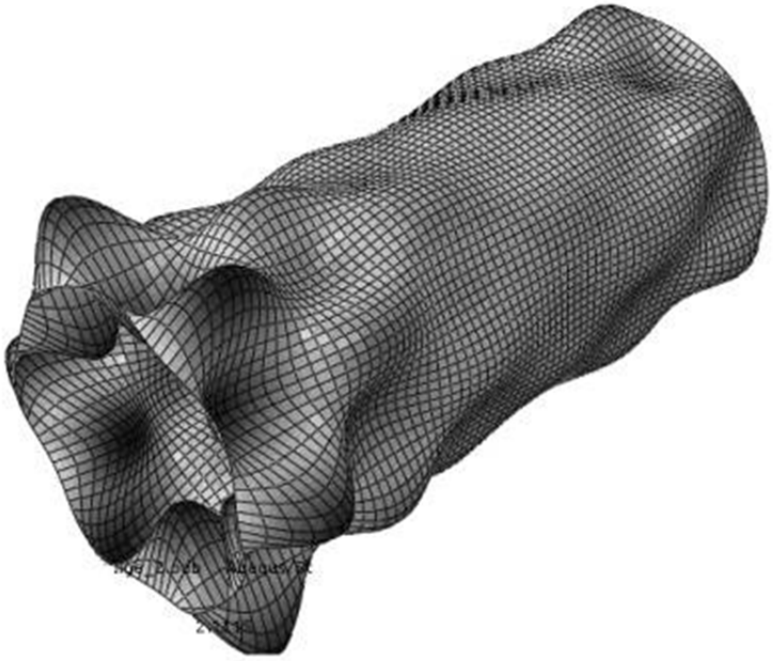

Figure 63 - Buckled Shape, Bleeder Carbon, 0.02in Bulge Perturbation

Elliptical Shape of the Cross-Section

An elliptical cross-sectional shape was not measured in the 6.50in diameter experimental specimens, but it could be caused by improper manufacturing and is a possible side effect of bending stresses (see Bend Testing of Hollow FRP Tubes for a discussion on ovalization). The perimeter of the ellipse is the same as the regular circular cross section, only the minor radius is smaller by a length of *scale* and the major radius is longer by a compensating amount. Where r_A and r_B are the radii, perimeter was calculated using the second Ramanujan approximation, Equation 16 (Sykora 2010), which matches the Taylor series expansion up to the 9th order.

$$perimeter = \pi\left(r_A + r_B\right)\left[1 + \frac{3\left(\frac{\left(r_A - r_B\right)^2}{\left(r_A + r_B\right)^2}\right)}{10 + \sqrt{4 - 3\left(\frac{\left(r_A - r_B\right)^2}{\left(r_A + r_B\right)^2}\right)}}\right] \qquad \text{Equation 16}$$

This equation was used in conjunction with an iterative process to input a given perimeter and minor radius A to find the major radius B (the circular radius is initially assumed). Figure 64 shows a wire mesh of the modified shape using a 0.984in reduction in the minor radius (from a circular 3.25in radius) and the resulting major radius to keep a constant perimeter. The elliptic shape is exaggerated by a factor of 2.

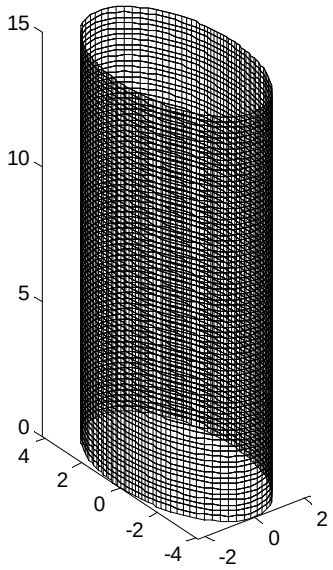

Figure 64 - Wire Mesh of Ellipse Cross Section, Minor Radius Reduced 0.984in

Elliptic perturbation had a smaller effect on capacity than some other perturbations, including the hourglass shape (Table 30). The worst-case ellipse (single carbon 15.4% reduction in minor axis) produced a reduction of 17%, a significant amount, but smaller than hourglass or curvature effects. The least severe ellipse (3.08% reduction in minor axis) was closer to the actual elliptical shape recorded during bending tests (see Bend Testing of Hollow FRP Tubes). They produced a modest 1.0% decrease in the double carbon capacity. Bending specimens should see a reduction in capacity from ellipse shaping, bending stress warps the cross section into an ellipse. Ellipse shaping was negligible on the tested compression specimens.

Elliptical cross sections have a different buckled shape from the circular control that depends on radius change. In Figure 65 a small reduction in radius (0.10in) retains the buckled shape of a circular section while the severe ellipse has little deformation at the middle and has heavy wrinkling on the minor axes near the edges. Double carbon, in

Figure 66, had a less pronounced shape change between different ellipses. A small radius reduction kept heavy deformations along both axes and a large radius reduction concentrated buckling deformation on the minor axes, but both had buckled shapes dominated by edge effects.

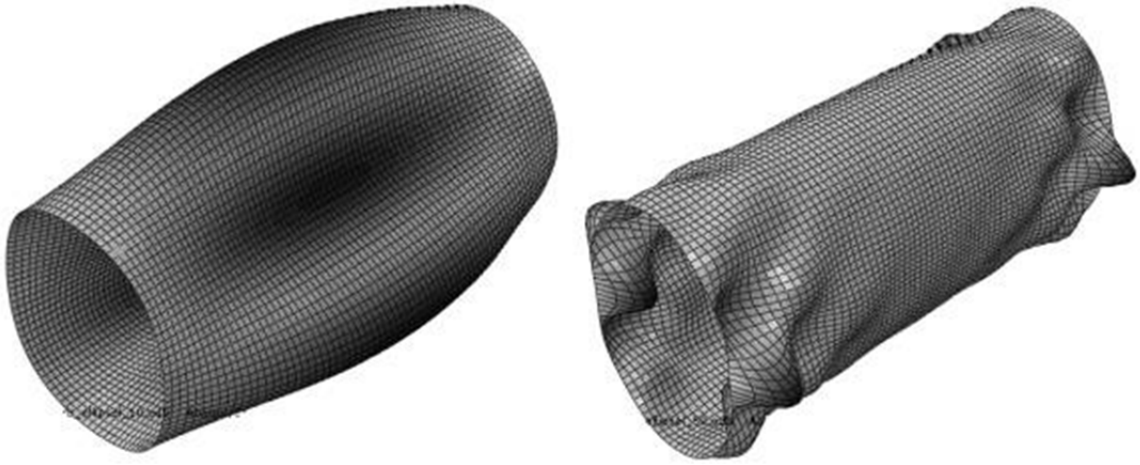

Figure 65 - Single Carbon: 0.10in, 0.50in Minor Radius Loss

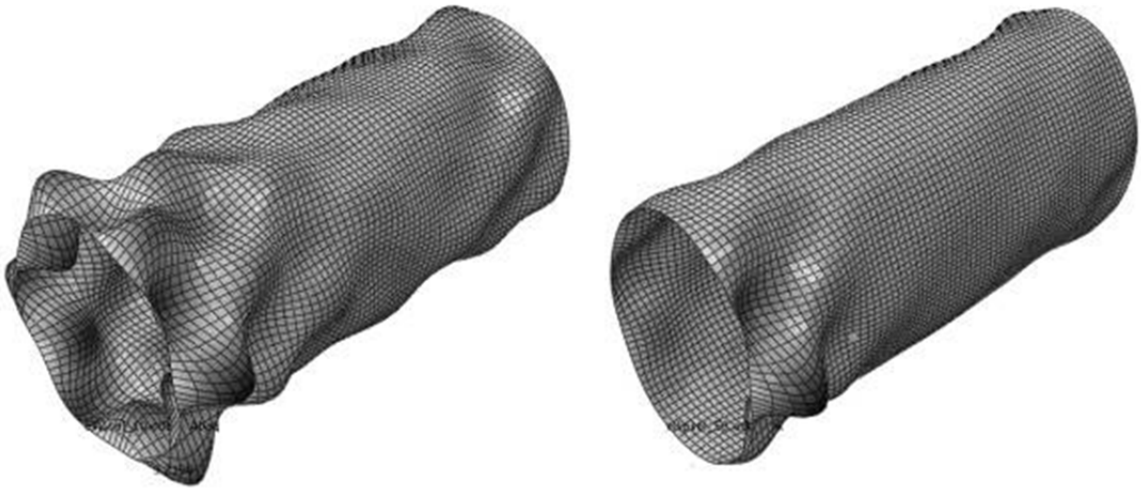

Figure 66 - Double Carbon: 0.10in, 0.50in Minor Radius Loss

Curvature of Section

Experimental specimens were constructed as nominally straight tubes, and an effort was made to manufacture every tube to be as straight as possible. However, some tubes still had locally curved sections. A similar analogy can be made for arches where certain sections are not as tight against the formwork as anticipated and an irregular curvature

occurs. All of the long, 6.50in diameter tubes except tube SC 165, 1 had a curvature measurement taken, which was reported as a deviation from a central line every 12.0in in length along the tube. This information is in Bend Testing of Hollow FRP Tubes. The tube was placed on supports as in the next section with a tensioned line over the tube positioned at the center points of the tube over the supports. A square with a level was used to find the flat portion at the top of the cross section of the tube and measure the distance from this flat spot to the line. The variation over 12.0in was as high as 1.26in, but a more typical value was .118in to 0.39in. The 1.26in curved section at the center of tube 3 was not used for compression testing. In the model, three perturbations were made including 0.10in (the typical variation), 0.06in (higher than typical but near or below the maximum of every long tube), and 0.50in (higher than the maximum for most tubes but much lower than the absolute maximum of 1.26in). Three general models were created to reflect the inconsistent curvature of the longitudinal specimens: single curvature (cross section is perturbed into a half sine wave shape with ends parallel), double curvature (cross section is perturbed into a half sine wave top and bottom – ends are parallel but do not occupy same x and y coordinates), and a circular arc. In all cases, a portion of the tube – either the top end or the center – is deflected by a magnitude of the variable *scale*. All three perturbations are based on maintaining the perfect uniform circular cross section, but the arc formulation rotated the cross section.

Braid angle fluctuation is ignored in this analysis. Curved tubes do not have a constant fiber angle. Bending the specimen puts increased tension on the outer face (smaller braid angle, increased stiffness) and compression on the inner face (larger braid angle, decreased stiffness). The model implemented assumes a constant braid angle and constant material properties. However, it must be noted that the carbon fiber is at a braid angle where a small fluctuation of even one or two degrees from the nominal value is expected to change the longitudinal stiffness as much as 10% based on a micromechanics analysis of the composite cross-section. Any specimen with variable stiffness would behave differently in the buckling analysis than the uniform stiffness model used.

Single Curvature

For single curvature, x coordinates of all nodes were perturbed by Equation 17, where Z is the height of the cylinder at a node and *scale* is the magnitude of perturbation.

$$Y_{change} = scale * \sin\left(\frac{Z\pi}{Z_{\max}}\right) \qquad \text{Equation 17}$$

When Z is zero or Z_{max}, the equation will equal zero (the top and bottom remain in their initial position). Between the top and bottom the cross section is displaced out of plane

by a sine wave with maximum amplitude *scale*. A half sine wave was selected because it is a smooth continuous function and the buckled shape predicted by Abaqus for a perfect cylinder has a half sine wave shape for the bleeder carbon and single carbon models (with a triple sine wave around the perimeter). Figure 67 shows a wire mesh rendering of the single curvature perturbation at a mid height displacement of 0.984in.

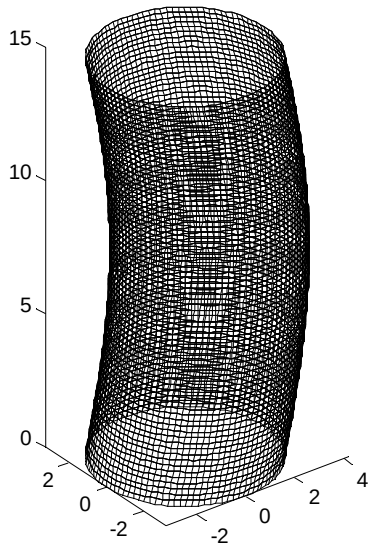

Figure 67 - Wire Mesh of a Single Curvature with 0.984in Perturbation

The single carbon and bleeder carbon models all had the same buckled shape regardless of magnitude. The double carbon models all had a similar shape but the least perturbed model appeared noticeably different from the other two material types. Figure 68 shows the buckled shape of the single curvature perturbation for the (left) bleeder carbon material with a 0.5in center perturbation and the (right) double carbon material with a 0.10in perturbation. Single curvature dominated failures would have appeared as a kink forming at the mid height of the cylinder on a single side of the cylinder – an observed failure for single carbon and bleeder carbon specimens. The least severe double carbon single curvature model produced a shape with maximum deformation at the middle, but high and irregular deformations near the edges.

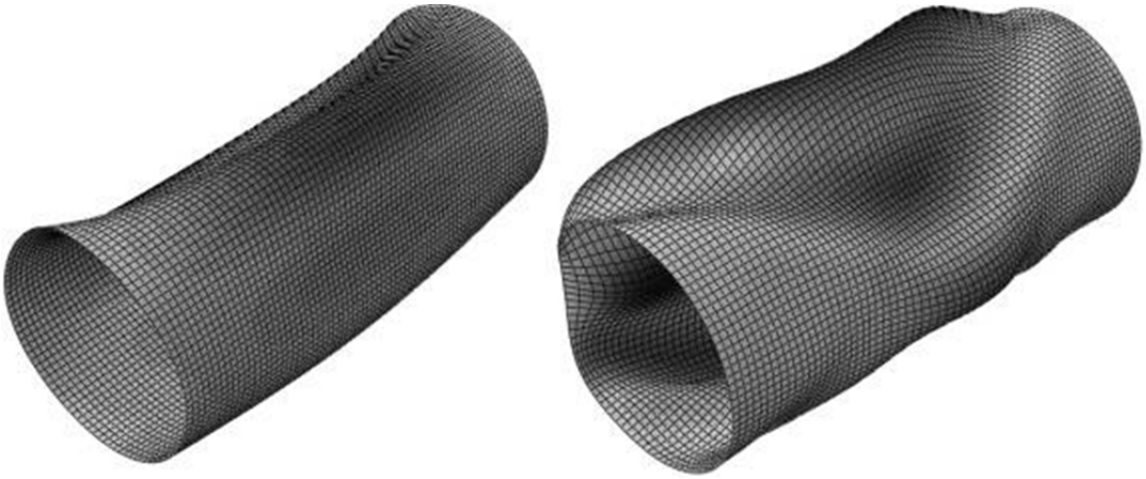

Figure 68 - Single Curvature: Bleeder Carbon 0.5in, Double Carbon 0.10in

Single curvature perturbation produced large reductions in capacity compared to most of the deformed shapes (Table 30). The single curvature model put the center of load away from the centroid of the cylinder, an eccentric load, which produced a bending force in the shell wall and increased the compressive stress on the inside curved face of the cylinder. Reduction of 54% (double carbon) to 61% (single carbon) resulted from a maximum center perturbation of 7.7%. In all three material cases the single curvature perturbation produced buckling loads near or below the average experimental buckling loads, suggesting that this one defect alone – without considering multiple defects, local material stiffness fluctuation, or local wall thickness variation – could have produced the reduction seen from the model to the actual load.

Double Curvature

During manufacture, tubes were hand straightened, but some bends could not be entirely removed. Often, when attempting to straighten a bent section, the result was two bends in close proximity. The magnitude of these bends was large compared to local diameter variations such as the bulge and hourglass, but difficult to correct during manufacture. Models were run where the total displacement over a 6.50in height was 1.7% to 7.7% of the diameter. The double curvature shape has top and bottom cross sections that are both normal to the height of the cylinder but they are not centered at the same location: the top is displaced by the magnitude of the variable *scale* from the bottom face. A conditional set of equations was written in Equation 18.

If $Z > \frac{Z_{\max}}{2}$ then $Y_{change} = -scale * \sin\left(\frac{Z\pi}{Z_{\max}}\right) + 2$ Equation 18

Else $Y_{change} = scale * \sin\left(\frac{Z\pi}{Z_{\max}}\right)$

The double curvature shape appears incomplete; the cylinder terminates at the points of most rapid bend. The double curvature model is in total a half sine wave imposed on the shape with a quarter sine wave in each direction starting from the center height of the cylinder. This is a single approximation of the many possible specimen imperfections.

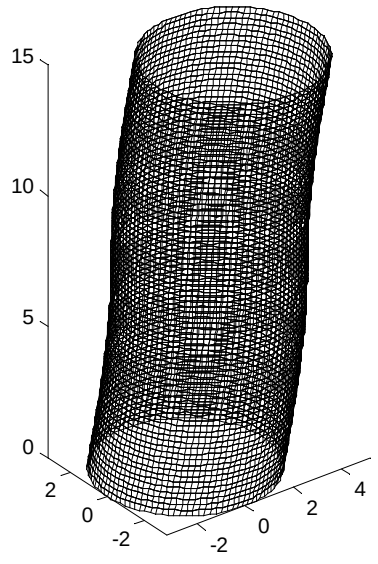

Figure 69 - Wire Mesh of a Double Curvature Section, Top Perturbed 0.984in

Double curvature buckling load reductions were less severe than single curvature models. Instead of reductions near 60% for the 7.7% diameter perturbation, double curvature had reductions from 30% (double carbon) to 42% (single carbon). The buckled shapes for models with double curvature perturbation had a typical failure shape; 8 of 9 had a similar shape to the unperturbed buckling model for the given material. As the double carbon became more perturbed it buckled closer to mid height, as seen in Figure 70. Results were consistent with the observed failures of the experimental specimens where

the vast majority of double carbon specimens failed near the edge while many of the single carbon or carbon bleeder specimens would fail in the measured gauge length.

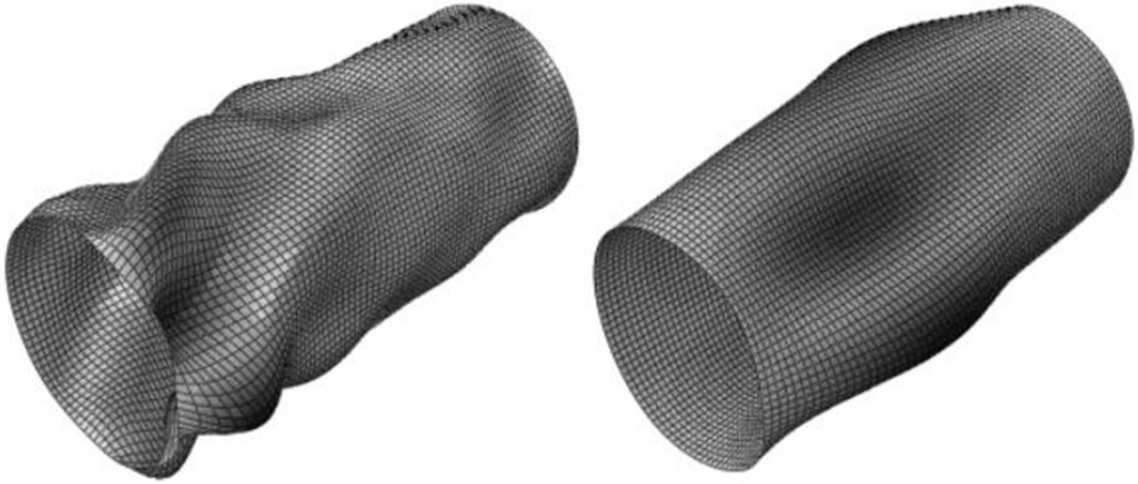

Figure 70 - Double Carbon, Double Curvature 0.10in and 0.5in

Circular Arc

Upon inspection it is impossible to tell whether the organic curvature in a cylinder is closer to a sine wave or a circular arc. The arc perturbation is an important shape that, like the ellipse perturbation, is real and will be in every arch. Unlike the ellipse, the arc shape is used in buried arch bridges. The circular arc was a difficult shape to mathematically construct and an intermediate radius of curvature was calculated, Equation 19

$$radius = \frac{\sqrt{\frac{Z_{\max}{}^{2}}{2} + scale^{2}}}{2\cos\left(\frac{\pi}{2} - \arcsin\frac{2Scale}{Z_{\max}}\right)}$$

Equation 19

Radius of curvature was used in the expression for calculating the new *Y*, Equation 20 and *Z*, Equation 21, coordinates based on rotating the circular cross section. *X* coordinates remain constant during this analysis.

$$Y_{new} = \cos\left(\frac{\arctan\left(Z - \frac{Z_{\max}}{2}\right)}{radius}\right)(radius - Y) - radius \qquad \text{Equation 20}$$

$$Z_{new} = \sin\left(\frac{\arctan\left(Z - \frac{Z_{\max}}{2}\right)}{radius}\right)(radius - Y) + \frac{Z_{\max}}{2} \qquad \text{Equation 21}$$

Figure 71 shows a deformed cross sectional shape with a 1.0in perturbation at mid height. A difference between this model and the similar single curvature model was that the load rotates with this model to follow the rotation of the shell instead of performing a p-delta analysis; this rotation is more indicative of the stresses propagating through the shell of an arch as opposed to a compression test.

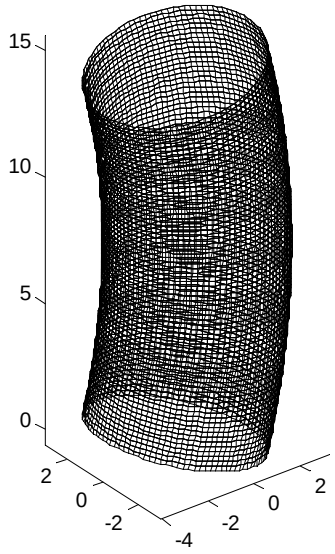

Figure 71 - Wire mesh of an Arc Deflection, Middle Perturbed 1.00in

In Table 30, buckling loads for perturbed models, the double carbon 0.10in arc shows an increase in capacity of 14% over the perfect cylinder. This implied that moderate arc curvature of the cylinder helps the buckling capacity. The steep curvature models, 0.5in centerline perturbation, – beyond what has been intentionally manufactured, but in the range of possible defects – has a severe reduction in capacity similar to the single curvature model (56% reduction in the single carbon capacity). The single curvature and the arc curvature models both impose a central bend in the cylinder, and at the extreme range of what was measured this defect alone was capable of reducing the capacity by over 50%, giving a buckling load near the experimental average. The deformed shape (Figure 72) from this analysis was in all cases very similar to the deformed shape from the single curvature model.

Figure 72 - Double Carbon with 0.5in Arc Perturbation

Eigenvalue Buckling Analysis of Tubes with Holes

When arches are concrete filled with concrete from the apex, a hole drilled into the apex compromises the cross sectional rigidity and the capacity of the compressive face of the arch. A principal reason for building a finite element model was to see the effect of the filling hole on buckling capacity. Experimental reductions in axial compressive capacity can be compared to model reductions as a way of verifying the effect of a hole on structural integrity. Three lay-ups are considered: bleeder-carbon with a small hole, double-carbon with a small hole and double-carbon with a large hole. Hole sizes are the same as those in the test specimens.

Models Without Damage Around Hole

The typical cylinder from previous sections was defined in the parts module. A new part was defined – a solid circular cylinder of diameter 1.75in for the small hole and 3.0in for the large hole – reflecting the holes cut into the experimental specimens. The Abaqus

'cut instance' tool was used in the assembly module to cut the initial shell cylinder with the new solid cylinder, as a cylindrical hole saw removed a section from the experimental specimens. All other properties – element type, mesh size, and material properties – remained the same from Mesh Refinement, an ideal cylinder.

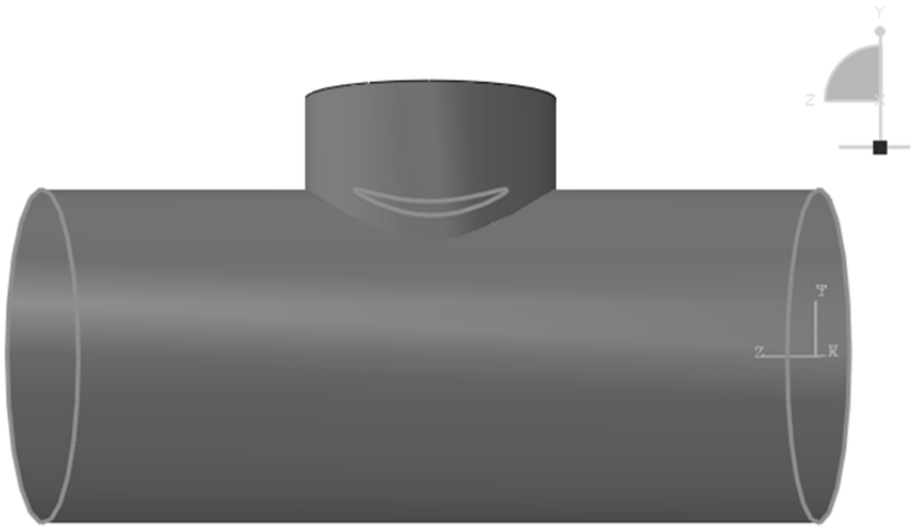

Figure 73 - Cutting a Hole in a Cylinder ABAQUS Model

Adding a hole produced a sizeable reduction in capacity (for the bleeder carbon: 27.9kip, a reduction of 41%) results for all three models with holes are in Table 31. The buckling mode changed from the sine wave shapes typical for a perfect cylinder to a concentrated deformation around the hole. The deformed shape was not consistent with the experiment as the model predicted large creases in the cylinder face, Figure 74, and experimental testing, Figure 76, showed creases at the sides of the cylinder with the top and the bottom face of the cylinder rotating towards the center.

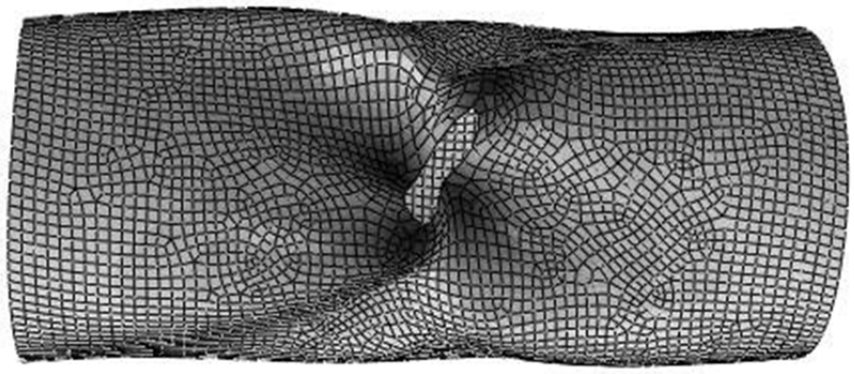

Figure 74 - Bleeder Carbon Buckled Shape Without Reduced Stiffness

Models With Damage Around Hole

When a hole is cut into a composite the tows cut by the hole become discontinuous and lose stiffness until developed by the matrix and the surrounding tows. Further, holes were cut with a hole saw, the same device used for cutting filling holes for concrete filling, which damages the surrounding matrix. The initial model with the hole ignored stiffness loss of the composite around the hole caused by inadequate development length and a damaged composite. A simplified approach was used to generate new material properties for a region immediately surrounding the hole of a certain width. This area had a 50% modulus reduction (E_x, E_θ, and G_{xy}) to reflect a linear change in modulus from the damaged edge (0 stiffness) to the full moduli in the body of the tube. At the damaged edge, the moduli will not be zero; the matrix will retain some of its stiffness. All properties are reduced evenly, although the shear modulus and off-axis modulus will develop more rapidly than the fiber direction modulus because they are more dependent on matrix properties. The radial and longitudinal moduli are a combination of all material direction moduli. The fiber direction modulus is much higher than the off-axis modulus, a uniform reduction was taken for all properties. The width of the surrounding area, from the physical hole to the edge of the reduced property region, was chosen to force the model to produce the experimental average buckling load, as shown in Table 31

Table 31 Length Convergence for Reduced Stiffness Area

Soft Region Width	BC Small	DC Small	DC Large
Experimental	48.9	74.3	47.6
No Reduced Stiffness	124	207	70.2
0.50in	69.4	116	58.5
0.94in	-	-	**47.5**
1.00in	57.6	95.3	46.2
1.5in	50.5	82.5	-
1.70in	**48.8**	-	-
1.85in	47.7	77.5	-
2.20in	46	**74.7**	-

The width of the damaged region was also compared with the equation for shear lag of a tow in resin, the development length of a tow in neat resin, where V is volume fraction, η is the length modification factor (Equation 22
), l is the tow length, r_f is fiber radius, and all other values are shear and longitudinal moduli for the fibers f or the matrix m (Nairn, 1997). When the equation reaches 90% of the fiber modulus, as given by Equation 23
, the fiber is considered fully developed. For the carbon development occurs at 0.91in, 0.984in for the glass. These values compare reasonably with the optimal lengths of the damaged region of 0.94in to 2.20in reported in Table 31.

$$\eta = \left(\sqrt{\left(\frac{2}{{r_f}^2 E_{af} E_{am}} \right) \left[\frac{E_{af} V_f + E_{am} V_m}{\frac{V_m}{4G_{af}} + \frac{1}{2G_{am}} \left(\left(\ln\left(\frac{1}{V_1} \right) - 1 - \frac{V_m}{2} \right) / V_m \right)} \right]} \right) \qquad \text{Equation 22}$$

$$E_f = E_{af} \frac{2(1 - \tanh(l\eta))}{l\eta} \qquad \text{Equation 23}$$

To assign material properties around the hole, a larger hole had to be modeled into the composite using the same method as for the smaller hole. The Area between the larger hole and the smaller hole were then joined to form a new section in the part using the merge command in the ABAQUS assembly module. The new reduced region, when meshed, appears in Figure 75. Because the tube section with a portion removed and the

ring were stored as separate regions with different properties in the same part, no tie constraints or contact were needed for this analysis.

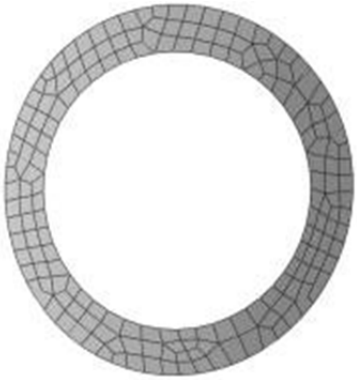

Figure 75 - Meshed Reduced Area Around Hole

The new model produced a lower capacity than the previous model without the reduced ring around the hole. The buckled shape alters substantially. Figure 76 shows the buckled shape and the predicted buckling shape. In both cases the area above the hole rotates inward and the material on the edges of the hole, near the mid height of the hole, buckles outward and undergoes the maximum deformation.

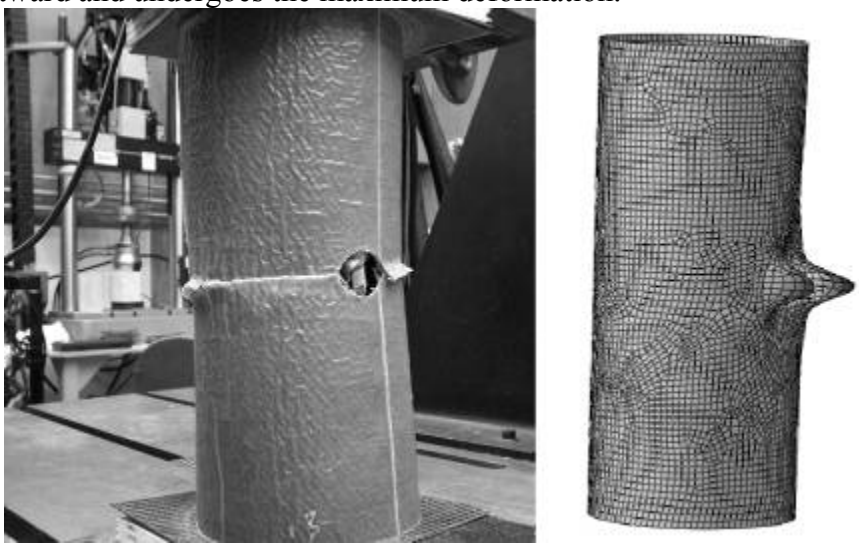

Figure 76 - Comparison of Model to Actual Buckled Shape

Imperfections in Tubes With Holes

Tubes with holes were just as likely to have unbalanced loading and irregular geometries as specimens without holes. Unlike solid specimens the hole was a local weak spot and

the direction of curvature or uneven loading affects the load path relative to the hole, affecting the buckling capacity. As seen in the previous sections, the hole is a severe weakness in the model and specimen and it was important to determine whether other geometric imperfections played a significant role in buckling capacity.

Effect of Unbalanced Loading in Tubes with Holes

Six models were run for each material type for an unbalanced loading case, and the results of the analysis are summarized in Table 32. The unbalanced load varied linearly based on angular location. These models put the peak load directly over the hole, diametrically against the hole, and at a 90-degree angle from the hole. Loads applied to the top and bottom surface of the tube were equal and opposite and always applied in the plane of the cylinder wall. Applying the maximum load above the position of the hole caused a dramatic loss in capacity similar to that seen in the low outliers of the experimental results for the carbon bleeder specimens with holes. Plywood end caps crushed (from experimental observation) near 6.74kip; any specimen that failed at or below 6.74kip did not have an opportunity to damage the plate and redistribute the load. Both the bleeder carbon with a small hole and the double carbon with the large hole were, according to the model, capable of failing under a lopsided load prior to plywood cap failure. Figure 77 shows the effect on buckled shape of moving the concentrated load to different faces of the cylinder.

Table 32 Capacity of Models With Holes and Unbalanced Loads in kips

TYPE	DC small	BC small	DC large
Even Load	16.8	11.0	10.7
Partial Unbalance Over the Hole	12.7	9.67	8.30
Partial Unbalance Off the Hole	24.5	16.9	13.9
Partial Unbalance Side of Hole	17.7	12.1	10.1
Full Unbalance Over the Hole	10.1	6.77	5.89
Full Unbalance Off the Hole	42.0	27.0	33.7
Full Unbalance Side of Hole	16.6	11.4	9.22

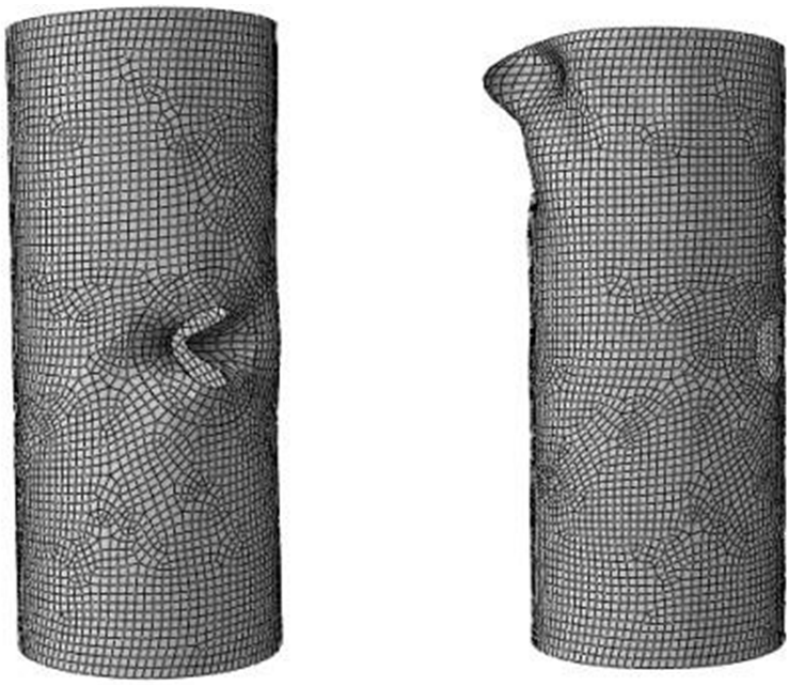

Figure 77 - Small Hole Double Carbon Model with Different Load Locations

Effect of Geometric Imperfections in Tubes With Holes

The models with holes were perturbed into the same geometric irregularities as the cylinder models without holes. Asymmetric model variations (ellipse, single curvature, double curvature, and arc) depend on the relative position of the hole to the geometry of the cylinder. Single curvature and arc models have a front, rear, and side model and the double curvature and ellipse each have a front and side model (the front and rear are symmetric for these models). In general, deformities were less important for buckled shape or failure load in models with holes because the hole was the dominant failure for most models. Asymmetric models that either concentrated or dispersed the load in the region around the hole had an effect, but the percent change was generally larger for the cylinder without holes than the holed cylinder when deformed. Table 33 contains the capacity of all tested geometric imperfections.

The hourglass, bulge, double curvature, minor axis ellipse, and single curvature 90 degrees from hole all have negligible reductions versus the perfect cylinder – less than 5% increase or decrease even with large perturbations. The major axis ellipse produced a sizeable decrease with a large change in radius, but based on experimental testing discussed in Bend Testing of Hollow FRP Tubes, it seems unlikely that this level of ellipticity will ever be reached during filling. Single curvature and arc curvature can

produce significant changes in the capacity of the cylinder. With a hole on the outward curving face of the single curvature shape the capacity increased because the load path moved away from the defect. With the hole on the inward curving face capacity is reduced. This phenomenon was similar to the uneven loading case, only the results were less severe. The arc shape produces significantly lower results whether the hole was located on the front, rear or side of curve – not the anticipated result. All material models shared this result suggesting that the hole adversely affected the capacity of the arched shell. The small reduction for most defects explains the low COVs from the experimental loads (8.1% bleeder carbon, 5.7% small hole, and 7.5% big hole double carbon).

Table 33 Failure Load in kips of Models with Hole and Geometric Imperfection

Type	DC small	BC small	DC large
Experimental	16.8	11.0	10.7
Non-Deformed	16.8	11.0	10.8
Hourglass - 0.02in	16.8	11.1	11.0
Hourglass – 0.06in	16.8	11.2	11.2
Hourglass - 0.10in	16.8	10.9	10.6
Bulge - 0.02in	16.7	10.8	10.4
Bulge - 0.06in	16.6	10.7	10.2
Bulge - 0.10in	16.8	11.0	10.7
Single Curvature Front - 0.10in	16.9	11.2	10.8
Single Curvature Front - 0.06in	17.6	11.8	11.2
Single Curvature Front - 0.50in	17.5	11.4	10.7
Single Curvature Back - 0.10in	18.8	12.0	10.9
Single Curvature Back - 0.06in	19.9	12.7	11.3
Single Curvature Back - 0.50in	16.0	10.5	10.4
Single Curvature Side - 0.10in	14.5	9.49	9.76
Single Curvature Side - 0.06in	12.9	8.43	9.01
Single Curvature Side - 0.50in	16.8	11.0	10.7
Double Curvature Front - 0.10in	16.6	10.9	10.7
Double Curvature Front - 0.06in	16.5	10.7	10.6
Double Curvature Front - 0.50in	16.8	11.0	10.7
Double Curvature Side - 0.10in	16.7	10.9	10.7
Double Curvature Side - 0.06in	16.7	10.7	10.8
Double Curvature Side - 0.50in	16.9	11.0	10.4
Ellipse Major - 0.10in	17.0	11.0	9.82
Ellipse Major - 0.06in	16.9	10.9	9.06
Ellipse Major - 0.50in	16.6	10.9	10.9
Ellipse Minor - 0.10in	16.2	10.7	11.1
Ellipse Minor - 0.06in	15.8	10.5	11.3
Ellipse Minor - 0.50in	15.9	10.7	9.42
Arc Side - 0.10in	16.3	11.0	9.73
Arc Side - 0.06in	17.1	11.7	9.98
Arc Side - 0.50in	15.3	10.2	9.24
Arc Front - 0.10in	14.1	9.42	9.40
Arc Front - 0.06in	13.0	8.61	9.85
Arc Front - 0.50in	16.5	10.9	9.28
Arc Back - 0.10in	17.6	11.5	9.47
Arc Back - 0.06in	18.5	12.0	9.91

Arc Back - 0.50in	16.8	11.0	10.7

Case Study, Caribou, Maine Bridge

A bridge planned for construction during summer, 2011 in Caribou, Maine is being built with a longer span and larger span to depth ratio than previous bridges, meaning that moments would potentially be higher than previous bridges and this bridge would be closer to critical load during filling. This chapter contains the modified finite element shell model for the new shell lay-up. In this circumstance the model was predictive; no testing was performed on this geometry and fiber construction.

Model Input Parameters

The shell for this model is identical to the Belfast Bridge that is described in Walton (2011); material properties use a 1-layer per braid model, adhering to principals from Lamina with One Orthotropic Layer per Braid. Material properties for the 14.76in diameter Caribou model are in Table 34. The cylinder in the model had length 36.0in, larger than the 15.0in length used in previous modeling, to keep a consistent diameter to length ratio. Two models were constructed: one with a 2.50in hole, to compare with stress at the apex, and one without a hole to compare with stress at the footing (peak stress); no perturbations were applied to either model. In the model with hole a reduced property region was created around the hole. As with previous models, stiffness was reduced by 50% (E_x, E_y, G_{xy}) for a length of 1.10in in all directions. The same methods as described previously were used for connecting the reduced properties section with the solid cylinder. The model was meshed with larger elements than previous, 0.512in per side, keeping approximately the same number of total elements in the model.

Table 34 Caribou Bridge Material Input Parameters

Property	**Carbon**	**E-Glass**
Angle (Degrees)	16	76
Thickness (in)	.039	.038
E_1 (Ksi)	8990	1200
E_2 (Ksi)	1000	4150
ν_{12}	0.977	0.139
G_{12} (Ksi)	1090	631

Model Results

Buckling capacity for the two models are displayed in Table 35 results are given in stress (ksi), instead of force (kips), the reported quantity for all previous buckling models. For pure axial loads, stress is constant in the cross section, for combined bending moment and axial load the stress varies in the cross section and the peak stress (combined) from the load model is compared to the model buckling stress (axial). Model results indicate a large reduction in buckling capacity when the hole is included, as seen in previous models. As the hole implemented in this arch is smaller, relative to length and diameter, to previous holes, the reduction in capacity is not as dramatic as that for previous holes. The model results are presented directly from ABAQUS, without any additional reduction. For previous results the double carbon experimental buckling average was 45% of the ABAQUS model prediction, so confidence on the accuracy of the model without holes is low. Applying large perturbations to the model is one potential approach toward getting a more accurate model. Figure 78 and Figure 79 show the lowest eigenvalue buckled shape for the models. The model without a hole is very different from previous buckling modes; shape change is localized to the central portion of the cylinder instead of the more uniform buckling mode of smaller diameter models.

Table 35 Caribou Bridge, Model Predicted Buckling Stress

	No Hole	**With Hole**
Model Buckling Stress (Ksi)	16.7	7.40

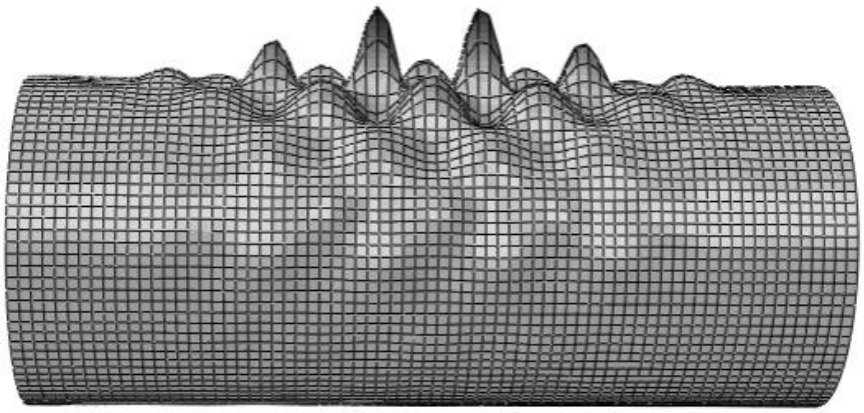

Figure 78 - Caribou Cylinder Without Hole

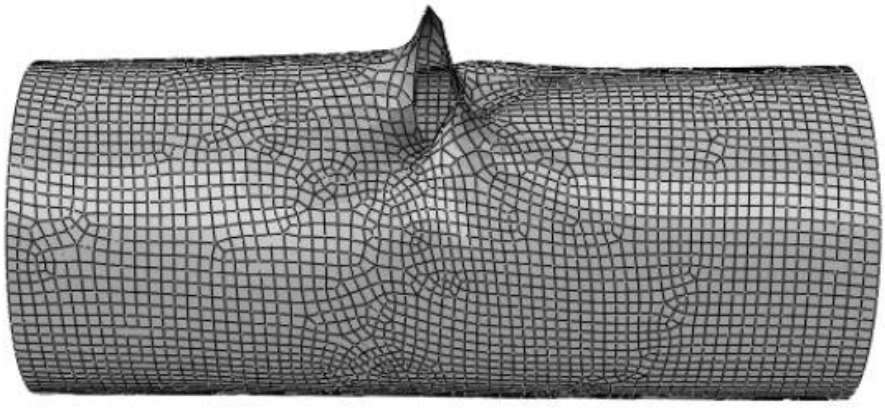

Figure 79 - Caribou Cylinder With Hole

Conclusion

Finite element shell models were used to perform eigenvalue buckling analyses and estimate the buckling capacity of short axial compression cylinders. The models were created to reflect actual test specimens and determine what factors influenced the buckled shape and buckling load. Several element types and material idealizations were considered, and mesh refinement was also addressed. In general, model-predicted buckling loads were higher than experimental buckling loads, and unbalanced loading and geometric defects were implemented to reduce capacity and more accurately compare to tests.

Of the geometric defects considered, only the extreme arc and single curvature defects were able to reduce the load from the perfect model to the experimental buckling load. Most specimens were closer to the perfect model, yet they still failed at a reduced load. Only cylinder global defects were considered; local fiber inconsistencies including tow size and tow overlap were ignored. These micro defects, in conjunction with a combination of the less extreme diameter and curvature defects likely account for the variability in the experimental load and the difference between the experimental load and the theoretical load.

Models with holes predicted buckling at loads close to experimental buckling loads for specimens with holes. Models with holes were minimally affected by diameter defects, indicating that the presence of the hole dominated response, and local geometric defects were unlikely to reduce buckling capacity further. The only defects that affected the capacity of models with holes were ones that rapidly changed the curvature near mid height – the single curvature and arc models. By extension, local defects including tow thickness and stiffness are expected to minimally affect the capacity of models/specimens

with holes. The hole was the dominant defect and unless the model/specimen was unevenly loaded or curved, there is expected to be good agreement between the model-predicted and experimentally measured buckling loads.

BEND TESTING OF HOLLOW FRP TUBES

Concrete filled FRP arches are designed as cast in place members where the FRP skin serves as the formwork for the curing concrete and the tensile reinforcing for the completed arch. When the concrete is first pumped into the arch it is a fluid, meaning that it contributes no strength or stiffness to the arch while it adds self-weight. The FRP arches made at the AWEC have a short height versus span and are formed around a circular section; this results in combined axial compression and bending. The FRP skin of the arch must carry this bending and axial compression load alone. Even if temporary shoring can be installed to support the arch during filling, it could cause large concentrated loads on the arch shell, which could lead to premature failure due to the low stiffness of the hollow FRP shell when loaded in the direction of cross-sectional radius.

When a hollow shape is subjected to a bending moment, there is a distortional effect caused by bending stress and curvature that alters the cross sectional shape. For a circular cross section the distorted shape can be approximated by an ellipse, where the radius perpendicular to the axis of bending decreases. This reduces the section modulus (bending resistance) and buckling capacity (see Modeling Buckling for a Hollow Cylinder, shell element modeling of cylinders) for an actual beam or arch. This phenomenon was first analyzed by Brazier (1927) and is sometimes referred to as Brazier's effect. Brazier used many simplifications and ignored higher order terms in approximating values, but later research (Kedward, 1978 and Tatting, 1997) has shown that Brazier's approximations for bending moment and radius change were reasonably accurate. Brazier (1927) and Tatting (1997) both noted that local buckling modes exist that are driven by geometry and stiffness and can result in beams failing in bifurcation buckling prior to the reaching the maximum bending moment and maximum radius reduction of 22% proposed by Brazier. Prior research assumes a geometrically perfect beam and isotropic (Brazier) or orthotropic (Kedward and Tatting) material, and deviation from these properties can reduce the collapse moment, giving smaller radius change at failure.

The two goals of the testing reported in this chapter were to find the failure stress of a hollow FRP shell in bending and to find how much cross sectional distortion occurred before failure. To avoid point source loading and mimic the effect of wet concrete, fluid (water) was used as a loading source. In some tests, bending stiffness was measured by applying a known weight near mid span and measuring mid span deflections.

Specimen Fabrication and Material Properties for Bending

Fluid filled bend tests occurred in October 2009 and June 2010. Each test used tubes composed of different material properties and having different geometries. For clarification the three tested glass tubes will be referred to as tubes G1, G2, G3 while the

six tested carbon fiber tubes will be referred to as tubes C1 – C6. Carbon fiber specimens that did not fail during testing were tested a second time after being rotated 90 degrees to get additional results from the same number of specimens; tests are labeled 'top' or 't' for the initial orientation and 'side' or 's' for the alternate orientation. The basic characteristics of the specimens are summarized in Table 36. Specimens built for testing in October were 11.8in diameter glass tubes with length 358.27in to 366.14in. Tubes were constructed of a diameter constraint e-glass (+/- 81 degrees, 0.043in) and a structural longitudinal e-glass (+/-30 degrees, 0.016in), and all three tubes were nominally identical although tube G1 was subject to incomplete vacuum after infusion making one side resin rich and the other side resin poor. Specimens for testing in June 2010 were 6.50in diameter carbon tubes with lengths of 433.04in to 472.44in. The fiber architecture (fiber angle, infused thickness) was diameter constraint e-glass (+/-81 degrees, 0.035in), one (tubes C1-C4) or two (tube C6) layers of structural carbon fiber (+/-22 degrees, 0.027in per layer), and for specimen C5, one layer of structural carbon fiber (+/-22 degrees, 0.027in) and a 0.032in thick homogenous polyester mat outer bleeder layer. Specimen and layer thicknesses were measured after undamaged sections of the tubes were cut for compression testing.

Table 36 Bend Testing Matrix

Diameter	Single Carbon	Double Carbon	Carbon Bleeder	Outer Glass
6.50in	C1-C4	C6	C5	0
11.8in	0	0	0	G1-G3

Tubes C2-C6 were loaded with a single 51lb sand bag to produce a local distributed load centered at 12.0in from mid span (while the mid span deflection was being measured) to find the bending stiffness *EI*. Table 37 contains the measured bending stiffness and the theoretical bending stiffness for the carbon fiber tubes. Theoretical bending stiffness was based on Classical Lamination Theory (CLT) and micromechanics properties for the carbon fibers, glass fibers, polyester mat fibers, and vinyl ester matrix, see Material Assumptions for material model assumptions.

Table 37 Elastic Modulus from Sand Tests

	SC	BC	DC
Experimental E_x (Ksi)	5920	4210	8500
COV (%)	5.43	5.77	3.03
Predicted E_x (Ksi)	5740	4080	7180
Percent Difference	3.00	3.17	15.49

Test Setup

Water fill testing was performed outside to avoid water spills indoors after tube failure. shows the test setup used for the 6.50in diameter specimens (the setup for 11.8in specimens was similar). Reinforced concrete supports, 29.9in cubes, were positioned 359.84in on center on level asphalt or on concrete blocks such that the center of both supports had the same elevation. The concrete cube was topped by a rocker platform restrained to allow only in-plane rotation and hardwood saddles to prevent the tube from displacing in any direction, as in Figure 81. Beams were simply supported. The larger diameter tubes sat snugly in the saddles while the smaller diameter tubes were strapped into the saddles with neoprene padding because the same saddles were used for both tube diameters. To prevent water from spilling out of the ends of the tubes inflatable rubber plugs were tightened into position over the supports for all tubes during testing. Wooden stands straddled the tube at five evenly spaced intermediary points along the length of the tube to hold instrumentation.

Figure 80 - Test Setup for 6.50in Diameter Specimens

The water fill rate was assumed to be constant for the duration of a single test. For the 11.8in diameter tests the fill time for a bucket (45.19lb capacity) was measured three times, twice prior to test, and once after test, to establish a flow rate. Flow rate varied by less than 1 second for all tests on a 11.8in tube corresponding to COVs <1%. Tube G3 – tested on a different day than tubes G1 and G2 – had a statistically significant difference in fill time, and a different fill time was used. For the 6.50in diameter specimen tests a constant head water tower, Figure 82, was erected to give a constant flow rate. The flow rate was measured by weighing buckets after a 1 minute, in total 12 buckets were weighed on three different days. Table 38 contains the load rate Q for each cylinder in N/min.

Table 38 Load Rate for Fluid Filled Specimens

TUBES	**11.8in 1 and 2**	**11.8in 3**	**4.92in All**
Rate (lb/min)	50.1	47.7	28.1
COV (%)	0.50	0.43	0.87

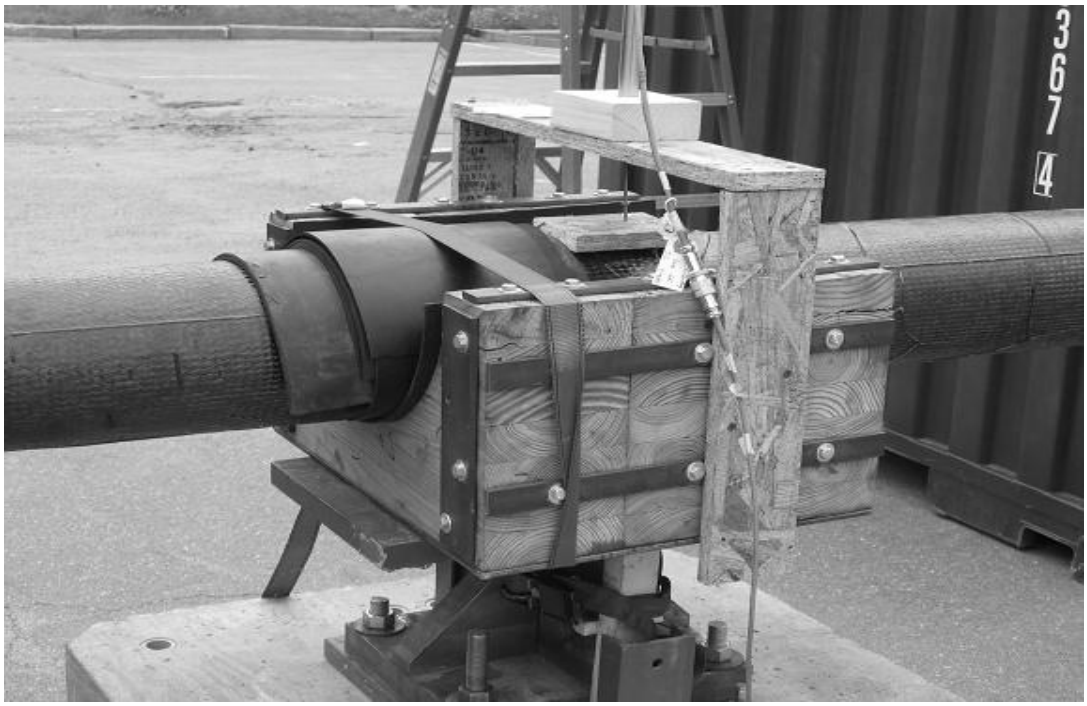

Figure 81 - Detail of Support from 6.50in Diameter Testing

AEWC Advanced Structures & Composites Center
5793 AEWC Bldg
University of Maine
Orono, ME 04469-5793

Telephone: 207-581-2123
FAX: 207-581-2074
contactaewc@umit.maine.edu
www.aewc.umaine.edu

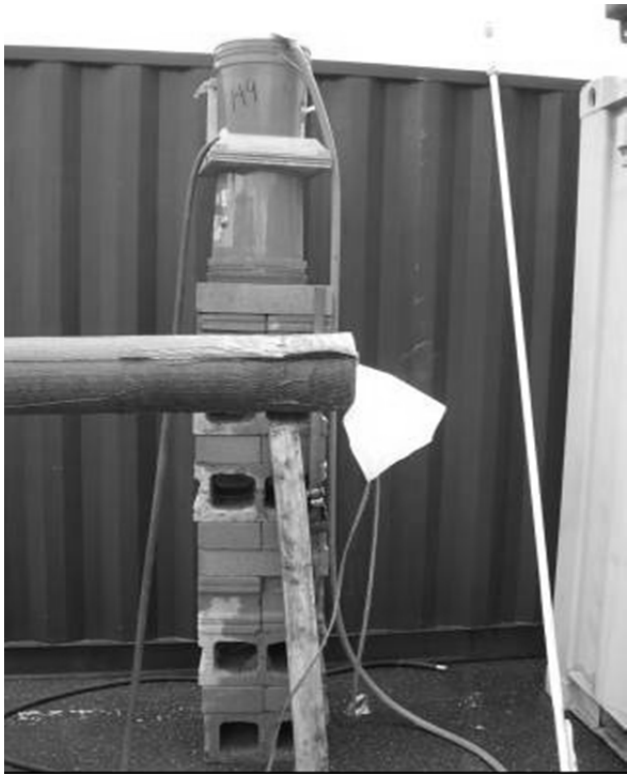

Figure 82 - Constant Head Water Tower

Instrumentation

The ovalization at a point on the tube (near midpoint) and the vertical displacement at several points along the span were measured during testing. Improvements were made to the instrumentation configuration as testing progressed. The same instrumentation was not used in every test, but for all tests the string potentiometer (string pot) configuration was similar, and 8 string pots were used. Four string pots were positioned at mid span to triangulate horizontal and vertical displacement. The other four string pots were positioned, one apiece, at the other sixth points along the specimen and positioned vertically above the starting point of the cylinder where they were connected to wooden frames. The strings were lengthened by monofilament fishing line to allow additional space between the instrument stand and the specimen and provide a mechanical fuse between the string pot and the specimen. String pots spanned from the wooden supports to screws that were fastened into small wooden blocks glued on the specimen using cyanoacrylate (super glue) and hot glue. Cyanoacrylate provided a rigid connection that did not displace during testing; hot glue provided a rapid bond until the cyanoacrylate hardened.

Two modifications were made to string pot configuration between the different test periods: the gap between the specimen and the instrument stands was increased from ~9.84in to ~25.6in to reduce the effect of non-vertical displacements on string pot displacement, and the string pots at mid span were moved to get an angle further from 90 degrees (see Figure 83) to improve calculation accuracy. The side string pot in the early configuration would produce incorrect measurements as the tube displaced past the string pot. Mid span string pots were positioned to be coplanar over the connection point so that displacement in the Z and Y direction could be calculated through trigonometry.

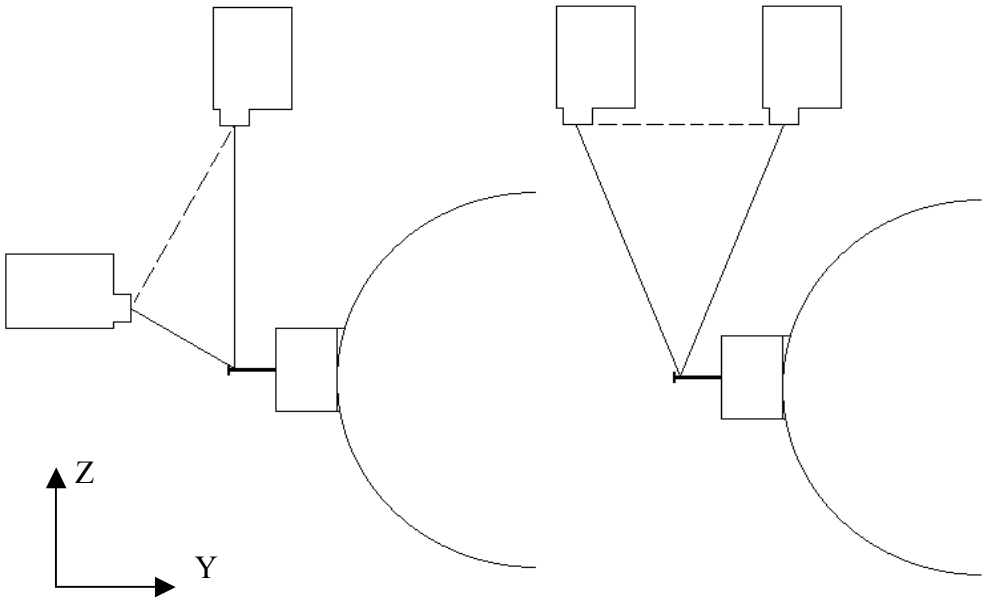

Figure 83 - Mid Span String Pot Arrangement Original and Improved

The 6.50in specimens had five additional linear variable differential transformers (LVDTs) added to measure support displacement, direct ovalization (vertical diameter loss) and mid span deflection. At supports, +/-0.984in LVDTs measured the amount the maple saddle and underlying neoprene crushed (see Figure 81), which was typically small compared to bending deflections in the span of the beam. A wooden yoke carrying a +/-0.984in LVDT was mounted to the specimen with duct tape to directly measure vertical diameter change of the specimen (Figure 84). Two long stroke (+/-5.0in) LVDTs measured vertical displacement at mid span as a check against triangulated string pot displacements and for measuring mid point deflection in point load tests (for bending stiffness *EI*).

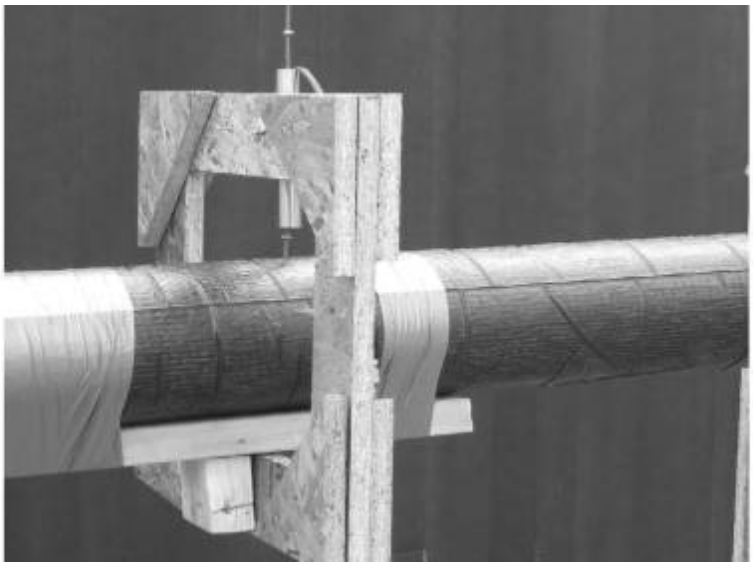

Figure 84 - LVDT Yoke for Measuring Ovalization

Results

The 11.8in diameter glass fiber specimens were loaded to failure, whereas the 6.50in diameter carbon fiber specimens were not intended to fail during testing, only ovalize. However, two carbon fiber (single carbon) specimens failed during testing. For the glass fiber specimens all three samples failed in local buckling at or near mid span (within 29.9in) and specimens G2 and G3 failed in the anticipated collapse of the compression face. Visual inspection of the tubes after failure shows that the tension face did not fracture or show signs of matrix damage even during the collapse for tube G2 and G3. Tube G1 had manufacturing defects, half of the cross section was resin poor, the other half was resin rich. The tube was arranged with the neither the center of the resin rich or resin poor sides on the compression face. Failure was asymmetric; the resin poor portion of the compression face collapsed before the resin rich portion. The resulting load redistribution caused buckling on the bottom of the tube in the resin poor portion of the face.

The carbon fiber specimens failed further from mid span with tube C1 failing outside of the middle third by ~11.8in (west) and tube 2C failing ~31.5in (east) from mid span. Both failures occurred when the specimen was nearly full and near the peak stress, as seen in later sections.

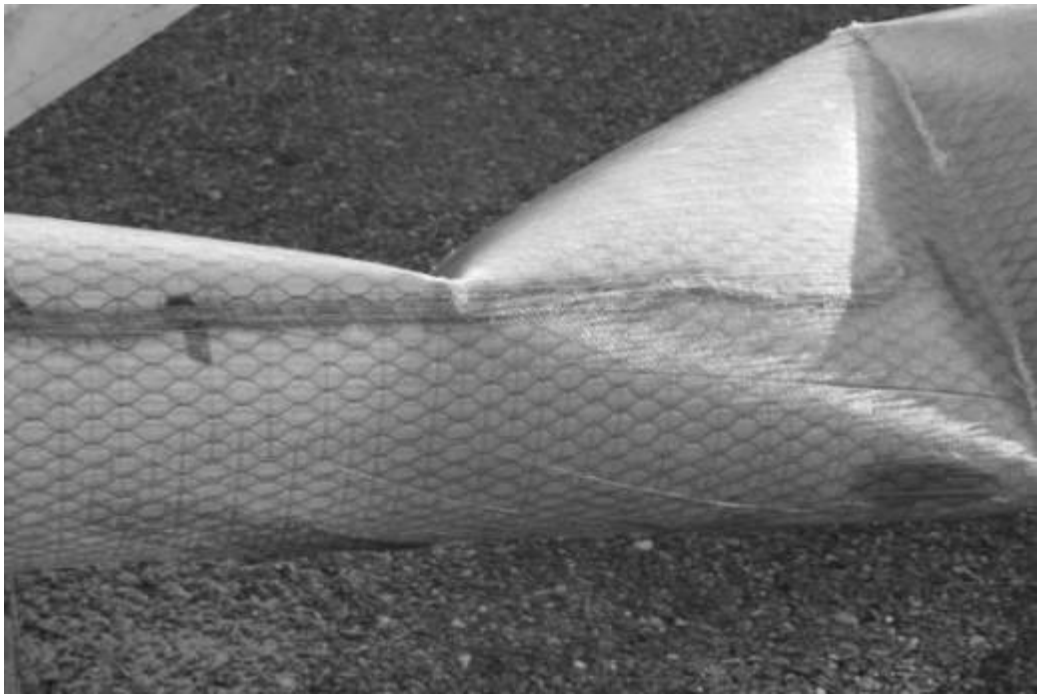

Figure 85 - Tube G1 Asymmetric Local Buckling of the Compression Face

AEWC Advanced Structures & Composites Center
5793 AEWC Bldg
University of Maine
Orono, ME 04469-5793

Telephone: 207-581-2123
FAX: 207-581-2074
contactaewc@umit.maine.edu
www.aewc.umaine.edu

Figure 86 - Tube G3 Symmetric Local Buckling of the Compression Face

Analysis Procedure

Strain gauges were not applied to the tubes, and no direct measurement was taken of the strain within each specimen. To calculate stress in a specimen a MATLAB program was written that used the deflection and vertical radius decrease as inputs and used the flow rate from the given test to compute the fluid loads along the length based on actual and interpolated deflections and pooled fluid weight. Ponding was a significant phenomenon in these tests; often the center deflection of the 6.50in diameter specimens exceeded 6.50in during filling, making it possible for the center to be fully filled while the sides were effectively empty. In this analysis, the water was treated as a non-viscous fluid and for calculation purposes it was assumed that the water instantly flowed to an even elevation across the entirety of the specimen. The density of water was taken as $0.036 lb/in^3$ in all calculations.

Deflection and Diameter Measurement

During the test, deflection was measured at five evenly spaced 5.0ft intervals along the length of the 30ft-span. Only gravity loads (self weight and water) were applied to the specimen during testing; it was assumed that the beam did not shift position along its length. With this assumption, the string pots only moved out-of-plane (*Y*) and vertically (*Z*). For string pots away from mid span all deflection was assumed to come from vertical displacement. This assumption was truer for the later specimens with longer initial string extensions (a 9.84in string with an extreme 1.97in out of plane motion gives a 0.20in error in deflection, a 25.6in string with the same 1.97in out of plane motion gives a 0.079in error). The endpoints were fixed against vertical deflection and the supports were rigid (there was a .118in piece of neoprene in the saddle support but its change in thickness was considered negligible for testing 11.8in specimens, and the total thickness change at the support was found to be less than or equal to 0.034in when measured during subsequent testing). Data for a specific time was not taken from a single time step but was taken as the average of (11) 1-second intervals immediately surrounding the time to account for instrumentation fluctuation.

Instead of using a single string pot at mid span, 4 string pots were used at mid span to capture the horizontal radius growth of the cross section. Two string pots connected to each side of the tube measured the change in length of two legs of a triangle; the third leg is the fixed distance between gauges. An out of plane (*Y*) and vertical (*Z*) deflection at each side of mid span was calculated. The difference in x-position on each side of the tube was taken as the horizontal radius growth. This measurement technique was sensitive to error and ultimately results of the horizontal radius measurement were deemed inaccurate due to the possibility of tube torsion, irregular cross sectional warping, and longitudinal shift that, while small, obfuscated the small horizontal radius change. Attempts to improve the method such as moving the gauges to a better initial angle near 60 degrees instead of an angle near 90 degrees did not substantially improve the quality of the data. A more successful technique was direct measurement of the vertical radius change by an LVDT on a yoke. This method produced more accurate results that, due to instrumentation faults, were not available on every 6.50in diameter test (including the failure of Specimen 1). The yoke was not used on any 11.8in diameter tests.

The MATLAB function interp1 was used with a cubic-spline shape to interpolate deflections using measured values. Figure 87 is a sample graph of the interpolated shape at 120second time intervals (and immediately before failure). The measured points are at 0ft, 5.0ft, 10.0ft, 15.0ft, 20.0ft, 25.0ft, and 30.0ft.

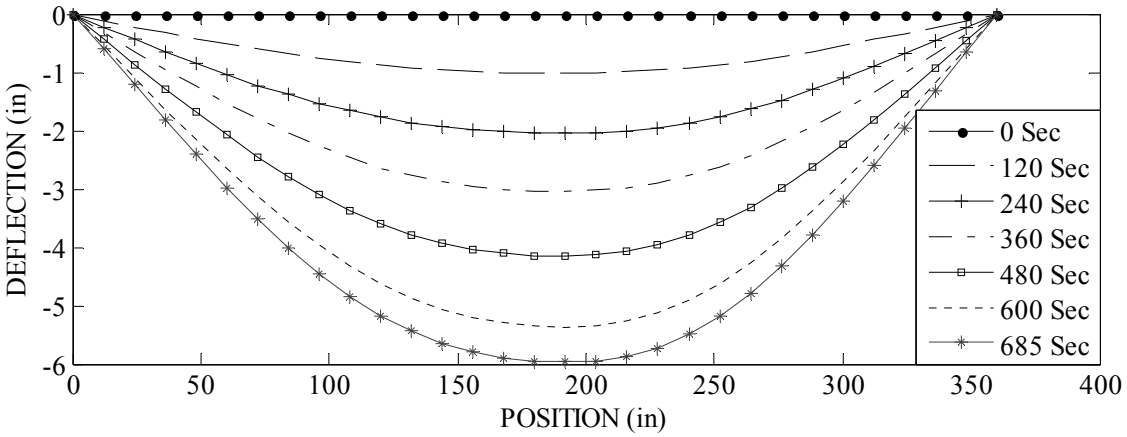

Figure 87 - Tube 2 Deflection versus Length at 120 Second Intervals

Ovalization

Determining cross sectional distortion at failure and during the test as a function of bending stress were the main reasons for fluid fill testing. Also of interest was the significance of cross sectional shape change on the section modulus and allowable stress (see modeling of compression testing). Under bending stresses the cross sectional shape of a tube or arch will change based on the curvature and the bending stress; this phenomenon is known as ovalization. The mechanism for ovalization is the bending stress acting through the curvature of the beam, as seen in Figure 88 (Tatting, 1998).

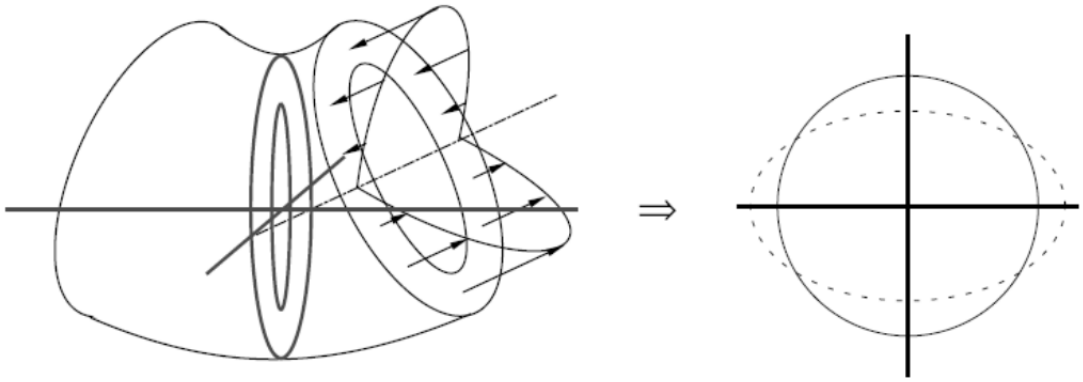

Figure 88 - Bending Stress Acting Through Deformed Tube from Tatting, 1998

Brazier (1927) was an early researcher to observe and calculate ovalization. Simplifications were used in his formulation, and all terms above second order were

excluded, i.e. the change in shape was only considered once while calculating stress, it was not recalculated to account for higher stress of the deformed shape. However, later research has shown that including the next higher order term will give a less correct answer, and only a full numerical computer analysis gives a better answer than Brazier's original hand calculations (Calladine, 1983).

Brazier derived an equation that relates bending curvature to both radius change w and angular position change s, where κ is curvature; v is Poisson's ratio (Brazier assumed an orthotropic material with the same Poisson's ratio in each direction); t is shell thickness; r is shell radius; and θ is angle (counter clockwise with 0 at the vertical axis). The vertical axis loss is calculated when $\theta = 0$.

$$w = \frac{\kappa^2 r^5}{t^2}\left(1-\nu^2\right)\cos(2\theta) + \kappa \nu r^2 \cos(\theta)$$ Equation 24

$$s = \frac{\kappa^2 r^5}{2t^2}\left(1-\nu^2\right)\sin(2\theta)$$ Equation 25

In Figure 89, the Brazier shape with a 22% loss in vertical radius, which is Brazier's radius change at collapse, is plotted with an equivalent vertical radius ellipse and an undeformed circle. Brazier's shape and the ellipse are clearly very similar, and the ellipse will be used for all subsequent calculations due to the relatively simple formulae for perimeter, partial area, and section modulus of an ellipse.

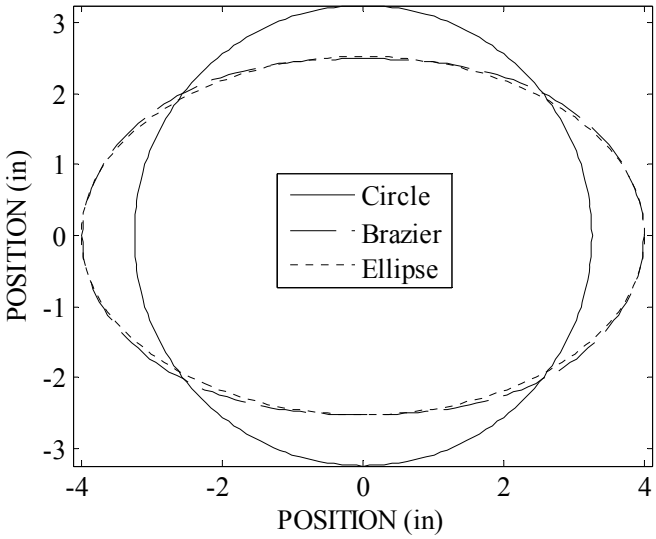

Figure 89 - Comparison of Cross Sectional Shapes

A second observation of Brazier, confirmed by later research (Tatting 1998), was that his theory predicts a theoretical ovalization limit with 22% loss of vertical radius, but local buckling can occur sooner depending on geometry and stiffness. The 22% loss in vertical radius is known as the 'collapse ovalization' and it corresponds to the point where the moment is non recoverable and increased curvature corresponds to a loss in moment capacity because of the diminishing cross sectional properties. Experimental tubes are prone to failing before this point in a lobed failure, where the cross section develops sinusoidal irregularities – as shown in the ABAQUS buckling models (see Modeling Buckling for a Hollow Cylinder). Tubes that are slender or stiffer in the longitudinal direction than the radial direction, or contain material defects, are more likely to fail prior to reaching the 'full' capacity (Tatting, 1998). Both pure compression and compressive bending stresses can produce local compressive buckling of a face on the cylinder, so the failure mode and compressive stresses at failure are assumed to be similar (Siede and Wiengarten, 1961, Tatting, 1998).

A more recent model accounts for orthotropic properties and composite laminate stacking sequence (Tatting, 1998), but this model assumes a symmetric laminate so it does not exactly satisfy the properties of the experimental specimens. Tatting based his analytical model on Brazier's model, following all assumptions used originally by Brazier. As a result, the cross section shape change predict by Tatting is identical to Brazier's, except it occurs at different stresses. Unlike the Brazier equation, the equation developed by Tatting also includes a collapse parameter dependent on a classical buckling model

(Donnell, 1935) and elastic shell theory (Sanders, 1950), allowing the cylinder to fail before the Brazier predicted ovalization maximum of 22%.

The collapse load for this material was established in Compression of Hollow FRP; the experimental collapse loads P_{cr} will be used as well as a predicted collapse load (per shell length) given by Equation 26 for all carbon specimens. No experimental compression load is available for glass only specimens. Internal pressure was low for the tube fill test; it is omitted from the following equations. Also required to calculate cross section loss is a collapse parameter χ, Equation 27, dependent on shell stiffness. This parameter allows for variation due to stacking sequence by using E_x, E_θ, and D_{11} and D_{22} from the composite compliance matrix. Normalized curvature c, Equation 28, is curvature scaled relative to the local buckling collapse load for a cylindrical shell; experimental values will be used in addition to model predictions. The collapse curvature c_{lt}, Equation 29, depends on the collapse parameter. Radius loss w, Equation 30, depends on the previously defined parameters.

$$P_{cr} = \frac{\sqrt{D_{11}E_\theta t}}{r}$$ Equation 26

$$\chi = \sqrt{\frac{D_{11}E_\theta}{D_{22}E_x}}$$ Equation 27

$$c = \frac{E_x t r \kappa}{P_{cr}}$$ Equation 28

$$c_{ltt} = \frac{1}{\chi}\sqrt{\frac{2}{3}}$$ Equation 29

$$w = \frac{\chi^2 c^2}{12}$$ Equation 30

A common assumption for treating ovalization phenomenon is a constant shell perimeter (Brazier, 1927, Kedward, 1978, Calladine, 1983, Tatting, 1998). The radial elastic modulus is several orders of magnitude higher than the transverse stiffness (i.e. only a small force is required in the direction of the cross-sectional radius to start flattening the hollow tube) for thin-walled sections (Brazier 1927, Tatting 1998). Also assumed was that all tubes were linear elastic until buckling. FRP composites typically exhibit linear

elastic behavior; the fibers are linear elastic until failure, fail before the polymer matrix, and have an elastic modulus greater than an order of magnitude higher than the matrix.

Table 39 contains the direct measured percentage ultimate vertical radius change and the indirect calculated vertical radius change based on the measured horizontal radius change found with triangulated string pots for all specimens tested. The values are given in bold type for specimens that failed during the test to differentiate from the specimens that were only tested to deflection.

Several specimens did not have measured radius changes either because of instrumentation failure or faulty measurement, most notably test C1-top, where because of a faulty LVDT and improper string pot configuration no accurate radius measurements were taken. Measured horizontal radius increase (from string pot triangulation) was typically much higher than the directly measured vertical radius decrease; this is inconsistent with the ellipse or Brazier shape change that suggests both axes should deform nearly equally. While there may have been differential shape change, it is more likely that one or both measurement systems had inherent flaws. The vertical radius change should have been more accurate for small radius changes as it was directly measured with the yoke on the carbon fiber tubes. In the case of large radius changes, which was more typical the glass tubes G1 – G3, the error in measurement becomes smaller relative to the actual quantity being measured and the horizontal radius change is more likely to be accurate.

Table 39 Maximum Percent Change in Vertical Radius from Bending Tests

Specimen	Indirect Radius	Direct Radius
G1	**25**	-
G2	**21.1**	-
G3	**20.2**	-
C1t	-	-
C2t	**6.6**	**3.29**
C3t	5.43	2.38
C3s	6.46	2.15
C4t	5.63	-
C4s	-	2.01
C5t	4.62	0.5
C5s	2.61	0.43
C6t	3.21	0.185
C6s	1.37	-

Perimeter

Measurements gave a single radial change, either vertical or horizontal. The second radius was calculated assuming a constant perimeter. Equation 31 shows the Ramanujan approximation for the perimeter of an ellipse (Sykora, 2010). This approximation is less computationally intensive than an integral and matches the Taylor series of the integral for the first 9 terms (Sykora, 2010). Known quantities A (known radius) and p (perimeter) allow for B – the other radius – to be found using Newton's method, an iterative approach where the difference between guesses is linear; the initial guess for B was the circular radius.

$$p = \pi(r_A + r_B)\left[1 + \frac{3\left(\frac{(r_A - r_B)^2}{(r_A + r_B)^2}\right)}{10 + \sqrt{4 - 3\left(\frac{(r_A - r_B)^2}{(r_A + r_B)^2}\right)}}\right]$$

Equation 31

Fluid Cross-Sectional Area

The cross sectional area of the fluid was calculated at each node in the tube for a specified time in the fill. The three additional assumptions to the interpolated displaced shape used in calculating the cross sectional area were: fluid settles to a level height (shown in Figure 90), flow rate was constant (volume of fluid depended on time), and a simplified method of determining the ovalization at discrete points could be used. The first two assumptions have already been discussed. The middle third of the tube has a moment within 20% of the maximum moment; therefore it is likely that for a uniform tube the ovalization is close to uniform over this region. Over the end thirds the moment diminishes rapidly to 0 at the pinned supports, and at the supports the cross sectional shape was fixed by pressurized plugs meaning that there is no ovalization at the support. An assumption was made that the radius change varies linearly from a circle at the supports to the radius change at the third point.

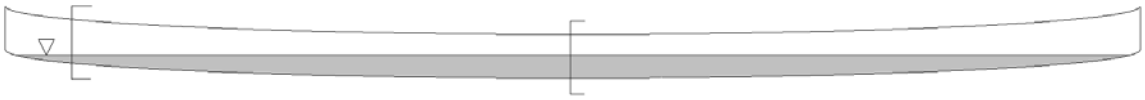

Figure 90 - Deflected Tube with Varying Water Height, Section in Figure 91

Because of uncertainty in ovalization measurements and calculations three cross sectional shapes were considered: a circle (original shape), the ellipse based on vertical radius change (direct measurement) or an ellipse based on horizontal radius change (triangulation). For the ellipses considered, there is small change in the area, but the partial filled area can have a larger change because of the shorter cross sectional height of an ellipse, as shown in Figure 91.

Figure 91 - Cross Section of Partially Filled Tube

The area was found at each node by solving the integral in Equation 32 for the partial area of an ellipse, A_p, where h is the depth, r is the circular radius, x is the variable of integration, and all other variables are the same as calculating the perimeter of an ellipse.

$$A_p = 2\frac{r_A}{r_B}\int_0^h \sqrt{2r_B x - x^2}\, d(x) \qquad \text{Equation 32}$$

When using the circular cross section assumption the two radii are equal and the equation simplifies to Equation 33, which can be represented without an integral.

$$A_p = 2\int_0^h \sqrt{2rx - x^2}\, d(x) = \frac{r^2}{2}\left[\pi + 2\arcsin\left(\frac{h}{r} - 1\right) + \left(\frac{h}{r} - 1\right)\sqrt{\frac{h^2}{r^2} - \frac{2h}{r}}\right] \qquad \text{Equation 33}$$

Conservation of Volume

At each node, tributary volume V_i, Equation 34, was calculated using partial filled area and tributary length L_i.

$$V_i = A_{p_i} L_i \qquad \text{Equation 34}$$

Density of the water does not appreciably change throughout the experiment and a constant delivery of water is assumed; there must be a constant increase in volume. The total fluid volume V_t, Equation 35, was known from the fluid load rate Q, the density of water ρ and the time duration t_{fill}.

$$V_t = \frac{Q}{\rho} t_{fill}$$ Equation 35

Using Newton's method, the depth of fluid in the tube D was manipulated until the sum of nodal volumes equaled the total volume V_t. To begin the iterative process for fluid depth an initial guess was needed to calculate nodal volumes, mid span deflection was chosen, meaning that the initial guess made the fluid height level with the elevation of the supports. A numerical derivative for the volume with respect to depth $d(V_i)/d(D)$, needed for Newton's method, was calculated using forward difference method and a small change in depth. Equation 36
shows the calculation of the updated depth D performed at each Newton iteration.

$$D = D - \frac{V_t - \sum V_i}{\frac{d(V_i)}{d(D)}}$$ Equation 36

The fluid area was recalculated for the updated depth. This process was iterated until the volume difference for the entire tube between the total volume and the summed nodal volumes was less than .000061in^3.

Point Forces
The force applied to the tube by water loading was treated a series of point loads applied at the nodes. Figure 92 shows a beam with the non-uniform distributed load of water weight divided into point loads. The magnitude of each nodal force was equal to the density of water times the volume of water in the space tributary, using the optimized volume from Newton's method at each node. The density of water was taken as 0.036lb/in^3.

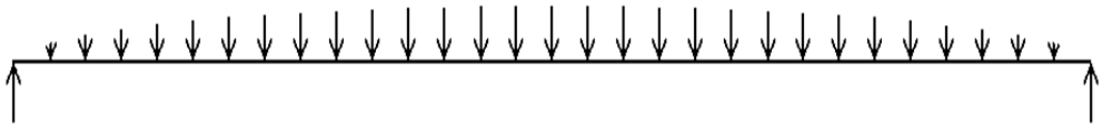

Figure 92 - Beam with Applied Fluid Load

Bending Stresses and Displacements

The right vertical reaction, R_{right}, was calculated by summing moments about the reaction assuming a simply-supported beam. In Equation 37, P is a point force caused by water weight; l is the distance from the left support to the point force; n is the number of point forces; and L is the span (distance between centerline supports).

$$R_{right} = \sum_{i}^{1:n} \frac{P_i l_i}{L} \qquad \text{Equation 37}$$

After generating the left reaction, the internal moment at each node was calculated by summing the moments caused by all nodal forces between the left support and the node of interest at each node. In Equation 38, the addition sign implies that standard engineering sign conventions are used and the reaction will always points upward and the point forces point downward (gravity).

$$M_k = R_{left} l_k + \sum_{i}^{1:k} P_i \left(l_k - l_i \right) \qquad \text{Equation 38}$$

The maximum bending stress at a point (F_b) is the internal moment divided by the section modulus. The section modulus for a hollow ellipse, Equation 39, is the difference of the moment of inertia of the solid (outer) ellipse and the hollow (inner) ellipse divided by the radius of the solid ellipse (total centroidal height).

$$S_x = \pi \left(\frac{r_A {r_B}^3 - \left(r_A - t \right) \left(r_B - t \right)^3}{4 r_B} \right) \qquad \text{Equation 39}$$

Table 40 contains the maximum computed stress in each bending test based on the three assumed cross sectional shapes. All specimens that failed during testing are listed in bold type. For specimens that did not fail, stress was limited by water capacity, and tests were stopped once water came out of the fill hole. These specimens were tested with their arbitrarily named 'top' side up, and then were rotated 90 degrees and tested again on their 'side', moving defects and getting more ovalization data from the same number of specimens.

Specimens G1-G3 (the longitudinal glass fiber specimens, which were tested first) have a large difference in stress from the circular cross section to the ellipse cross section. At failure, the elliptical cross section was measured to be near Brazier's collapse ovalization (22%), and this large shape change has a 4.8% reduction in section modulus versus a circle (there is a .4% loss in section modulus for a 6% loss in vertical radius). The glass

fiber tubes failed at around 50% fluid capacity; there was a large difference between the amount of water in a partially filled flat ellipse and a partially filled circle with the same hydraulic elevation. Carbon fiber tubes exhibit a similar stress for both the circle and ellipse cross-sections because they experienced less ovalization. The difference in section modulus was less than 1% from the initial circle for all carbon fiber tubes and the tubes failed or finished filling when the center was full.

Brazier's equation for radius change is based on an isotropic material – uniform elastic modulus in all directions – not an irregular material such as a multilayer composite shell. When the shell is modeled as an orthotropic material using Classical Lamination Theory (CLT) there can be a large discrepancy between the longitudinal elastic modulus and the radial elastic modulus (transverse in CLT). The all glass fiber tubes (G1-G3) had a radial modulus nearly double the transverse modulus, while the single carbon fiber tube had the opposite relationship, a longitudinal modulus more than double the transverse modulus. Specimens that were relatively stiff in the radial direction were more likely to oval severely before buckling, sometimes reaching the maximum collapse ovalization and the Brazier collapse moment.

Table 40 Maximum Bending Stress in Ksi

Specimen	Circle	Ellipse - Vertical	Ellipse - Horizontal
G1	5.11	-	6.14
G2	5.42	-	6.74
G3	5.57	-	6.87
C1-top	9.27	-	-
C2-top	8.46	8.66	8.88
C3-top	10.4	10.6	10.7
C3-side	10.4	10.5	10.8
C4-top	10.3	-	10.6
C4-side	10.1	10.3	-
C5-top	7.05	7.05	7.14
C5-side	6.95	6.96	7.12
C6-top	6.74	6.76	6.92
C6-side	4.28	-	4.32

The described analysis method for generating a series of point loads from deflected shape and fluid ponding was not a usual method for analyzing a beam or running a laboratory test. To check the accuracy of the assumptions and the measured deflections, the center deflection for each tube was calculated using finite element beam code and the calculated load based on filled fluid volume. A model was constructed with two-noded Euler Bernoulli beam elements. Nodes were distributed at the same locations as water testing analysis, cross section shell area A and moment of inertia I were based on the deformed cross section (different deflections are generated based on model assumptions) and varied along the length of the beam, and the elastic modulus was based on the experimental bending modulus from sand bag tests in Table 37. The beam was given simple supports; the left support was a pin, the right support was a roller.

Three cross section shapes: circle, ellipse based on measured vertical deflection, and ellipse based on measured horizontal deflection, give different deflections. The ellipse prediction based on horizontal measurements generates the largest deflection prediction because it had the smallest moment of inertia. As seen from the results, actual mid span deflections were close to model predictions, frequently having less than 10% difference. The vertical measured deflection gave the best prediction for mid span deflection, the model over predicts deflection in five of nine tests, showing an almost even number of times above and below the predicted value. This assumption also had two trials with less than 1% difference between measured and predicted deflection and an additional three trials with less than 5% difference between measured and predicted deflection. Figure 93 shows the measured and predicted mid span deflection, assuming the vertical radius measured shape change, for the duration of the test C4-side. In this plot, the measured and predicted deflections remain close except for a single point where the vertical deflection jumps.

Table 41 Actual and Predicted Deflection in inches and % Difference

Test	Actual	Circle	% (A-C)	Vertical	% (A-V)	Horizontal	% (A-H)
C1-top	6.06	5.83	-4.12	-	-	-	-
C2-top	6.26	5.24	-16.5	140	-12.0	148	-6.88
C3-top	6.26	6.73	8.00	177	11.5	186	17.0
C3-side	6.14	6.73	9.59	178	13.7	188	20.3
C4-top	6.97	6.61	-4.75	169	-4.46	183	3.45
C4-side	6.73	6.46	-4.01	170	-0.742	-	-
C5-top	6.46	6.38	-0.930	162	-0.930	168	2.48
C5-side	6.10	6.26	2.45	161	3.27	170	9.15
C6-top	3.06	2.98	-2.61	75.9	-2.29	79.8	2.61
C6-side	1.64	1.81	10.4	46.0	10.4	47.0	12.8

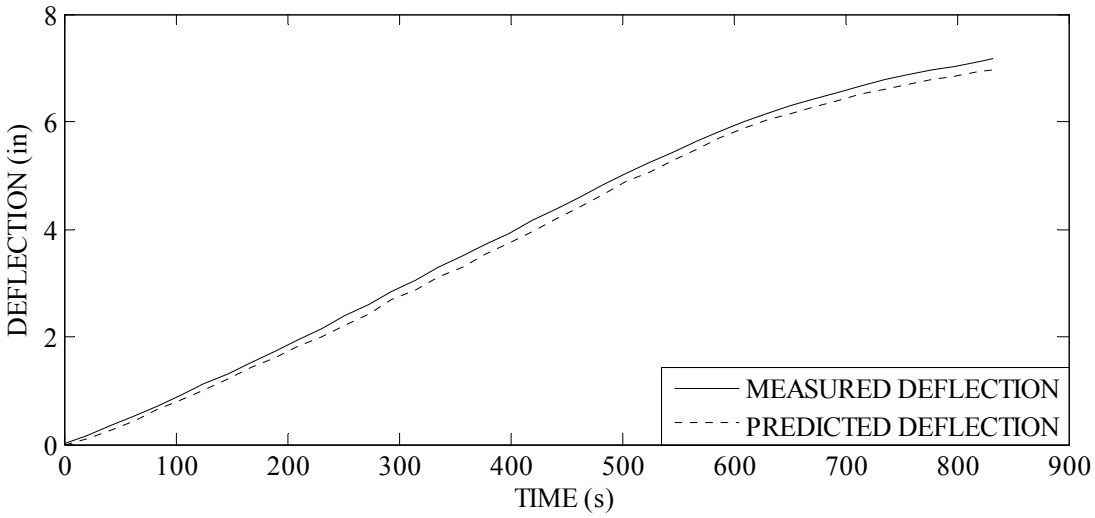

Figure 93 - Comparison of Measured and Predicted Deflection, C4-top

Later experimental tests showed that tubes C3 and C4 were slightly stronger than tubes C1 and C2, but an additional factor that may have influenced early failure was thermal

gradient. Tubes C1 and C2 were both tested on sunny days while tubes C3 and C4 were both tested on overcast days. Approximately 10 minutes after the failure of tube C2 thermal readings were taken of the water inside the tube as well as the shell temperature in areas that were fully filled, partially filled, and completely empty. Exposed to direct sunlight, the black, insulating carbon fiber shell absorbed a significant amount of heat from the sun and the 30 degree temperature shift from the area cooled by the water to the top fibers exposed to direct sunlight may have contributed to cross sectional distortion influencing a lower failure stress.

Table 42. Temperature of Tube C2 After Failure, in Degrees Celsius

Air	Water	Mid Span Carbon	Sixth Point Carbon	End Carbon
23	12	28	43	52

Stress Versus Ovalization

Ovalization is a function of bending stress and curvature; in a straight linear elastic beam curvature and bending stress are directly related, making ovalization a function of bending stress. As bending stress increases in the specimen the ovalization increases; this much is consistent in every test. Two methods of measuring ovalization were used: measuring the horizontal radius growth with four string pots and triangulating to horizontal and vertical displacements and measuring the vertical radius contraction with an LVDT mounted on a yoke surrounding the tube. The glass fiber tubes G1-G3 only used horizontal radius measurement equipment, not a direct measurement of the vertical radius. Ovalization at failure closely related to the Brazier ovalization prediction at failure, but shape of the radius change versus load plots were nearly linear while the Brazier prediction indicated a sharp radius change increase at the end of the test. A high initial deflection and a nearly linear response are hallmarks of the horizontal measurement technique (Figure 94, Figure 96), a shape contrary to both predictions which indicates faster radius change as the bending stress becomes higher. In all stress versus ovalization plots, radius change refers to the vertical radius change, either directly measured or calculated from the measured horizontal radius change, and the stress was calculated using the deformed shape based on the radius change being displayed. All laminates except double carbon have the Tatting predictions extended to the collapse moment.

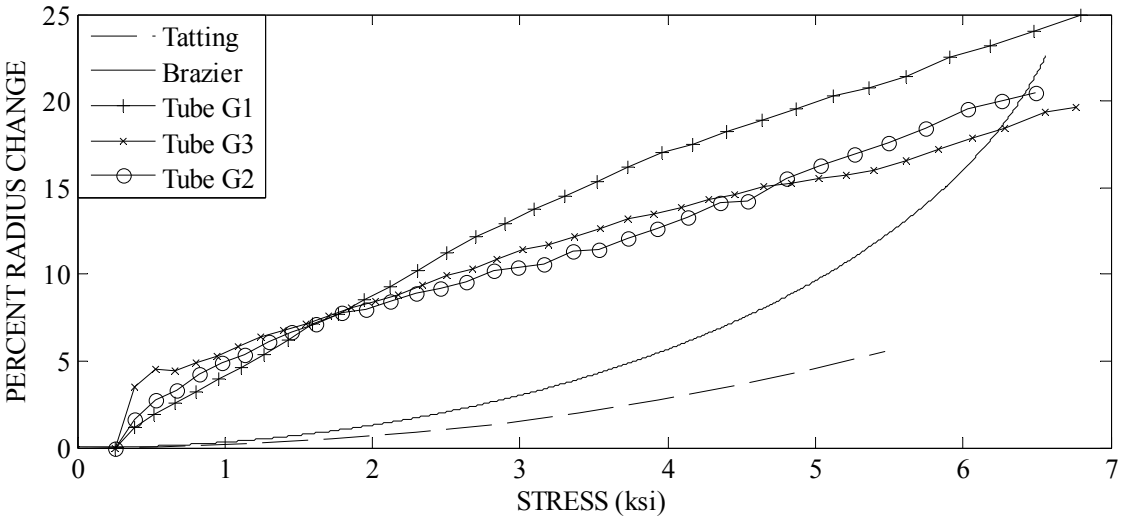

Figure 94 - Radius Change vs Stress, Glass Tubes, Horizontal Radius

Single layer carbon specimens showed a reasonable correlation between Tatting ovalization prediction and the actual ovalization from vertical measurements (Figure 95). Tube C2 ovals faster than the other tubes, but this tube failed near the LVDT measuring vertical deflection, so if a local curvature or radius defect caused a stress concentration, additional ovalization occurred in this vicinity. The horizontal measurements for all of the carbon fiber tubes are similar to the glass fiber measurements; the entire response shape is different from the shape of the Tatting prediction and the initial response is steeper (Figure 96, Figure 97, andFigure 98). Either the horizontal measurements are correct, and the tube changes shape in a very different way than thought, or the horizontal measurements are being skewed by a poor assumption. A possibility that explains the difference is longitudinal motion. Water is filled from a side, not at the center, and that side will have a higher weight of water before it distributes, causing unbalanced fluid height along the length, and potentially lateral motion in the loose lateral restraints. Results show this behavior; specimens have slower ovalization later in the test when ovalization rate should be increasing, but weight should be more evenly distributed reducing lateral translation.

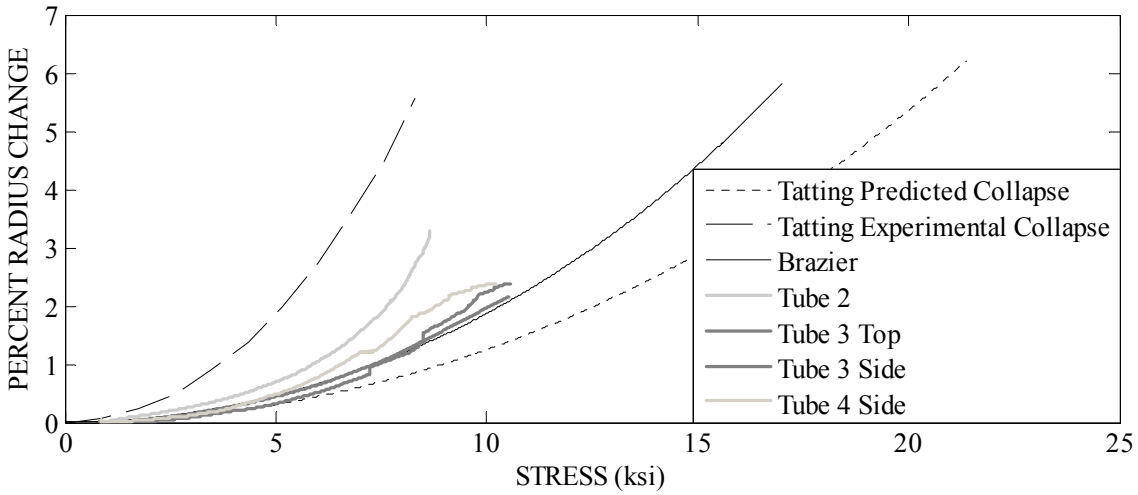

Figure 95 - Radius Change vs Stress, Single Carbon Tubes, Vertical Radius

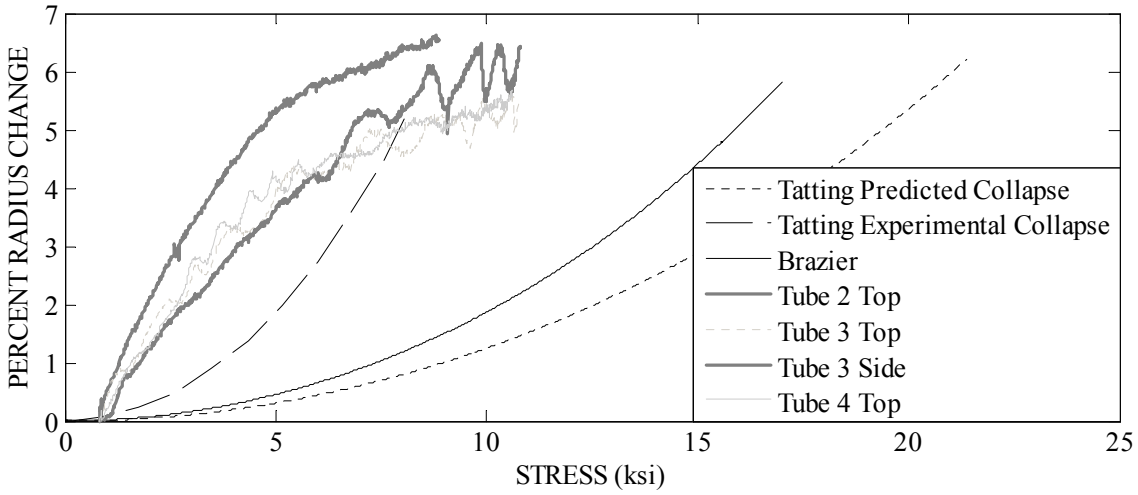

Figure 96 - Radius Change vs Stress, Single Carbon Tubes, Horizontal Radius

AEWC Advanced Structures & Composites Center
5793 AEWC Bldg
University of Maine
Orono, ME 04469-5793

Telephone: 207-581-2123
FAX: 207-581-2074
contactaewc@umit.maine.edu
www.aewc.umaine.edu

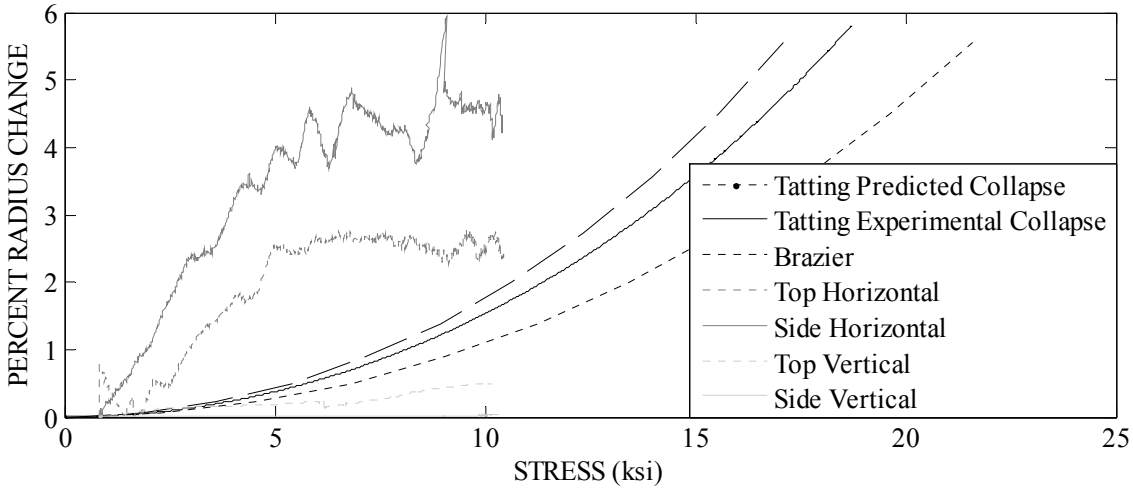

Figure 97 - Radius Change vs Stress, Bleeder Carbon Tube

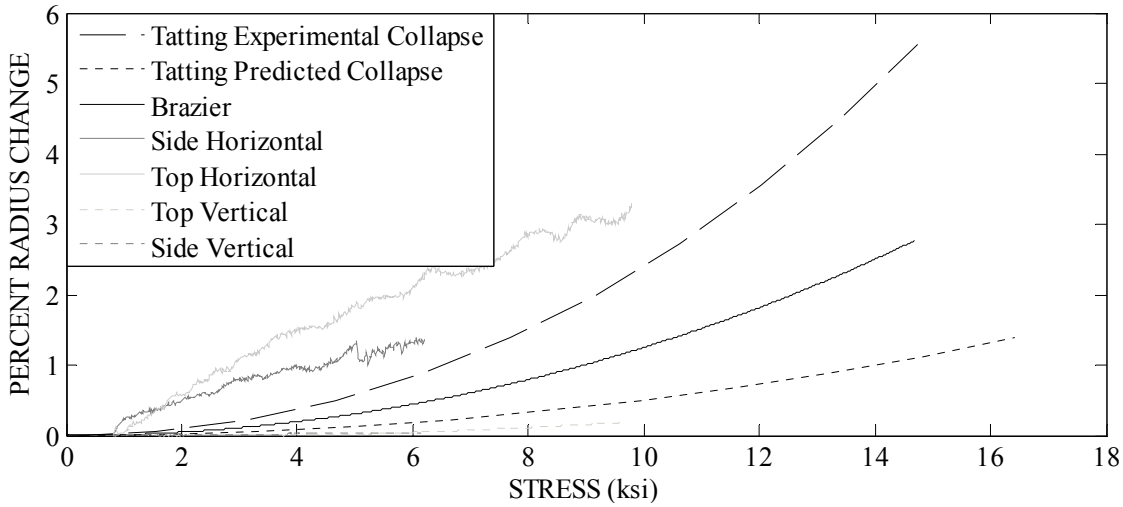

Figure 98 - Radius Change vs Stress, Double Carbon Tube

In all cases except the double carbon tube, the Brazier ovalization prediction appeared closer to experimental data than the more sophisticated Tatting prediction.

Conclusions

Bending tests were conducted on long cylinders to assess importance of ovalization, or Brazier's effect, on the bending stress in a tube. Glass fiber structural tubes showed a

large change in radius that caused a noticeable reduction in section modulus; measurement indicated ~20% gain in horizontal radius before failure, and a loss of over 4% of the section modulus. The change in radius closely matched Brazier's theoretical collapse ovalization and the bending stress also corresponded closely to Brazier's ultimate moment. The amount of ovalization was likely smaller than the measurement and influenced by poor results that exaggerated early ovalization results.

Carbon fiber tubes did not respond in the same manner. Two of the four single-layer carbon fiber tubes failed during testing; both failures occurred well below the Brazier predicted collapse ovalization or moment, regardless of measurement technique. However, subsequent compression tests of short tubes, Compression of Hollow FRP, showed that the computed ~8.70ksi failure stress is not unreasonable for this material in this geometric configuration. Single carbon, short tubular compression specimens failed at an average of 11.6ksi, but individual specimen capacities varied from 8.56ksi – 17.0ksi. The lower bound of experimental compression tests corresponds to the calculated buckling stress for the bending specimen. As carbon fiber is the preferred material for longitudinal structural reinforcing, the results of these tests indicate that ovalization during filling may not be an important effect to account for when designing a beam or arch.

Ovalization cannot be used as failure criteria because there is not an ovalization that relates directly to failure; every geometry and fiber lay-up is going to have a different response. The small magnitude of the ovalization at failure for the carbon specimens (3% loss in vertical radius) is not easily seen by the human eye and is difficult to measure during a test – especially as the cross section translates and sways during a ten-minute fill. Failure will occur below the maximum ovalization, before the theoretical collapse moment, because the local buckling stress was controlled by material defects and laminate asymmetry.

Future Work

It is unlikely that these tests will be repeated as detailed here. Many improvements to the testing procedure were made between initial testing and the second round of testing. The first testing measured radius change only through string pot triangulation at mid span; after reviewing results this method was determined to be inaccurate and prone to consistent error. Initial testing had no support displacement measurement, no direct vertical radius change measurement, short string pots that were more sensitive to out of plane motion, and a water quantity that assumes tap water pressure remains constant. Yokes were not used in initial testing to prevent damage to instrumentation from the collapse of the specimen. In subsequent testing, no LVDTs were damaged by the falling tube. Later testing corrected many of these problems. LVDTs at the support measured support crushing and detected up to 0.079in of settlement in the maple saddle and the

neoprene layer supporting the tube. A single yoke with an LVDT measured direct vertical diameter loss; this measurement related much better to the predicted equations in both magnitude and general shape than horizontal measurements. Additional LVDTs would have been useful to verify the radius measurement. String pots with extended strings reaching over 23.6in initially reduced error from lateral and out of plane motion. A constant head water stand was used to deliver consistent fluid pressure.

Future testing should not use more instrumentation, but better apply the instrumentation. Instead of the 4 string pots at mid span, a single string pot measuring vertical change, as at the other sixth points, would improve vertical deflection measurements. The long LVDTs used at mid span, which frequently ran out of stroke during the test, could be eliminated. Two additional ovalization measurements using vertical LVDTs could give ovalization over the length of the tube instead of a single location. Another proposed change is to test multi-layer tubes (bleeder carbon and double bleeder) at a larger span length to generate higher bending stresses. All measurements show poor ovalization correlations for these tubes, but the tubes saw low stress making the expected ovalization more affected by the error in the measurement technique.

Summary

This project dealt with the refinement of analysis methods and the improvement of design tools and some materials. Significant cost savings can be achieved with this work for most projects. Improvements to the soil-structural interaction analysis allow for a methodical and established way of allowing the soil to achieve passive or active condtions in the model. A new decking product was introduced that allows for an increased spacing of arches therefore decreasing cost and potentially eliminating the concrete overlay saving time and money. Advanced modeling of unfilled tubes gives a much greater understanding of the capacity of these unfilled tubes during construction. This allows for greater reliability in their performance and increases safety and potentially decreases cost.

References

Bannon, Dan. Goslin, Keenan WI-T-77 "Static and Fatigue Testing of Cylindrical Concrete Filled FRP Beams". AEWC Internal Work Instruction. AEWC Center June 26, 2008 rev Sept 2010.

Bannon, Dan. "Characterization of Concrete-Filled Fiber Reinforced Polymer (FRP) Arch Members". Master's Thesis. University of Maine. May 2009.

Baxter, John R. "FHWA Acceptance Letter B-124". Letter to Shane Weyant at Creative Pultrusions. December 9, 2003. http://safety.fhwa.dot.gov/roadway_dept /policy_guide_/road_hardware/barriers/pdf/b124.htm. Cited July 7, 2011.

Brazier, L. G. (1927). On the flexure of thin cylindrical shells and other "thin" sections. *Proceedings of the Royal Society of London. Series A, Containing Papers of a Mathematical and Physical Character,* 116(773), 104-114.

Carey, J. et. al. (2003). Longitudinal elastic model prediction of a 2-d braided fiber composite. *Journal of Reinforced Plastics and Composites*, 22, 813-831.

Chen, L. et. al. (1999). Mechanical analysis of 3-d braided composites by the multiphase element method. *Composites Science and Technology*, 59, 2383-2391.

Clapp, Joshua. William Davids. "CFRP Arch Analysis and Theory". AEWC Technical Report 11-30. University of Maine. January 31, 2011

Creative Pultrusions, Inc. "Superdeck Technical Data". Alum Bank, PA http://www.creativepultrusions.com/LitLibrary/products/superdeck/brochure.pdf. July 22, 2011.

Cox, B. N. and Dadkhah M. S. (1995). The macroscopic elasticity of 3D woven composites. *Journal of Composite Materials*, 29, 785-819.

Daniel, I. M. and Ishai, O. (2006). Engineering mechanics of composite materials, 2nd Edition. Oxford, Ny.: Oxford University Press.

Demkowicz, M. (2011). Environmental durability of hybrid braided polymer matrix composites for infrastructure applications. (Master's thesis, University of Maine, 2011 – publishing pending).

Donnell, L. H. (1934). Stability of thin-walled tubes under torsion. *NACA TR-479*.

Donnell, L. H. (1934). A new theory for the buckling of thin cylinders under axial compression and bending. *Transactions of the American Society of Mechanical Engineers*, 56, 795-806.

Edgren, F. and Asp, L. E. (2005). Approximate analytical constitutive model for noon-crimp fabric composites. *Composites: Part A*, 36, 173-181.

El-Chiti, F. (2005). Experimental variability of e-glass reinforced vinyl ester composites fabricated by VARTM/Scrimp. (Masters thesis, University of Maine, 2009).

El-Chiti, I. (2004). FRP-concrete arch. (Masters thesis, University of Maine, 2009).

Enduro Systems Inc. (n. d.). Tuff Span ® 8.0 Roof Deck Series 700. In *Enduro Systems Tuff Span® Building Products Guide Catalogue.* Retrieved June 2, 2011, from <http://www.endurocomposites.com/downloads/Enduro_Tuff_Span_Building_Products_Guide_Catalog.pdf>.

Faraji S, Ting JM, Crovo DS, Ernst H (2001). Nonlinear analysis of integral bridges: finite-element model. *Journal of Geotechnical and Geoenvironmental Engineering*, 127(5): 454-461.

Fuchs H. P. and Hyer M. W. (1996). The nonlinear response of short thin-walled laminated composite cylinders in bending. *Composite Structures*, 34, 309-324.

Goslin, Keenan. Neal Bridge Replacement-Structural Calculations. AEWC project 622. February 2, 2009.

Harajli, M. H. (2006). Axial stress-strain relationship for FRP confined circular and rectangular concrete columns. *Cement & Concrete Composites* 28, 938-948.

Jiang , T. & Teng, J. . (2007). Analysis-oriented stress-strain models for FRP-confined concrete. *Engineering Structures,* 29, 2968-2986.

Jones, R. M. (1975). Mechanics of composite materials. Washington DC: Hemisphere Publishing Company.

Jones, R. M. (2006). Buckling of bars plates and shells. Blacksburg Va.: Bull Ridge Publishing.

Kedward, K.T. (1978). Nonlinear Collapse of thin-walled composite cylinders under flexural loading. *Proceedings, 2nd International Conferece on Composite Materials,* Metal Society of AIME, Warrendale Pa., 353-365.

Lei, C. et. al. (1992). Finite element analysis of 3-d braided composites. *Advances in Engineering Software*, 14, 187-194.

Li, L. Y. (1996). Bending instability of composite tubes. *Journal of Aerospace Engineering*, 9 (2), 58-60.

Martin Marietta Composites. "DuraSpan fiber-reinforced polymer bridge deck systems". Raleigh, North Carolina. www.martinmariettacomposites.com. July 22, 2011.

Mostoller, Jeremy. "Arch Sheathing Panel: Global sizing Verification". Engineering report from Creative Pultrustions, Inc. to Advanced Infrastructure Technologies, LLC. January 20, 2011.

Nairn J. A. (1997). On the use of shear-lag methods for analysis of stress transfer in unidirectional composites. *Mechanics of Materials*, 26, 63-80.

NCHRP (1991). *Manuals for the Design of Bridge Foundations*. National Cooperative Highway Research Program Report No. 343, Transportation Research Board, Washington, DC.

Reissner, E. and Weinitschke, H. J. (1963). Finite pure bending of circular cylindrical tubes. *Quarterly Journal of Applied Mathematics,* 20, 305-319.

Richards, Dan. Phone Interview with Brad Hall regarding ZellComp decking capacity. August 8, 2011.

Resolite. Tred Safe Roof Panels Datasheet. San Diego, CA. http://www.fiberglasssheets.com/FRP/Resolite-Tred-Safe-Roof-skylight-fiberglass-roof-panels. July 22, 2011.

Saha, M., Prabhakaran, R., Waters, W. A. Jr. (2004). Compressive behavior of pultruded composite plates with circular holes. *Composite Structures*, 65, 29-36.

Sanders, J. L. (1970). Nonlinear theories for thin shells. *Quarterly Journal of Mechanics and Applied Mathematics,* 21, 25-36.

Seide, P. and Weingarten, V. I. (1961). On the buckling of circular cylindrical shells Under pure bending. *Journal of Applied Mechanics,* 28, 112-116.

Shen, H. S. (2008). Boundary layer theory for the buckling and postbuckling of an anisotropic laminated cylindrical shell. Part I: prediction under axial compression. *Composite Structures*, 82(3), 346-61.

Silvestri, N. (2007). Generalised beam theory to analyse the buckling behaviour of circular cylindrical shells and tubes. *Thin-Walled Structures*, 45, 185-198.

Soutis, C, and Fleck, N. A. (1990) Static compression failure of carbon fibre T800/924C composite plate with a single hole. *Journal of Composite Manufacture*, 24, 536-558.

Sykora, S. (2010). Ellipse Perimeter Approximations. *Stan's Hub,* Web, 10 Mar. 2011. <http://www.ebyte.it/library/docs/math05a/EllipsePerimeterApprox05.html>.

Tatting, B.F., Gurdal, Z. and Vasiliev, V. V. (1997). The Brazier effect for finite length composite cylinders under bending. *International Journal of Solids and Structures*, 34, 1419-1440.

Tatting, B.F. (1998). Analysis and design of variable stiffness composite cylinders. (PhD thesis, Virginia Polytechnic Institute and State University, 1998).

Ting JM and Faraji S (1998). *Force-Displacement Testing for Integral Abutment Bridges*. University of Massachusetts Transportation Center Report No. UMTC 97-13, University of Massachusetts, Amherst, MA.

Tomblin, J. (2006). Buried frp-concete arches. (Masters thesis, University of Maine, 2006).

Toutanji, H. A. (1999). Stress-strain characteristics of concrete columns externally confined with advanced fiber sheets. *ACI Materials Journal,* 96(3), 397-404.

USACoE (1994). *Design of Sheet Pile Walls*. CECW-ED Engineer Manual 1110-2-2504. Department of the Army, US Army Corps of Engineering, Washington, DC.

Walton, Harold. "Response of FRP Arches to Concrete Filling Loads". Master's Thesis. University of Maine. August 2011.

Weaver, P. M. (2002). Anisotropy-induced spiral buckling in compression-loaded cylindrical shells. *AIAA Journal*, 43, 2639-2645.

Wierzbiecki, T. & Sinmao, M. V. (1997). A simplified model of Brazier effect in plastic bending of cylindrical tubes. *International Journal of Pressure Vessels and Piping*, 71(1), 19-28.

Zellcomp. Fiber-reinforced composite bridge decks. Durham, NC. www.zellcomp.com. July 22, 2011.

Zeng, T. et. al. (2004). Mechanical analysis of 3d braided composites: a finite element model. *Composite Structures*, 64, 399-404.

Page: 1
By: JDC Date: 5/2/2011
Checked by: ___ Date: 5/2/2011

AEWC Center

5793 AEWC Building
Orono, Maine 04669
Telephone: (207) 581-2123
Fax: (207) 581-2074
www.aewc.umaine.edu

Designed By: JDC
Date: 01/20/11
Checked By:
Date:
Job Number: 906F

Project: AIT Soil-Structure Interaction
Task: Calculate Analysis Properties

References
1. Proposed decking design drawing provided by Matthew Pellerin of AIT.

Uncracked decking properties in the transverse direction (spanning arches)

AASHTO 2007 allows either uncracked or cracked sections to be considered depending on the expected situation, assume cracked

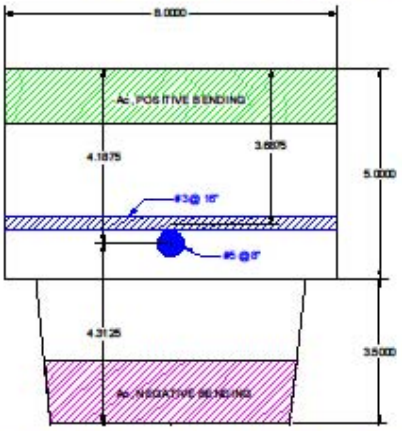

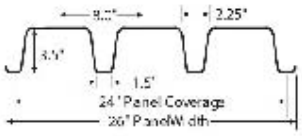

Concrete section - perpendicular to arch span (some properties from AutoCAD)

TRANSVERSE

$$Ag := \frac{21.44in^2 + 8in \cdot 5in}{8in} = 7.68 \cdot \frac{in^2}{in}$$

Concr. strength $f_c := 4350psi$ (MDOT spec.)

Concr. stiffness $E_c := 57000 \cdot \sqrt{f_c \cdot psi}$ $E_c = 3759 \cdot ksi$

Modular ratio $n_s := \frac{29000ksi}{E_c}$ $n_s = 7.71$

UNCRACKED

Ybar (top)

$$y_t := \frac{8in \cdot 5in \cdot 2.5in + 21.44in^2 \cdot 6.71in + \frac{\pi}{4} \cdot \left(\frac{5}{8}in\right)^2 \cdot (n_s - 1) \cdot 4.18in}{8in \cdot 5in + 21.44in^2 + \frac{\pi}{4} \cdot \left(\frac{5}{8}in\right)^2 \cdot n_s}$$

$y_t = 3.96 \cdot in$

C:\Documents and Settings\joshua.clapp\Desktop\Arch Decking Calcs.xmcd

AEWC Advanced Structures & Composites Center
5793 AEWC Bldg
University of Maine
Orono, ME 04469-5793

CONFIDENTIAL

Telephone: 207-581-2123
FAX: 207-581-2074
contactaewc@umit.maine.edu
www.aewc.umaine.edu

Page: 2
By: JDC Date: 5/2/2011
Checked by: ___ Date: 5/2/2011

TRANSVERSE (continued)

Moment of inertia

$$I := \frac{\frac{8in\cdot(5in)^3}{12} + 8in\cdot5in\cdot(y_t - 2.5in)^2 + 21.86in^4 + 21.44in^2\cdot(6.71in - y_t)^2 + \frac{\pi}{4}\cdot\left(\frac{5}{8}in\right)^2\cdot(n_s - 1)\cdot(4.18in - y_t)^2}{8in} \quad I = 44.09\cdot\frac{in^4}{in}$$

Equivalent thickness for self-weight

$$t := \frac{(8in\cdot5in + 21.44in^2 + 0.125in\cdot8in)}{8in} \quad t = 7.81\cdot in$$

POSITIVE BENDING CRACKED

Solve for ybar and I

Given $y_{bar} := 0.5in$ $A_s := 0.31in^2$ $d := 4.1875in$

$$8in\,y_{bar}\cdot\frac{y_{bar}}{2} - n_s\cdot A_s\cdot(d - y_{bar}) = 0$$

$y_{bar} := \text{Find}(y_{bar})$ $y_{bar} = 1.31\cdot in$

$$I := \frac{y_{bar}^3}{12} + y_{bar}\cdot\left(\frac{y_{bar}}{2}\right)^2 + n_s\cdot\frac{A_s}{8in}\cdot(d - y_{bar})^2 \quad I = 3.224\cdot\frac{in^4}{in}$$

NEGATIVE BENDING CRACKED

Given $y_{bar} := 0.5in$ $A_s := 0.31in^2$ $d := 4.31in$

$$5.75in\,y_{bar}\cdot\frac{y_{bar}}{2} + \frac{6.5in - 5.75in}{3.5in}\cdot y_{bar}\cdot\frac{y_{bar}}{2}\cdot y_{bar}\cdot\frac{1}{3} - n_s\cdot A_s\cdot(d - y_{bar}) = 0$$

$y_{bar} := \text{Find}(y_{bar})$ $y_{bar} = 1.51\cdot in$

$$I := \frac{6.7179in^4}{8in} + n_s\cdot\frac{A_s}{8in}\cdot(d - y_{bar})^2 \quad I = 3.181\cdot\frac{in^4}{in}$$

Say I = 3.2 in^4/in both ways

LONGITUDINAL

UNCRACKED

$$I_{long} := \frac{(5in)^3}{12} = 10.42\cdot\frac{in^4}{in} \qquad A_{long} := 5in = 5.00\cdot\frac{in^2}{in}$$

Given $y_{bar} := 0.5in$ $A_s := 0.11in^2$ $d := 3.6875in$

$$16in\,y_{bar}\cdot y_{bar} - n_s\cdot A_s\cdot(d - y_{bar}) = 0$$

$y_{bar} := \text{Find}(y_{bar})$ $y_{bar} = 0.42\cdot in$

C:\Documents and Settings\joshua.clapp\Desktop\Arch Decking Calcs.xmcd

Page: 3
By: JDC Date: 5/2/2011
Checked by: ___ Date: 5/2/2011

LONGITUDINAL (continued)

POSITIVE BENDING CRACKED

$$I_{pos} := \frac{y_{bar}^3}{12} + y_{bar}\cdot\left(\frac{y_{bar}}{2}\right)^2 + n_s\cdot\frac{A_s}{16in}\cdot(d - y_{bar})^2 \qquad I_{pos} = 0.592\cdot\frac{in^4}{in}$$

Given $y_{bar} := 0.5in$ $A_s := 0.11in^2$ $d := 1.3125in$

$16in\,y_{bar}\cdot y_{bar} - n_s\cdot A_s\cdot(d - y_{bar}) = 0$

$y_{bar} := \text{Find}(y_{bar})$ $y_{bar} = 0.24\cdot in$

NEGATIVE BENDING CRACKED

$$I_{neg} := \frac{y_{bar}^3}{12} + y_{bar}\cdot\left(\frac{y_{bar}}{2}\right)^2 + n_s\cdot\frac{A_s}{16in}\cdot(d - y_{bar})^2 \qquad I_{neg} = 0.066\cdot\frac{in^4}{in}$$

FRP decking - CP155

$n_{FRP} := \frac{4200ksi}{E_c}$ $n_{FRP} = 1.12$

$I_{FRP} := \frac{11.16in^4}{ft}$ $I_{FRP} = 0.93\cdot\frac{in^4}{in}$

$A_{FRP} := \frac{3.64in^2}{ft}$ $A_{FRP} = 0.30\cdot\frac{in^2}{in}$

$wt_{FRP} := 3.75psf$ $t_{eq} := \frac{3.75psf}{145pcf}$ $t_{eq} = 0.31\cdot in$

Arch Moment of Inertia

Effective diameter for EI calculation $d := 11.8in$

Uncracked $I_{uncracked} := \frac{\pi\cdot d^4}{64} = 951.70\cdot in^4$

$EI_{uncracked} := E_c\cdot I_{uncracked} = 3.58\times 10^6\cdot kip\cdot in^2$

Cracked $EI_{cracked} := \frac{669.21kip\cdot in}{\frac{0.000911}{in}} = 7.35\times 10^5\cdot kip\cdot in^2$

Ratio uncracked to cracked $\frac{EI_{uncracked}}{EI_{cracked}} = 4.87$

Ratio arch to concr. deck M+ $\frac{EI_{cracked}}{I_{pos}\cdot E_c\cdot 60in} = 5.51$

Ratio arch to concr. deck M- $\frac{EI_{cracked}}{I_{neg}\cdot E_c\cdot 60in} = 49.58$

C:\Documents and Settings\joshua.clapp\Desktop\Arch Decking Calcs.xmcd

AEWC Advanced Structures & Composites Center
5793 AEWC Bldg
University of Maine
Orono, ME 04469-5793

Telephone: 207-581-2123
FAX: 207-581-2074
contactaewc@umit.maine.edu
www.aewc.umaine.edu

APPENDIX B: COMPRESSION BOUNDARY PLATES

B.1. Under Layers

Under layers were used either to provide a rigid surface to increase the area of the crosshead or to provide a softer layer to help distribute the load on the specimen. The base layer was typically ½in steel plate with a 11.8in by 18.8in area (see Figure B.1), but for testing larger diameter specimens and some of the subsequent 6.5in specimens a 5 layer built up 3.74inthick by 18.8in per side plywood plate was used to increase the area of the crosshead, as in Figure B.2.

With both resin caps and plywood plates, 0.236in neoprene was sometimes used as a distribution layer where differential crushing of the neoprene would more evenly distribute the load. This technique is used in the testing of concrete cylinders. Results indicated that neoprene gave no improvement-specimens with neoprene still had uneven strains and were as likely to undergo resin cracking prior to tube buckling. Figure B.1 and Figure B.2 show typical boundaries using a neoprene distribution layer.

Figure B.1. Resin Cap with Neoprene Distribution Layer and Steel Base

Figure B.2. Wood Plate with Neoprene Distribution Layer and Wood Base

B.2. Steel Bearing Plates

When steel was used in direct contact with the specimen the specimen failed in bearing as observed in testing during the summer of 2009 as well as specimen 6-3.

Figure B.3. Specimen Crushed by Direct Contact with Steel Bearing Plate

The high bending stiffness of the thick steel plate and the high elastic modulus of the steel (greater than the specimen) allowed for insufficient movement at the boundary interface and localized contact caused a delamination failure on the end of the tube.

B.3. Resin Caps

Approximately 12mm thick resin caps were cast onto the top and bottom face of the specimen to generate even boundaries. The caps were parallel to each other, but in many cases they were not flat because the heat of resin curing caused the cap to warp as it was forming. Caps were shaped by flat-sided glass moulds with concave sidewalls treated with a mold release to allow easy removal of resin. A piece of chopped strand glass fiber matting was placed into the resin to limit thermal shrinkage cracking. During curing the specimen was suspended approximately 6mm above the glass plate to center the specimen within the resin.

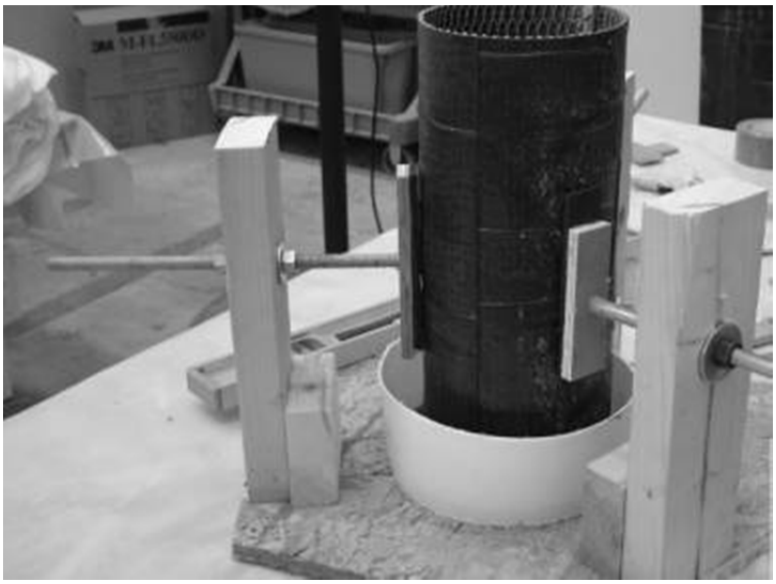

Figure B.4. Specimen in Resin Capping Stand

During loading, resin caps frequently fractured before the specimen failed; a series of loading and unloading ensued that decreased the accuracy of the strain measuring instruments and caused uneven loading conditions leading to early failure.

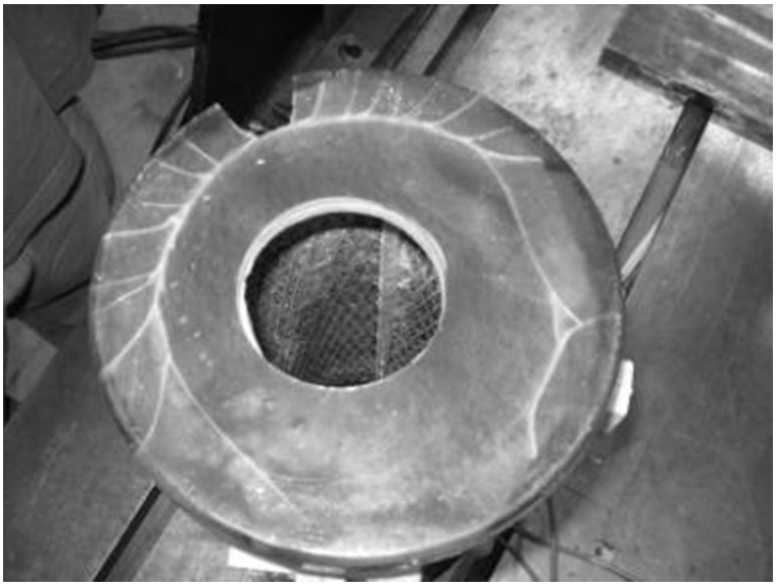

Figure B.5. Cracked Resin Cap After Loading

Resin caps also allowed several specimens to fail in sudden buckling, but the resin caps were higher cost, one time use, time consuming to manufacture, and produced many specimens that could not be counted for ultimate strength. With unlimited time and access to materials, resin caps may produce the best boundary. For this lab trial, resin caps proved difficult to implement.

B.4. Plywood Bearing Plates

Plywood was used as the boundary plate for all tests in 2009 and many tests in 2010, becoming the preferred boundary for future testing. Testing in 2009 employed ½" CDX pine plates reused for all specimens. These plates became heavily grooved after a single test and in subsequent tests may have contributed to the uneven load distributions measured on the specimen and indicated by the failure type.

Figure B.6. Plywood Cap on a 300mm Specimen

Imperfections in the wood such as initial curvature or knots and other inclusions may have contributed to uneven loading conditions. To correct this issue the plywood used in 2010 was a ¾"cabinet grade hardwood with lower curvature and cleaner faces with fewer knots. Wooden plates were only used twice – once on each side – to ensure that specimens were not loaded unevenly due to existing grooves.

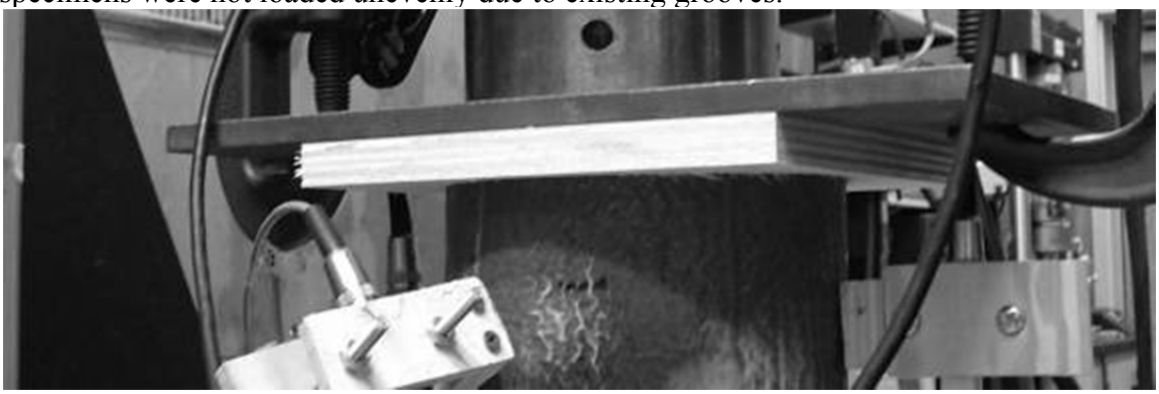

Figure B.7. Higher Grade Plywood Boundary

The plywood did not eliminate all uneven loading conditions but it did help uneven boundaries by crushing (differentially based on load) prior to specimen failure. Typical crushing began at 40% of max load for single layer samples and 20% of max load for other samples. Many specimens tested with wood boundaries show a single gauge taking a large amount of deflection initially that slows down after the wood begins crushing while other gauges take on additional deflection.

B.5. FRP Bearing Surface on Plywood

Plywood served as a good boundary for the larger diameter samples and the single layer specimens, but as the failure load became higher the plywood experienced large crushing deformations and the specimen failed in buckling-bearing failure. This failure mode is a buckling failure that occurs on an extreme edge of the specimen between the instrumentation and the plate. This failure initiates as a material wrinkle, but it suggests that the failure is influenced by the proximity of the load source. To correct this problem for stronger specimen types a plate was needed between the plywood that had a higher cutting strength, but was flexible enough to move with the plywood underneath as the plywood crushed. Two layers of braided carbon FRP (0.03in, +/-22 deg) arranged in opposite directions (strong axis of one lamina was placed against the weak axis of the other lamina) served as the bearing surface. During testing, the specimen damaged the FRP, breaking the matrix, but not breaking the fibers.

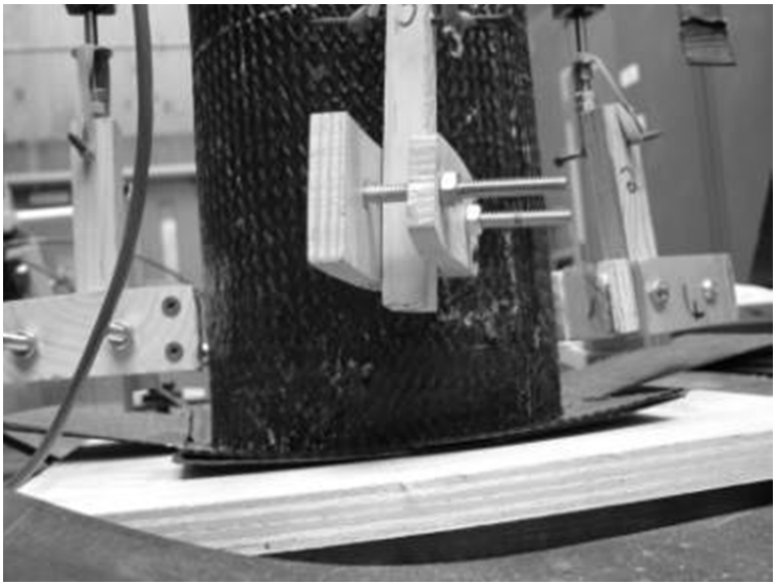

Figure B.8. FRP Plate with Plywood Sandwich Plate

The FRP bent around the specimen as it was forced into the plywood. The plywood groove from this test is both wider and shallower from those of similar load capacities performed without FRP covering. It resembled a dent instead of a cut.

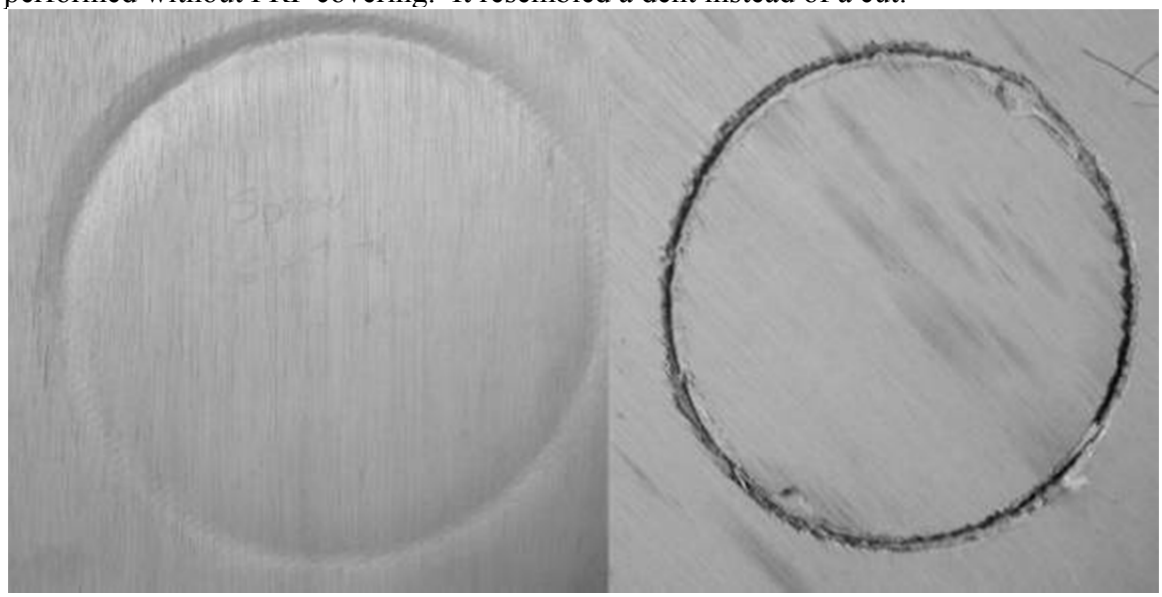

Figure B.9. Wood Core With FRP Without FRP

With FRP plates the failure mode changed from end bearing-buckling to buckling in bleeder specimens and in double carbon specimens the failure strength became more consistent and no specimens failed in bearing after making this transition. Alternatively, thin steel plates (0.04in – 0.08 in) may work for this task as well or better than the carbon FRP plates, but the carbon plates were available and reusable because as the fibers did not fracture. Whatever material is used the two critical features are sufficient capacity to resist cutting from the compression load, and bending flexibility to allow the specimen to crush the sub layer and have the plate travel with the sub layer as it crushes.

AEWC Advanced Structures & Composites Center
5793 AEWC Bldg
University of Maine
Orono, ME 04469-5793

Telephone: 207-581-2123
FAX: 207-581-2074
contactaewc@umit.maine.edu
www.aewc.umaine.edu